Lifetime Measurements probing Shape Coexistence in ^{175}Au, ^{174}Pt and ^{175}Pt

Thesis submitted in accordance with the requirements of the University of Liverpool for the degree of Doctor in Philosophy

by

Heidi Watkins

Oliver Lodge Laboratory

2011

This thesis is dedicated to my Mum,

for her unwavering love and giving me the skills to blossom and pursue my dreams.

"Logic will get you from A to B. Inspiration will get you everywhere."

Albert Einstein.

"Nothing great was ever achieved without enthusiasm."

Ralph Waldo Emerson.

"All our dreams can come true if we have the courage to pursue them."

Walt Disney.

Acknowledgements

I would like to thank my supervisor Dr. David Joss for giving me the opportunity to work on such an interesting project and for his guidance during my time as a PhD student.

I am especially grateful to Dr. Tuomas Grahn whose tutelage and knowledge became the nucleus of my thesis.

A huge thanks to Dr. David O'Donnell for many things, not least taking the time to read this entire thesis offering advice and corrections and being a wonderfully supportive, critical friend.

I would also like to thank Prof. Robert Page, Prof. John Simpson and Dr. Marcus Scheck for teaching me to question.

I would like to thank the staff of the Physics Department of the University of Jyväskylä and the Köln University Plunger group, especially Matthias Hackstein, in regard to the running of a smooth and successful experiment.

Many thanks to Dr. James Thomson, Dr. Paul Sapple and Robert Carroll for their constant camaraderie and good will throughout my PhD especially when we were far away from home.

I would like to thank many of the past and present members of the Liverpool Nuclear Structure group, especially Dr. Danielle Rostron, Dr. Laura Nelson, Dr. Suzanne Wong and Samantha Colosimo for their enduring friendship.

I would like to recognise all the collaborators involved in this research.

I would also like to acknowledge STFC, for providing the necessary financial support for this research project.

Finally, I would like to thank my mother Karen Watkins for her unconditional love and inspiration throughout my life.

Abstract

For the first time, lifetime measurements of the excited states in $^{175}_{79}$Au, $^{174}_{78}$Pt and $^{175}_{78}$Pt have been measured using the recoil-decay tagging technique in recoil distance Doppler-shift measurements. These states were populated by a fusion-evaporation reaction using a ^{92}Mo target and a 401 MeV ^{86}Sr^{16+} beam. This work was carried out at the Accelerator laboratory of the University of Jyväskylä, Finland, where a plunger device has been coupled to the JUROGAM detector array and the RITU gas-filled separator. The present study addresses the phenomenon of shape coexistence in neutron deficient nuclei below the $Z = 82$ closed shell.

Lifetimes of the low-lying excited states in the very neutron-deficient nucleus ^{175}Au have been measured. Transitional quadrupole moments and reduced transition probabilities extracted for this odd-Z nucleus provide evidence for the existence of three distinct shapes and indicate the transition between collective and non-collective structures. These measurements constitute the first deformation measurements of triple shape coexistence in a heavy odd-Z nucleus. The results are compared to the available lifetime measurements for Hg and Tl nuclei.

A lifetime of the 6^+ yrast state in ^{174}Pt has been measured using recoil-decay tagged γ-ray spectra. In addition, lifetimes of the $17/2^+$ and $21/2^+$ yrast states in ^{175}Pt have been measured using recoil-gated $\gamma\gamma$-coincidence spectra. Transitional quadrupole moments and deformation parameters extracted for these nuclei provide information on the change in nuclear shape resulting from the mixing of different shaped configurations at low spin. The results are compared to TRS calculations produced for neutron deficient Pt nuclei below the neutron $N = 104$ mid-shell.

Contents

Contents i

1 Introduction **1**

1.1 Nuclear Structure: Deformation and Rotation 4

1.1.1 Deformation Parameters 5

1.1.2 Collective Rotations 5

1.1.3 Nilsson Model 8

1.2 Quadrupole Deformation 14

1.2.1 Deformed Woods-Saxon Potential 16

1.3 Electromagnetic Transitions 16

1.3.1 Reduced Transition Probability 17

1.3.2 Reduced Transition Probability and Quadrupole Moment . . . 19

2 Experimental Methods and Apparatus **21**

2.1 Heavy-ion Fusion Evaporation 21

2.2 The JUROGAM II germanium detector array 23

2.2.1 Phase I detectors 23

2.2.2 Clover detectors 24

2.2.3 Compton suppression 25

2.2.4 Efficiency 26

2.3 The Recoil Ion Transport Unit (RITU) 27

2.4 The GREAT Focal Plane spectrometer 28

2.4.1 The Multiwire Proportional Counter (MWPC) 28

2.4.2 The DSSD implantation detectors 29
2.5 Data acquisition 30
2.5.1 Data Sorting 32
2.6 Tagging techniques 32
2.7 The RDDS method 35
2.8 The Plunger device 37
2.9 The differential decay curve method 39
2.9.1 Unobserved side feeding 43
2.10 Summary of experimental details 44

3 Deformation and collectivity of the coexisting shapes in ^{174}Pt and ^{175}Pt 46

3.1 Shape coexistence in ^{174,175}Pt 46
3.2 Results - the nucleus ^{174}Pt 48
3.2.1 Experimental details 48
3.2.2 Lifetime measurements of the 6^+ state 52
3.3 Results - The nucleus ^{175}Pt 54
3.3.1 Experimental details 54
3.3.2 Lifetime measurements of the $21/2^+$ and $17/2^+$ states 55
3.4 Discussion 60
3.4.1 Previous interpretation 60
3.4.2 Total Routhian Surfaces 63
3.4.3 Staggering Parameter 63
3.4.4 Collectivity of the 6^+ state in ^{174}Pt 65
3.4.5 Shape coexistence in ^{175}Pt 66
3.4.6 Triaxiality 67

4 Deformation and collectivity of the coexisting shape triplet in ^{175}Au 70

4.1 Triple shape coexistence in ^{175}Au 70
4.2 Results 74

4.2.1 Alpha decay properties of ^{175}Au 74
4.2.2 Experimental details 74
4.2.3 Lifetime measurements of the $25/2^+$ - $17/2^+$ states 76
4.2.4 Lifetime measurement of the $13/2^+$ state 82
4.3 Discussion 83
4.3.1 Previous interpretation 83
4.3.2 Collectivity of the $25/2^+$ and $21/2^+$ states 85
4.3.3 Shape mixing at the $17/2^+$ state 87
4.3.4 Single particle behaviour of the $13/2^+$ state 89

5 Summary **90**

Chapter 1

Introduction

This thesis explores the phenomenon of shape coexistence that is observed at low spin in the neutron deficient Au and Pt nuclei. Shape coexistence arises as configurations based on different deformations have similar excitation energy and therefore can compete for the yrast band. This occurs in nuclei near closed shells and has been interpreted in terms of intruder configurations based on particle-hole (p-h) excitations producing deformed configurations [Wood92, Heyd83]. This can occur because the energy minima of oblate or prolate bands are low enough in energy to lie close to the ground state. For neutron deficient nuclei below the $Z = 82$ closed shell, shape coexistence occurs when protons are scattered into the deformation driving $h_{9/2}$, $f_{7/2}$ and $i_{13/2}$ intruder orbitals. The shape observed in these nuclei is dependent on the number of neutrons; for heavier nuclei with a few neutrons above the $N = 104$ mid shell the low energy level structure is observed to be near spherical or oblate in shape. As the number of neutrons decrease the prolate shape minimum decrease in energy and dominates the low energy structure. This occurs as the number of valence neutrons increases, approaching the $N = 104$ mid-shell, providing the maximum interactions to scatter the protons into the intruding prolate orbitals. The even-even nuclei in this region provide a number of examples of shape coexistence. For example, the Hg isotopes have an oblate ground state that coexists with prolate shapes based on (4p-6h) proton excitations [Naza93, Juli01]. For the $Z = 82$, $N = 104$ ^{186}Pb

nucleus a shape triplet has been determined. This nucleus is observed to have a spherical ground state, a collective oblate non-yrast band (2 proton excitation) and a coexisting collective prolate yrast band (4 proton excitation) [Andr00]. The shape coexistence phenomenon has also been observed in odd-N Hg nuclei [Jenk02] and odd-Z Tl nuclei [Lane94] and Au [Kond01]. The microscopic origin of shape coexistence in odd-Z nuclei is different to their even-Z counterparts since the orbital within which the odd-proton is located plays an important role as it can stabilise the polarisation of the core. Moving away from the $Z = 82$ closed shell, with decreasing number of protons, nuclei such as Pt and Os can be deformed in the ground state resulting in a decrease in the difference in deformation between the competing minima. In these nuclei the phenomena of shape coexistence manifests itself as a mixed band instead of the different bands observed in the heavier nuclei.

Level structures associated with three different shapes were observed in ^{175}Au [Kond01]. The origins of triple shape coexistence in ^{175}Au are very different to those of ^{186}Pb [Paka05, Grah06]. In ^{175}Au at low spin, the different shapes are stabilised by the core polarising properties of single protons occupying either the $s_{1/2}$, $d_{3/2}$ or $h_{11/2}$ states below the shell gap or the $h_{9/2}$, $f_{7/2}$ and $i_{13/2}$ intruder orbitals above the $Z = 82$ shell closure. At high spin, the positive parity yrast sequence is a collective band based upon the prolate $\pi i_{13/2}$ configuration, but however, at low spin a shape transition is observed as the yrast band feeds an oblate $\pi i_{13/2}$ state at 977 keV [Kond01]. The 294 keV transition feeding the oblate $\pi i_{13/2}$ state does not follow the regular collective pattern established in the higher spin states, indicating shape mixing. The α-decaying isomeric state in ^{175}Au is based on the spherical $\pi h_{11/2}$ configuration. Thus, three different shapes compete to be yrast in ^{175}Au.

In the light Pt nuclei the phenomenon of shape coexistence is established as a mixed ground state band observed as a deviation from the regular I(I+1) rotational structure, at low spin. The irregular level spacing observed at low spin in the yrast band of ^{174}Pt was interpreted [Drac91] as a competition between triaxial and prolate shapes relating to the occupation of different proton orbitals. The prolate deformed

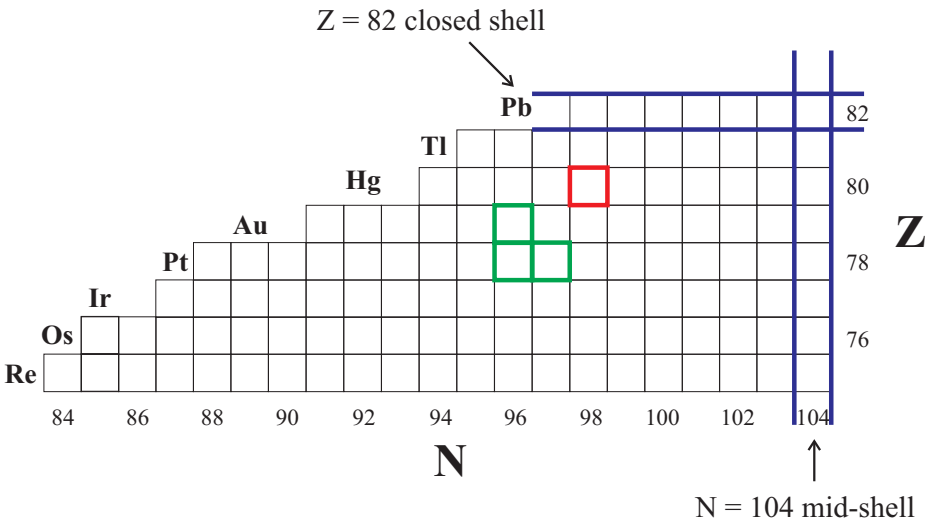

Figure 1.1: Schematic of the region of interest of the Segre chart below the $Z = 82$ shell gap. The green squares indicate ^{175}Au and ^{174,175}Pt, which are the subject of this thesis. The red square indicates the compound nucleus of the fusion-evaporation reaction, ^{92}Mo target + ^{86}Sr^{16+} $\rightarrow$ ^{178}Hg*.

band results from a pair of non-aligned protons scattering into deformation-driving $h_{9/2}/f_{7/2}$ orbitals [Drac91]. This irregular behaviour at low spin was also observed in the assigned $\nu i_{13/2}$ signature partner bands of ^{175}Pt [Cede90]. It was also noted that the $N = 98$ gap stays almost constant when the ^{175}Pt nucleus undergoes the calculated shape changes, implying the neutron configuration is not affected by the deformation changes. Therefore the low spin irregularity observed in ^{175}Pt was explained to be analogous to the crossing of different proton structures as discussed for the even-A Pt nuclei.

Obtaining quantitative information on the collectivity and deformation of the neutron deficient ^{175}Au and ^{174,175}Pt is challenging from an experimental viewpoint. The degree of collectivity for the low-lying excited states in nuclei can be determined experimentally from measuring the lifetime of the level. In doing so the absolute transition probabilities can be determined and provide a direct measure of the collectivity. In the present study, Recoil Distance Doppler Shift (RDDS) [Schw68] lifetime

measurements have been carried out in ^{174}Pt, ^{175}Pt and ^{175}Au. The lifetimes of the low-lying yrast states in ^{175}Pt, the 6^+ state in ^{174}Pt and the low-lying yrast states in ^{175}Au have been measured, allowing the quadrupole moments for the levels associated with different shapes to be extracted.

This chapter discusses the theoretical background for the motivation of this thesis and the calculations used to interpret the data, focusing on the models used to understand the different shapes and collective behaviour of the nuclei studied. Chapter 2 describes the techniques and apparatus used to acquire the experimental data. The experiment resulted in the lifetime measurements of the low-lying excited states in ^{174,175}Pt and ^{175}Au providing an insight into the single particle and collective nature of these nuclei. The results and their interpretations are discussed in Chapters 3 and 4, respectively. In Chapter 5 the nuclear structure of ^{174,175}Pt and ^{175}Au are discussed in the framework of the phenomena of shape coexistence and the implications for further studies into probing nuclear shape.

1.1 Nuclear Structure: Deformation and Rotation

The structure of the nucleus is characterised by nuclear models which broadly describe two different aspects of nuclear motion; single particle and collective motion. The liquid drop model depicts bulk coherent motion such as deformation, vibration and rotation and approximates the nucleus as a sphere of constant density. The shell model details single particle motion in which only the nucleons in the vicinity of the Fermi surface are involved and each particle moves in a state independent of the other particles. The study of the nucleus reveals the delicate interplay between these two modes of excitations. The shell model is successful at describing nuclear properties near closed major shells. In regions between the major shell closures, coherence in the single-particle motion can result in collective effects such as deformation. The concept of stable nuclear deformation can be investigated using a number of nuclear models.

1.1.1 Deformation Parameters

The nuclear shape can be described by defining a radius $R(\theta, \phi)$ from the centre of the nucleus to a point on the surface and can be expressed as a sum over the spherical harmonics $Y_\lambda^\mu(\theta, \phi)$:

$$R(\theta, \phi) = C(\alpha_{\lambda\mu}) R_0 \left[1 + \sum_{\lambda=0}^{\infty} \sum_{\mu=-\lambda}^{\lambda} \alpha_{\lambda\mu} Y_\lambda^\mu(\theta, \phi) \right] \tag{1.1}$$

where R_0 is the radius of a sphere and is equal to $r_0 A^{1/3}$, with A the mass number and r_0 determined empirically to be approximately 1.20 fm. Here $\alpha_{\lambda\mu}$ are the coefficients that represent the distortions from an equilibrium spherical shape and λ indicates the multipolarity of the deformation surface oscillation and μ is an integer ranging from $-\lambda$ to λ. The factor $C(\alpha_{\lambda\mu})$ is included to satisfy the condition of conservation of volume. The $\lambda = 0$ term does not give spectroscopic information but describe the breathing modes of nuclear oscillations. The higher order degrees of freedom describe oscillations of the nuclear surface, such as $\lambda = 2$: quadrupole and $\lambda = 4$: hexadecapole, for axially symmetric shapes and $\lambda = 3$: octupole, for reflection asymmetric nuclei. For axially symmetric nuclei the nuclear shape may be described by:

$$\begin{aligned} R(\theta) &= C R_0 \left[1 + \sqrt{\tfrac{2\lambda+1}{4\pi}} \textstyle\sum_\lambda \beta_\lambda P_\lambda(\cos\theta) \right] \\ &= C R_0 \left[1 + \sqrt{\tfrac{5}{4\pi}} \beta_2 P_2(\cos\theta) + \sqrt{\tfrac{9}{4\pi}} \beta_4 P_4(\cos\theta) \right] \end{aligned} \tag{1.2}$$

where $P_\lambda(cos\theta)$ are Legendre polynomials. This expression introduces the β_λ deformation parameters.

1.1.2 Collective Rotations

The mechanism for nuclear collective rotation is only observed in nuclei with non-spherical shapes as rotations about a symmetry axis are quantum mechanically forbidden. In deformed nuclei, the total angular momentum **I** is obtained by vectorially adding the rotational angular momentum **R** and the intrinsic angular momentum **J**,

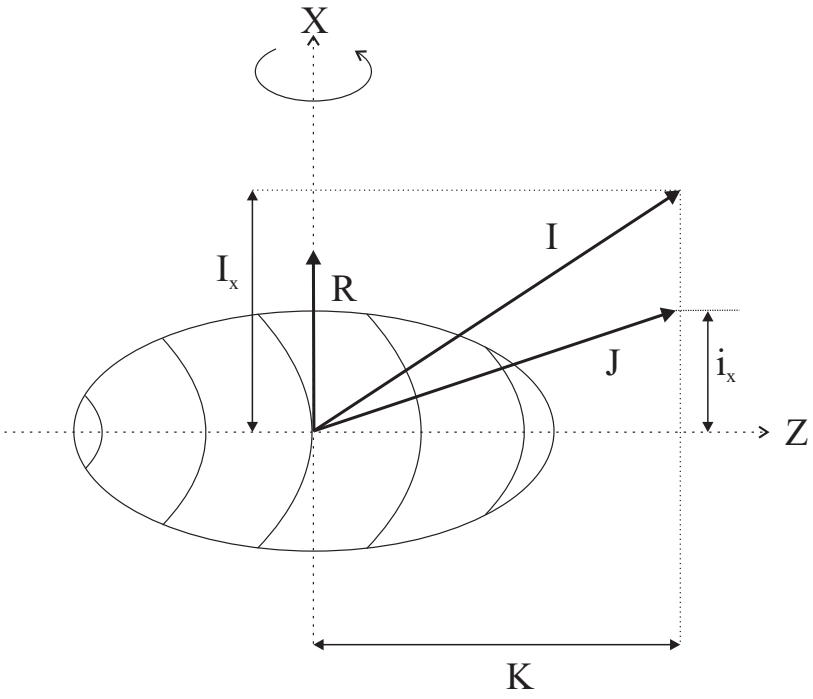

Figure 1.2: Schematic of the nuclear angular momentum and its components.

where **J** is the sum of the intrinsic angular momentum of the individual valence nucleons $\mathbf{J} = \sum \mathbf{j}$. Figure 1.2 shows the coupling of the angular momentum of the valence and core nucleons. For axially symmetric nuclei the collective angular momentum **R** is perpendicular to the symmetry axis, therefore the projection of **I** and **J** on the symmetry axis is the same and denoted by K.

The expression for the kinetic energy of a classic rotating rigid body is given by:

$$E_{rot} = \frac{1}{2}\Im\omega^2 = \frac{I^2}{2\Im}; \omega = \frac{I}{\Im} \tag{1.3}$$

where $\Im$ is the moment of inertia. The collective rotation of a deformed nucleus results in a sequence of states with increasing energy. The states, with increasing I, exhibit in an increase in energy proportional to $I(I+1)$:

$$E_{rot}(I) = \frac{\hbar^2}{2\Im^{(0)}} I(I+1) \tag{1.4}$$

where $\Im^{(0)}$ defines the static moment of inertia. This sequence of states is called a rotational band of $E2$ transitions $E_\gamma \simeq 2\hbar\omega$. In addition to the static moment of

inertia the kinematic moment of inertia and dynamic moment of inertia are also used to describe the nuclear behaviour under rotation. The kinematic moment of inertia, $\Im^{(1)}$, is defined as:

$$\Im^{(1)} = I_x \hbar^2 \left[\frac{dE}{dI_x}\right]^{-1} = \hbar \frac{I_x}{\omega} \tag{1.5}$$

and the dynamic moment of inertia, $\Im^{(2)}$, is defined as:

$$\Im^{(2)} = \hbar^2 \left[\frac{d^2E}{dI_x^2}\right]^{-1} = \hbar \frac{dI_x}{d\omega} \tag{1.6}$$

where I_x is the projection of I onto the rotation axis, given by:

$$I_x = \sqrt{I(I+1) - K^2}. \tag{1.7}$$

The experimental aligned angular momentum i_x is defined as:

$$i_x = I_x - I_{x,ref} \tag{1.8}$$

where the reference alignment I_{ref} is defined as:

$$I_{ref} = \left(\Im_0 + \omega^2 \Im_1\right) \omega. \tag{1.9}$$

The experimental aligned angular momentum i_x subtracts a rotational reference. At low spin, the nuclear moment of inertia is roughly proportional to the square of the rotational frequency. It follows that the energy reference is based on a Variable Moment of Inertia (VMI), which introduces the Harris parameters $\Im_0$ and $\Im_1$ [Harr65]. These parameters are found by applying a least squares fit to the states of a reference band of choice, for example the yrast states of a ground state band. The alignment i_x is plotted against rotational frequency to investigate the differences between various configurations.

In practice, the nucleus is not a rigid rotor and experimentally measured values for the moment of inertia are smaller than rigid-body values. Due to pairing effects nuclear matter can behave like a fluid. Pairs of particles occupy time-reversed orbits, as a result the spins cancel and the pair contribute $I^\pi = 0^+$. Each particle orbits the

nucleus interacting twice per revolution with its paired nucleon, scattering from one orbit to another. The greatest spatial overlap between the two particles occurs when the pair orbit with the bulk of the nuclear matter. Under rotation the nucleus may be considered as a rigid core plus a fluid of valence nucleons. The effect of the pairing of the valence nucleons can be observed in the study of the angular momentum as a function of excitation energy of the nucleus. The rotational motion of the nucleons can be energetic enough for the Coriolis force to become large enough to overcome the pairing force between a specific pair of coupled nucleons. The angular momentum of the uncoupled nucleons is then aligned with respect to the rotational axis. The alignment results in the slowing down of the nuclear rotation frequency as states based on this new configuration become yrast. Such effects can be observed in plots of the aligned angular momentum as a function rotation frequency, with a sharp backbend observed at the frequency at which the alignment occurs. This effect is known as backbending and is interpreted as the crossing of two bands based on different intrinsic configurations, where the configuration of an aligned pair of nucleons has a higher angular momentum than the rotational band built on all the nucleons being paired. The sharpness of the backbend is related to the strength of the interaction between the two bands involved in the crossing.

1.1.3 Nilsson Model

The Nilsson model is a single particle model and provides a microscopic basis for the existence of rotational and vibrational collective motion that is directly linked to the shell model. The Nilsson (or deformed shell) model uses a deformed potential instead of a spherically symmetric potential used in the shell model. The Nilsson model [Nils69] calculates the influence of the deformed nuclear potential on the single particle orbits, the Nilsson potential is based on the deformed harmonic oscillator potential for a spheroidal nucleus deformed along the z-axis, and can be written as:

$$V_{Nilsson} = V_{osc} - \kappa\hbar\omega_0 \left[2\mathbf{l}.\mathbf{s} + \mu\left(\mathbf{l}^2 - \langle\mathbf{l}^2\rangle_N\right)\right]. \tag{1.10}$$

Here, κ and μ are adjustable coupling strength parameters which can be obtained by fitting to experimental energy levels and are different for each major oscillator shell. The **l.s** term is the spin-orbit coupling term which is included to reproduce the observed major shell gaps at magic numbers. This term splits the otherwise degenerate levels with $j = l \pm 1/2$. The $(\mathbf{l}^2 - \langle \mathbf{l}^2 \rangle_N)$ term is introduced to give a more realistic shape by flattening the potential as nucleons near the surface feel a stronger potential than those nearer the core. The first term in the Nilsson potential (equation 1.10) is the deformed harmonic oscillator potential, which can be written as [Beng89]:

$$V_{osc} = \frac{1}{2} M \left[\omega_\perp^2 \left(x^2 + y^2 \right) + \omega_z^2 z^2 \right] \tag{1.11}$$

where $\omega_\perp$ and ω_z represents the frequencies of the simple harmonic motion perpendicular and parallel to the nuclear symmetry axis, respectively, and are inversely proportional to length on each axis of the deformed shape. Deformation is introduced along the z-axis, the nucleus, therefore, is axially symmetric about the z-axis. The oscillation frequencies can be expressed in terms of the deformation parameter δ ($\simeq 0.95\beta_2$) if they are expressed as:

$$\omega_\perp = \omega_0 \left[1 - \frac{2}{3}\delta \right] \tag{1.12}$$

$$\omega_z = \omega_0 \left[1 + \frac{1}{3}\delta \right] \tag{1.13}$$

where ω_0 is the harmonic oscillator quantum and for volume conservation $\omega_0^3 = \omega_\perp^2 \omega_z$. The harmonic oscillator quantum ω_0 is taken to be isospin independent and so is calculated separately for protons and neutrons using:

$$\hbar\omega_0 = 41 A^{-1/3} \left[1 \pm \frac{(N-Z)}{3A} \right] \tag{1.14}$$

where the minus sign is used for protons and the positive sign for neutrons.

The energy shift, experienced by the Nilsson states, relative to $\delta = 0$ can be calculated using:

$$\Delta E(Nlj\Omega) = -\frac{2}{3}\hbar\omega_0 \left[N + \frac{3}{2} \right] \delta \frac{[3\Omega^2 - j(j+1)][\frac{3}{4} - j(j+1)]}{[2j-1]j(j+1)[2j+3]}. \tag{1.15}$$

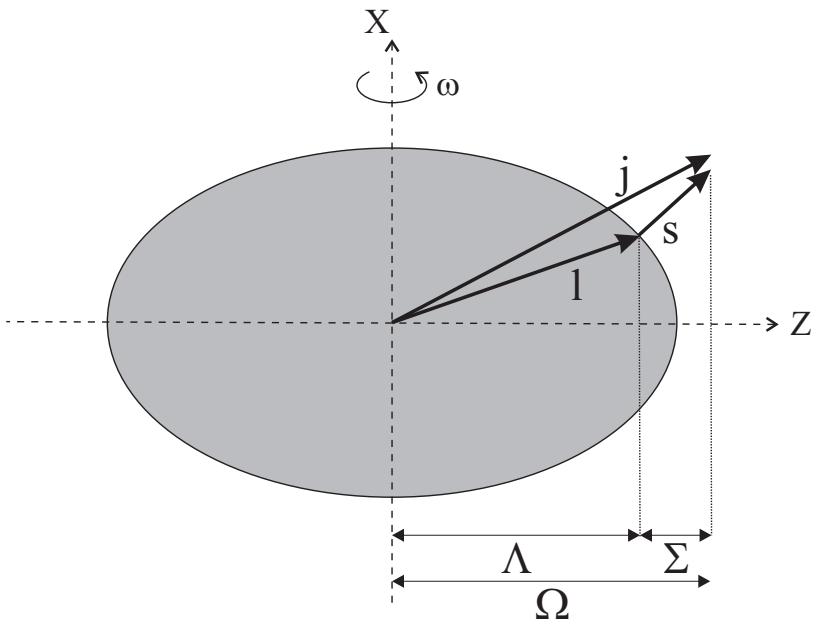

Figure 1.3: Schematic of the quantum numbers used to label the levels of the Nilsson model.

Equation 1.15 shows that the energy shift ΔE is proportional to δ, depends on Ω^2 and is linearly dependent on the oscillator quantum number N. The dependence on N indicates that the Nilsson states slope down more for heavy nuclei, so they are more easily deformed than light nuclei.

For large deformation, the $\mathbf{l.s}$ and $\mathbf{l}^2$ terms are negligible and the energy of the states is given by:

$$E = \hbar\omega_0 \left[N + \frac{3}{2}\right] - \hbar\omega_0 \left[2n_z - n_\perp\right] \frac{1}{3}\delta \tag{1.16}$$

with $N = n_z + n_\perp$. The δ dependence means that the energies of the states are still proportional to the deformation. The gradient of the slope is dependent on n_z and the lowest-lying states at the largest deformations have $n_z = N$ or $n_z = N - 1$, while the highest-lying states have $n_z = 0$ or $n_z = 1$.

The energy levels obtained using the Nilsson model are characterised by the following quantum numbers, as illustrated in figure 1.3:

$$\Omega^\pi \left[N n_z \Lambda\right] \tag{1.17}$$

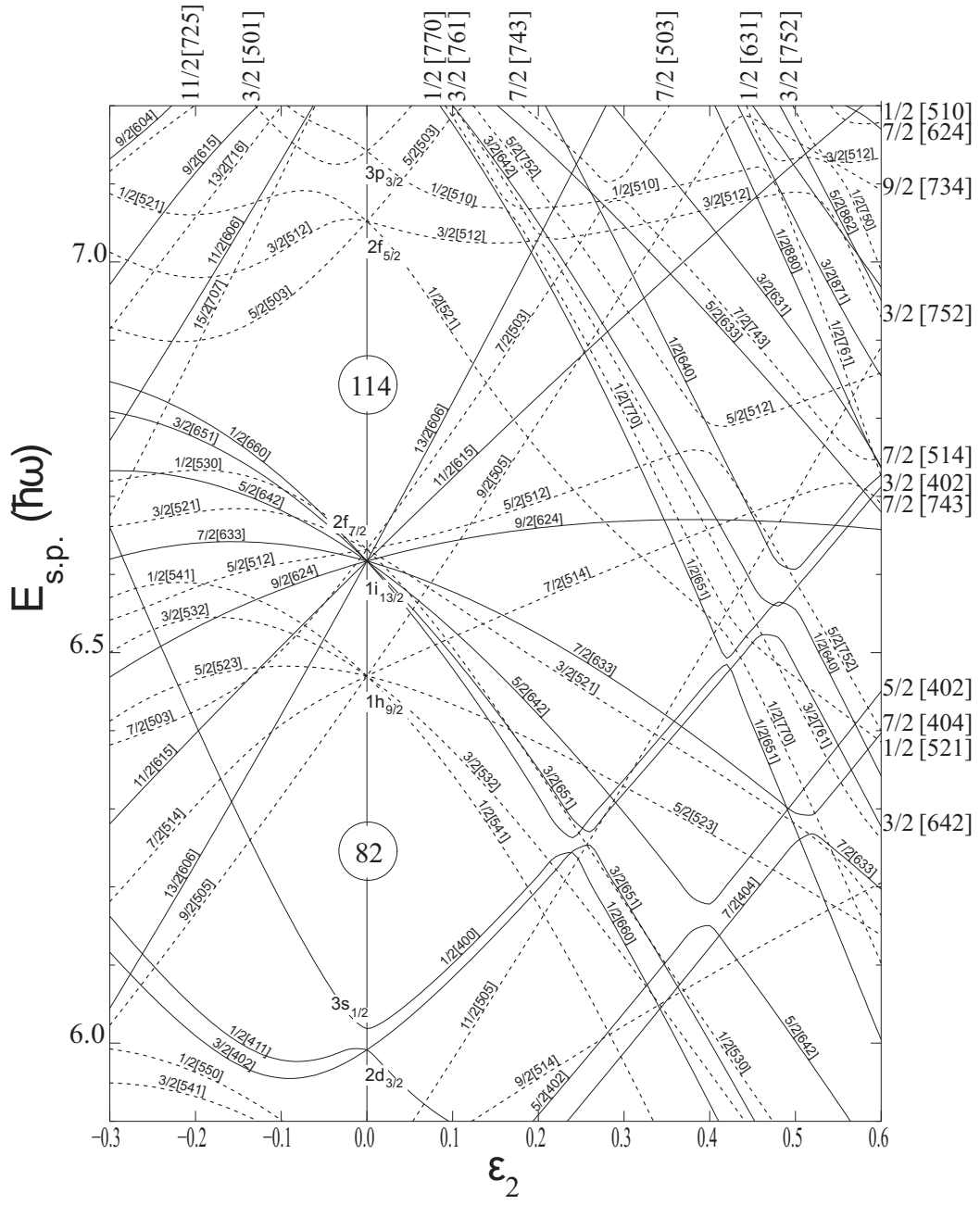

Figure 1.4: A proton Nilsson diagram near the $Z = 82$ shell gap. The quantity ϵ is the deformation parameter used in a non-Cartesian coordinate system used in the Nilsson model approach [Beng89].

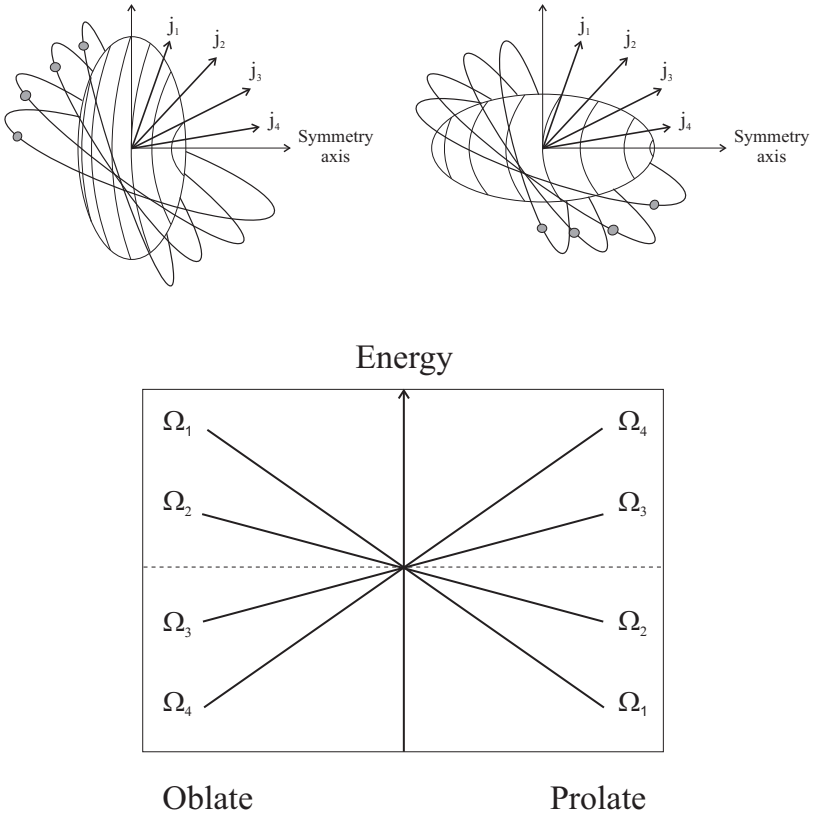

Figure 1.5: Schematic of the splitting of energy levels of different Ω values with different deformation.

where N is the total number of oscillator quanta, n_z the number of oscillator quanta along the symmetry axis, π is parity, Ω is the projection of the total single particle angular momentum j on the symmetry axis, Λ is the projection of the orbital angular momentum l on the symmetry axis and $\Omega = \Lambda + \Sigma$, where Σ ($\pm 1/2$) is the projection of intrinsic spin of the orbit s on the symmetric axis. For even N, $n_z + \Lambda$ must be even and if N is odd then $n_z + \Lambda$ must be odd. Each level is two-fold degenerate.

An example of a Nilsson diagram is shown in figure 1.4. The diagram shows the single particle energy levels as a function of deformation for proton numbers approaching the $Z = 82$ shell gap. The solid lines correspond to positive parity states and the dashed lines negative parity states. Low Ω (high Ω) orbitals have a large spatial overlap with a prolate (oblate) deformed core and are consequently lowered in

energy with increasing prolate (oblate) deformation. The splitting of the energy levels of different Ω values with deformation is shown in figure 1.5. As levels with high Ω values are lowered in energy for oblate deformations this makes it more efficient for the generation of angular momentum by single particle excitations. At zero deformation the magic numbers of the major shell closures appear at regions where the level density is low. The slope of a Nilsson state is related to the single-particle matrix element of the quadrupole operator, given by:

$$\frac{dE_k}{d\beta_2} = -\langle k \mid r^2 Y_{20} \mid k \rangle. \tag{1.18}$$

The principles of the Nilsson model can be understood qualitatively with reference to the behaviour of the states observed in the Nilsson Diagrams. The nuclear force is attractive and so an orbit will have lower energy if it lies close to the rest of the nuclear matter. The energy depends on its orientation with respect to the nuclear symmetry axis, quantified by the projection of the total angular momentum on the symmetry axis, Ω. For a positive quadrupole deformation low Ω values correspond to equatorial motion near the bulk of nuclear matter. That is, orbitals with lower Ω values are more extended in the z direction and so have more nodes in its wave function in the z direction. So for prolate quadrupole deformation, orbits with the largest n_z have the lowest energy. The difference in energy between low Ω is small and increases rapidly as Ω increases. As can be seen in the Nilsson Diagram (figure 1.4) for prolate deformation ($\beta_2 > 0$) the energy drops rapidly with increasing deformation for low Ω values and the separation of adjacent Ω values increases sharply with increasing Ω.

The Pauli principle states that no two particles with the same quantum numbers can occupy the same quantum mechanical state. The Ω and n_z dependence of the energy means that as deformation changes some of the Nilsson states will approach each other. The consequence of the Pauli principle is that levels with the same Ω and π values interact and repel each other. Each Nilsson trajectory is linear with respect to β_2 but will curve as it approaches another state of the same Ω and π. A feature of the Nilsson diagram is that the highest Ω orbitals are very straight due to the lack of nearby j-shells with the same high Ω component with which they can

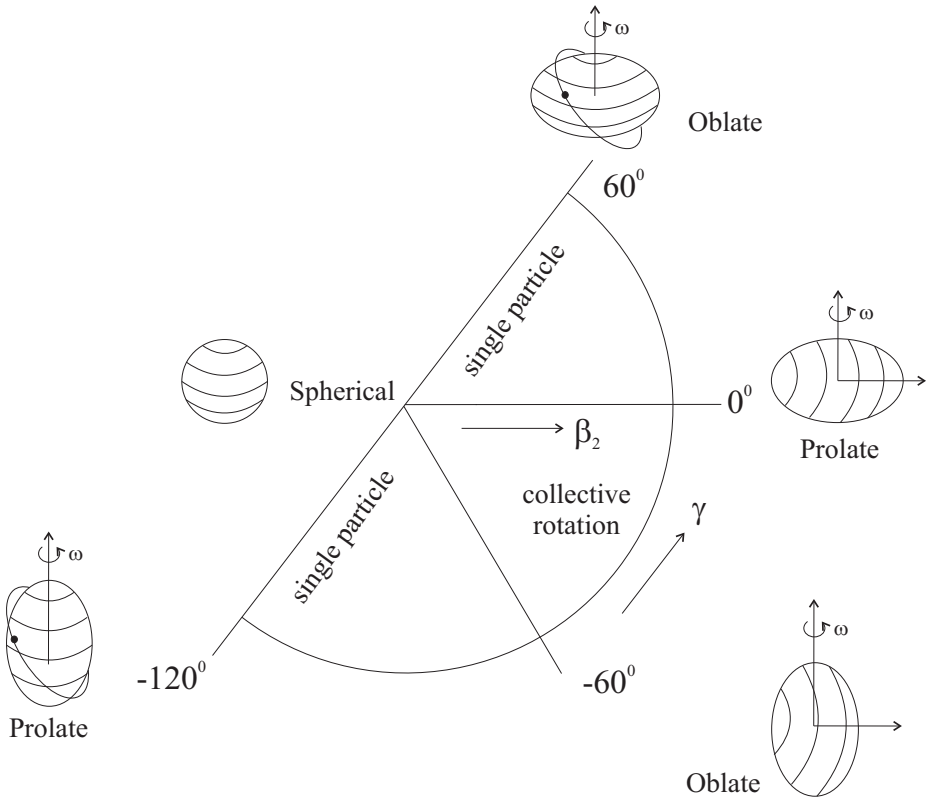

Figure 1.6: Schematic of the Lund Convention for describing quadrupole shapes.

mix. Also orbitals with the opposite parity can intrude into a lower shell at a larger deformation. These intruder orbitals do not mix with the nearby orbitals as the parities are opposite, therefore they are very pure states.

1.2 Quadrupole Deformation

The forces between nucleons outside a major closed shell can be described as residual interactions. The 2^{λ}-pole interactions act most strongly between nucleons in $\Delta j = \Delta l = \lambda$. These interactions have a short range and therefore only act between orbitals that lie physically close together. Orbits within a major shell typically have $\Delta j = \Delta l = 2$, and so the quadrupole ($\lambda = 2$) interaction is usually the most important. Nucleons subjected to the quadrupole interaction will move in quadrupole

shaped orbits. With many nucleons in these orbits, and a strong quadrupole interaction, quadrupole vibrations or deformations of the nucleus can result.

In case of quadrupole deformation, if the $\alpha_{2\mu}$ coefficients of equation 1.1 are defined in the system of principle axes, $\alpha_{22} = \alpha_{2-2}$, $\alpha_{21} = \alpha_{2-1} = 0$ and:

$$R(\theta, \phi) = CR_0 \left[1 + \alpha_{20} Y_2^0(\theta, \phi) + \alpha_{22} \left(Y_2^2(\theta, \phi) + Y_2^{-2}(\theta, \phi)\right)\right] \tag{1.19}$$

then the five $\alpha_{2\mu}$ coefficients are reduced to two independent variables α_{20} and α_{22}. These coefficients can be expressed in terms of the deformation parameters β_2 and γ:

$$\begin{aligned} \alpha_{20} &= \beta_2 \cos\gamma \\ \alpha_{22} &= \tfrac{1}{\sqrt{2}} \beta_2 \sin\gamma \end{aligned} \tag{1.20}$$

where β_2 represents the extent of quadrupole deformation while γ represents the degree or axial asymmetry.

The deformation parameters β_2 and γ describe the shape of the nucleus as defined by the Lund convention, illustrated in figure 1.6. The parameter β_2 measures the total quadrupole deformation:

$$\beta_2^2 = \sum_{\mu} \mid \alpha_{2\mu} \mid^2 \tag{1.21}$$

while the parameter γ measures the lengths along the principal axes:

$$\begin{aligned} \delta R_x &= \sqrt{\tfrac{5}{4\pi}} \beta_2 R_0 \cos(\gamma - \tfrac{2\pi}{3}) \\ \delta R_y &= \sqrt{\tfrac{5}{4\pi}} \beta_2 R_0 \cos(\gamma - \tfrac{4\pi}{3}) \\ \delta R_z &= \sqrt{\tfrac{5}{4\pi}} \beta_2 R_0 \cos(\gamma). \end{aligned} \tag{1.22}$$

For γ values that are a multiple of 60°, two δR_i values are always identical since the nucleus is axially symmetric. Values of $\gamma = 0°$ and $-120°$, $\beta_2 > 0$ corresponds to a prolate (rugby ball) shape, while values of $\gamma = +60°$ and $-60°$, $\beta_2 < 0$ corresponds to an oblate (disc) shapes. The shapes at $\gamma = 0°$ (prolate) and γ = -60° represent collective motion. At $\gamma = -120°$ (prolate) and $\gamma = +60°$ the symmetry axis coincides

with the rotation axis resulting in non collective shapes (single particle). If γ is not a multiple of 60° the nucleus is said to be triaxial where all three of the axes are of different lengths.

1.2.1 Deformed Woods-Saxon Potential

The Woods-Saxon potential reproduces the single-particle state energies well in heavy nuclei. The surface diffuseness, described by the parameter a, is roughly constant in spherical nuclei. To obtain such a constant surface diffuseness in deformed nuclei requires the dependence of a on the angles θ, ϕ. The deformed Woods-Saxon potential may be written as [Bohr75]:

$$V_{ws}(r, \beta) = -V_0 \left[1 + \exp\left(r - R(\theta, \phi)/a(\theta, \phi)\right)\right] \tag{1.23}$$

where $r - R(\theta, \phi)$ is the distance between the point r and the nuclear surface $R(\theta, \phi)$. Similar to the Harmonic Oscillator Potential, a term proportional to $\mathbf{l}.\mathbf{s}$ is added in order to produce the correct magic numbers. Deformed Wood-Saxon potentials are used to calculate the single particle levels for protons and neutrons discussed in Chapters 3 and 4.

1.3 Electromagnetic Transitions

Most nuclear reactions and some radioactive decay processes leave the nucleus in an excited state, which usually decay via γ-ray emissions. Gamma rays are a type of electromagnetic radiation with wavelengths typically a million times smaller than visible light. When γ rays are emitted between excited states in a nucleus, the recoil momentum given to the nucleus us usually about 1 part in 10^5 and therefore can be neglected. This approximation means that the γ-ray energy corresponds to the difference in the energies of the nuclear states involved in the transition, usually between 0.1 and 10 MeV. Electromagnetic transitions obey the following angular momentum and parity π selection rules:

$$| I_i - I_f | \leq L \leq I_i + I_f \quad \forall\ L \neq 0,$$
$$\Delta\pi = \text{no: } L = \text{even for electric, } L = \text{odd for magnetic,}$$
$$\Delta\pi = \text{yes: } L = \text{odd for electric, } L = \text{even for magnetic,}$$

where I_i and I_f and the angular momenta of the initial and final states, respectively, and L is the multipolarity of the radiation, L cannot equal 0 because the photon has an intrinsic spin of 1. If the γ-ray carries the difference in angular momenta of the initial and final states then the transition is said to be stretched.

The electromagnetic radiation field can be described mathematically in terms of a multipole moment expansion. The terms correspond to 2^L-poles and the lowest terms are labelled as so: $L = 0$ (monopole), $L = 1$ (dipole), $L = 2$ (quadrupole), $L = 3$ (octupole). The multipole moments are dependent on charge and current densities and so can provide information on these properties of the nucleus. For example, the $E2$ moments are sensitive to the nuclear charge. A study of the $E2$ moments therefore gives information on collective effects such as deformation.

The γ-ray transition probability, $\lambda(L)$, between the initial and final states with angular momentum I_i and I_f, respectively, is given by:

$$\lambda(L) = \frac{1}{\tau} = \frac{8\pi(L+1)}{\hbar L[(2L+1)!!]} \left(\frac{E_\gamma}{\hbar c}\right)^{2L+1} B(\sigma L; I_i \rightarrow I_f), \tag{1.24}$$

where τ is the mean lifetime of the state, $B(\sigma L; I_i \rightarrow I_f)$ is the reduced transition probability, E_γ is the energy difference between the initial and final states, L indicates the multipole of the radiation ($L = 1$ for dipole, $L = 2$ for quadrupole and so on) and σ indicates the character of the transition (E for electric and M for magnetic).

1.3.1 Reduced Transition Probability

The reduced transition probability is defined as:

$$B(\sigma L; I_i \rightarrow I_f) = \frac{1}{2I_i + 1} \mid \langle I_f \| \sigma L \| I_i \rangle \mid^2 \tag{1.25}$$

where σL is the electromagnetic multipole operator and the reduced matrix element $\mid \langle I_f \| \sigma L \| I_i \rangle \mid^2$ contains all the information on the nuclear wave functions of the

$B(E1) = 0.06446\mathrm{A}^{2/3}$ $(\mathrm{e}^2\mathrm{fm}^2)$	$B(M1) = 1.7905$ (μ_N^2)
$B(E2) = 0.05940\mathrm{A}^{4/3}$ $(\mathrm{e}^2\mathrm{fm}^4)$	$B(M1) = 1.6501\mathrm{A}^{2/3}$ $(\mu_N^2\mathrm{fm}^2)$
$B(E3) = 0.05940\mathrm{A}^{2}$ $(\mathrm{e}^2\mathrm{fm}^6)$	$B(M3) = 1.6501\mathrm{A}^{4/3}$ $(\mu_N^2\mathrm{fm}^4)$

Table 1.1: Weisskopf single-particle strengths.

B(E1) $\sim 10^{-2}$ W.u.
B(M1) $\sim 10^{-1}$ W.u.
B(E2) $\sim 10^{2}$ W.u.

Table 1.2: Typical values of reduced transition strengths.

initial and final states. In measuring the reduced transition probability information about the nuclear wave function can be deduced giving direct information about the structure of the initial and final states.

Within the Weisskopf model, an electric transition is assumed to result from the excitation of a single proton, from one shell model state to another, excited in an average central potential. A magnetic transition occurs when the intrinsic spin is flipped, for example $j_1 = l_1 \pm 1/2 \rightarrow j_2 = l_2 \mp 1/2$. The Weisskopf single particle estimates assume a uniform charge distribution and, while quite limited, provide a useful scale with which to compare experimental reduced transition probabilities $B(E\lambda)$ and $B(M\lambda)$, these are listed in table 1.2. Typical experimental values are listed in table 1.2.

Simple estimates of the transition rates have been calculated for the case where the transition is assumed to be due to a single proton changing from one shell-model state to another [Kran88]. The EL and ML transition rates are given by:

$$\begin{aligned} T(EL) &= \tfrac{8\pi(L+1)}{L[(2L+1)!!]^2}\tfrac{e^2}{4\pi\epsilon_0\hbar c}\left(\tfrac{E}{\hbar c}\right)^{2L+1}\left(\tfrac{3}{L+3}\right)^2 cR^{2L} \\ T(ML) &= \tfrac{8\pi(L+1)}{L[(2L+1)!!]^2}\left(\mu_p - \tfrac{1}{L+1}\right)^2\left(\tfrac{\hbar}{m_p c}\right)^2\left(\tfrac{e^2}{4\pi\epsilon_0\hbar c}\right)\times\left(\tfrac{E}{\hbar c}\right)^{2L+1}\left(\tfrac{3}{L+2}\right)^2 cR^{2L-2} \end{aligned} \quad (1.26)$$

where m_p represents the mass of the proton. The transition rate is in s^{-1} and the

$\mathrm{T(E1)} = 1.590\times10^{15}E_\gamma^3B(E1)$	$\mathrm{T(M1)} = 1.758\times10^{13}E_\gamma^3B(M1)$
$\mathrm{T(E2)} = 1.225\times10^{9}E_\gamma^5B(E2)$	$\mathrm{T(M1)} = 1.355\times10^{7}E_\gamma^3B(M2)$
$\mathrm{T(E3)} = 5.708\times10^{2}E_\gamma^7B(E3)$	$\mathrm{T(M3)} = 6.313E_\gamma^7B(M3)$

Table 1.3: Transition rates for the lowest multipoles.

γ-ray energy E_γ is in MeV. The ML transition probability also includes a factor that depends on the nuclear magnetic moment μ_p of the proton. With $R = R_0A^{1/3}$, estimates can be made to give the transition probabilities known as the Weisskopf estimates, these are listed in table 1.3.

For example, if the transition rate is much greater than the Weisskopf estimate than one may infer that more than one single nucleon is responsible for the transition and more collective behaviour is being observed. Weisskopf estimates are often used as the units of real collective transition rates. The Weisskopf unit (W.u.) represents a transition strength calculated using:

$$\frac{T(\sigma L)_E}{T(\sigma L)_W} \tag{1.27}$$

where $T(\sigma L)_W$ represents the Weisskopf estimates of transition rates listed in table 1.3.

1.3.2 Reduced Transition Probability and Quadrupole Moment

The electric quadrupole moment provides a measure of the charge distribution of the nucleus and is dependent on the charge density ρ and the angle θ subtended by the radial vector $\mathbf{r}$. The intrinsic quadrupole moment Q_0 is defined in the intrinsic frame of reference and is zero for nuclei that have a spherically symmetric charge distribution, negative for oblate nuclei and positive for prolate nuclei. For the collective excitations in deformed nuclei the enhanced de-excitation mode is the electric quadrupole transition $E2$. For an $E2$ transition with $\Delta I = 2$ the reduced transition

probability can be extracted from equation 1.24 and can be written as:

$$B(E2) = \frac{0.0816}{E_\gamma^5 \, (1 + \alpha_{tot}) \, \tau} \; e^2 b^2 \tag{1.28}$$

where α_{tot} is the total internal conversion coefficient and, the lifetime τ is in units of ps and E_γ is in units of MeV. The reduced transition probability from an $I \rightarrow I - 2$ $E2$ transition for an axially symmetric deformed rotating nucleus is given as [Bohr75]:

$$B(E2; I_i \rightarrow I_f) = \frac{5}{16\pi} e^2 Q_t^2 \langle I_i K_i 20 \mid I_f K_f \rangle^2 \tag{1.29}$$

where Q_t is the transition quadrupole moment. Assuming a well behaving rotor the transitional quadrupole moment can be considered equal to the intrinsic quadrupole moment Q_0 which, in terms of the reduced matrix element, is defined as:

$$Q_0 = \sqrt{\frac{16\pi}{5}} \langle I_i K_i \mid E2 \mid I_f K_f \rangle^2. \tag{1.30}$$

The square of the transitional quadrupole moment is proportional to the reduced transition probability, as shown in equation 1.29, which in turn is inversely proportional to the lifetime of the state. The experimentally measured lifetime of a state can, therefore, provide a direct measure of the difference between the intrinsic configurations of the initial I and final $I - 2$ states. For example, a small difference in the intrinsic configurations occurring between the initial and final states will be reflected in a high Q_t value and the $B(E2)$ value will reflect the collectivity of the transition. Typical values for the collective transitions in deformed nuclei are of the order of 100 - 1000 Weisskopf units (W.u.).

The deformation parameter β_2, as described in sections 1.1 and 1.2, represents the extent of quadrupole deformation and is related to the eccentricity of an ellipse as:

$$\beta_2 = \frac{4}{3} \sqrt{\frac{\pi}{5}} \frac{\Delta R}{R_{ave}} \tag{1.31}$$

where ΔR is the difference between the semi-major and semi-minor axes of the ellipse and R_{ave} is the average nuclear radius and is equal to $R_0 A^{1/3}$. By assuming a uniform charge distribution the intrinsic quadrupole moment can be related to β_2 using:

$$Q_0 = \frac{3}{\sqrt{5\pi}} Z R^2 \beta_2 \, (1 + 0.16\beta_2) \;\; eb \tag{1.32}$$

where Z is the atomic number, $R = R_0 A^{1/3}$.

Chapter 2

Experimental Methods and Apparatus

The accelerator laboratory at the University of Jyväskylä, Finland, provides a setting for the lifetime measurements of excited states in nuclei far from stability. The facility consists of the JUROGAM Ge-detector array coupled to the RITU [Lein97] gas-filled separator and the GREAT spectrometer [Page03] at the focal plane of RITU. The Köln plunger device was installed at the JUROGAM target position. At this facility the data acquisition is a triggerless Total Data Readout (TDR) system [Laza01], which allows for the collection of all the data independently read out from each detector element. In this chapter the principles involved with fusion evaporation reactions and general description of the experimental methods used is discussed.

2.1 Heavy-ion Fusion Evaporation

The nuclei investigated in this thesis are neutron deficient: $^{175}_{79}$Au has 22 neutrons fewer than the stable Au isotope, $^{174}_{78}$Pt and $^{175}_{78}$Pt have 21 and 20 fewer neutrons than the lightest stable Pt isotope, respectively. These neutron-deficient nuclei are produced in a fusion-evaporation reaction using a stable target and beam fused together and form a compound nucleus. For fusion to occur the two nuclei must come close

enough to one another and overcome the Coulomb barrier.

The combination of beam, beam energy and target is chosen such that the nuclei of interest can be populated strongly. The amount of angular momentum transferred into the compound nucleus is given by $\mathbf{l} = m(\mathbf{v} \text{ x } \mathbf{b})$, therefore projectiles of higher velocity or heavier mass will introduce more angular momentum into the compound nucleus, allowing for studies of nuclei to high spin along the yrast line.

For beam energies greater than the Coulomb barrier, fusion can readily take place with the compound system typically forming within 10^{-20} s. One feature of fusion reactions is the compound nucleus retains no memory of the entrance channel. The excitation energy of the compound system E^* can be expressed as,

$$E^* = Q + E_{th} = \frac{M_t}{M_t + M_p} E_p[MeV] \tag{2.1}$$

where E_p is the projectile energy and E_{th} is the threshold energy.

If the compound nucleus is stable against fission, the excitation energy is released via particle and γ-ray emissions. Within 10^{-19} s after impact, nucleon evaporation occurs, resulting in the production of excited residual nuclei. The emitted nucleons carry away at least their binding energy (8-10 MeV) but little angular momentum. When the excitation energy is reduced to below the particle emission energy threshold ≈ 8 MeV above the yrast line, the residual nuclei will lose excitation energy via the emission of dipole ($E1$) γ-ray emission. This process is know as statistical (cooling) γ-ray emission and occurs 10^{-15} s after impact. Once more, in this process little angular momentum is removed and so the nucleus exists in a state of high angular momentum. The dipole radiation continues to be emitted until the nucleus reaches the yrast line at which point quadrupole ($E2$) γ-ray emission dominates. The yrast line denotes the lowest energy for a given spin. The residual nucleus loses angular momentum as the quadrupole γ-ray emission allows the nucleus to cascade down from one level to the next, this occurs 10^{-12} s after impact. After 10^{-9} s the residual nucleus reaches its ground state, and if the nucleus is not stable, radioactive decay will occur. The fusion-evaporation process described is illustrated in figure 2.1.

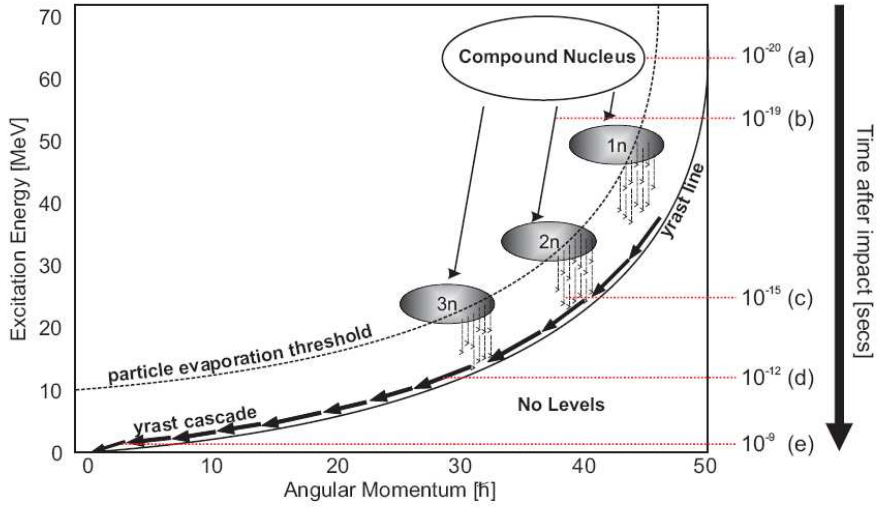

Figure 2.1: A schematic diagram to illustrate the process of energy and spin lost by nuclei, stable against fission, following a fusion evaporation reaction [Darb06].

2.2 The JUROGAM II germanium detector array

The JUROGAM II hyper-pure germanium (HP-Ge) detectors are positioned around the target position and are used to detect prompt γ radiation emitted from the nuclei produced following heavy-ion fusion evaporation reactions. In γ-ray spectroscopy the photopeak resolution is of great importance, especially in lifetime measurements as the separation of the two components of the photopeak are essential. JUROGAM consists of 15 EUROGAM Phase I Compton suppressed Ge detectors [Beau92] and 24 Clover EUROGAM II Ge detectors [Duch99]. The 39 Ge detectors are arranged in four angular groups with two rings of Phase I detectors (five at 157.6° and ten at 133.6°) and two rings of Clover detectors (twelve at 105° and twelve at 76°).

2.2.1 Phase I detectors

The Phase I Ge detectors, shown in figure 2.2, consist of a large coaxial n-type HPGe crystal of length 75 mm, diameter 70 mm and the front 30 mm is tapered at and angle

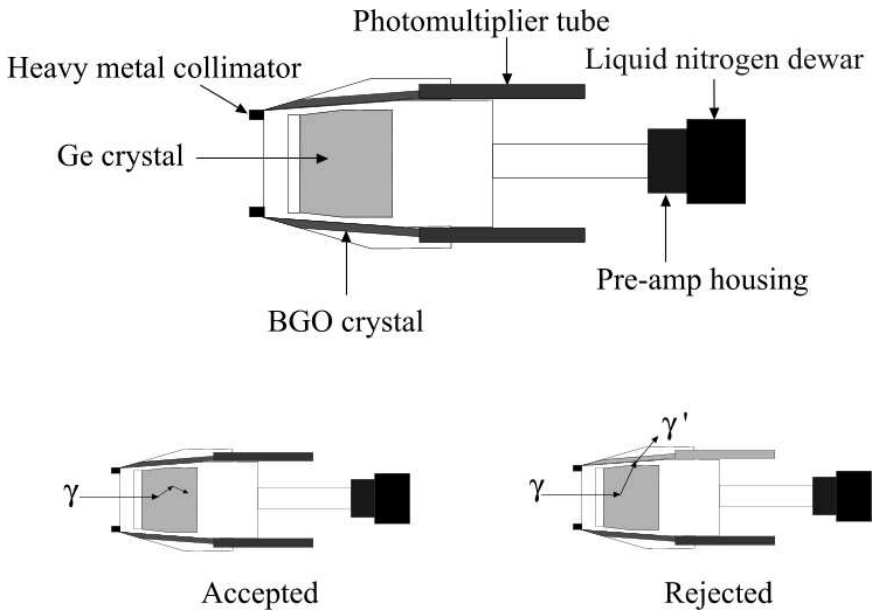

Figure 2.2: A schematic of a Phase I HP-Ge detector and an illustration of the concept of Compton suppression.

of 5.7° [Nola94]. The detectors have been designed for maximum coverage of the target position. The n-type detectors are the preferred choice for γ-ray spectroscopy as the thinner outer p^+ contact minimises the attenuation of γ rays and is less susceptible to radiation damage than p-type detectors.

2.2.2 Clover detectors

For the detectors placed around 90° with respect to the beam direction, Doppler broadening of the γ ray is an issue. One way to reduce the effect of Doppler broadening is to use a Clover detector, shown in figure 2.3, which is a composite Ge detector containing four HP-Ge crystals. The photopeak detection efficiency and the solid angle coverage that can be obtained with a composite detector is much larger than for a single crystal detector. The granularity of a composite detector leads to a reduction in the Doppler broadening of γ rays emitted by recoiling nuclei as the detector opening angle is reduced [Duch99]. The Clover detector consists of four coaxial n-type Ge

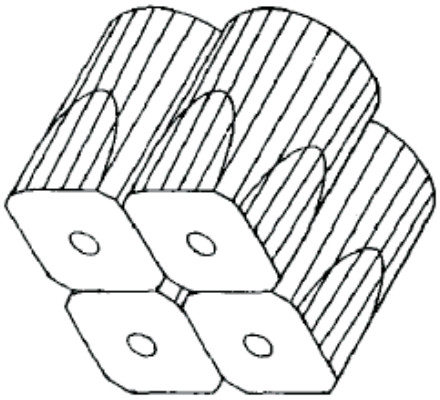

Figure 2.3: A schematic of the Clover detector, showing the arrangement of the four Ge crystals.

crystals of 50 mm diameter and 70 mm length mounted in a common cryostat.

The Clover detector can be used in two modes. Direct detection mode is where each crystal is used as a single detector and the signals from each detectors are treated separately. Coincidence detection mode is where two or more crystals are in temporal coincidence with each other. These coincidence events are mainly related to Compton scattering of the γ ray from one crystal to its neighbours and the γ ray deposits a fraction of its energy into two or more crystals. The total energy, E_γ, is recovered by summing the partial energies. This method of adding the energies of the Compton scattered γ ray is known as add-back.

2.2.3 Compton suppression

Each Ge detector is surrounded by a bismuth germanate (BGO) crystal. The length of the BGO crystal is 190 mm and the thickness varies from 20 mm at the back to 3 mm at the front. The BGO crystal acts a veto detector for γ rays scattered from the Ge crystal into the BGO. This reduces the background component caused by multiple Compton scattering of the incident γ ray within the detector crystal as most of the

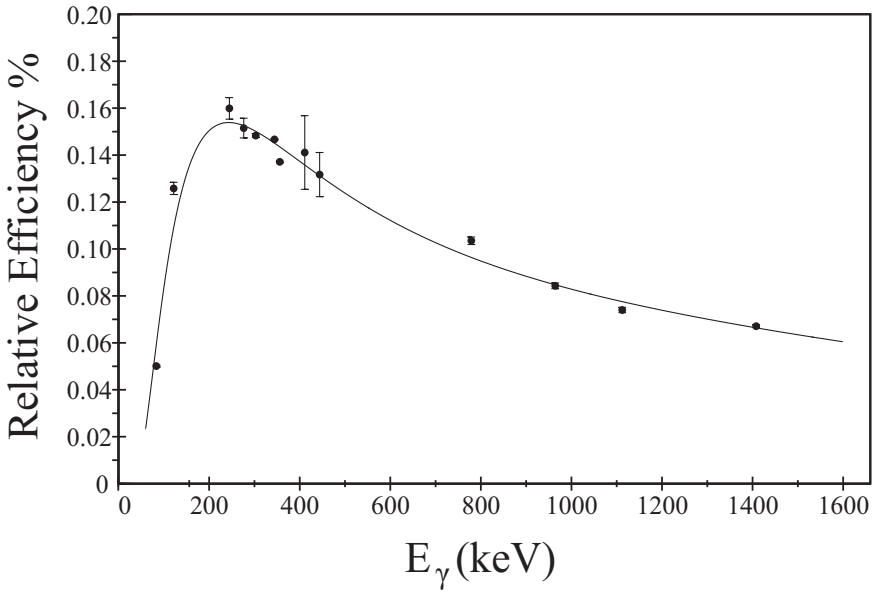

Figure 2.4: Relative efficiency curve of the JUROGAM II array measured using standard ^{133}Ba and ^{152}Eu calibration sources.

incident photons do not deposit their full energy into the detector but rather scatter multiple times before escaping. The use of bismuth germanate for the Compton suppression shield is due to its high atomic number and density which results in a high photoelectric absorption cross section for γ rays. Also bismuth germanate is relatively inexpensive [Beau96].

2.2.4 Efficiency

The efficiency of the JUROGAM spectrometer is a measure of the ratio of the number of γ rays detected to the number of γ rays emitted. The relative efficiency was measured using ^{152}Eu and ^{133}Ba sources of known activity, placed at the target position and the data being collected over a known period of time. Figure 2.4 shows a graph of the relative efficiency curves obtained for the array, with the combination of the Phase I detectors and the Clover detectors. For the Clover detector the total detection efficiency includes add-back. The absolute efficiency of the JUROGAM array was quoted to be 7% at 1332 keV [Duch99].

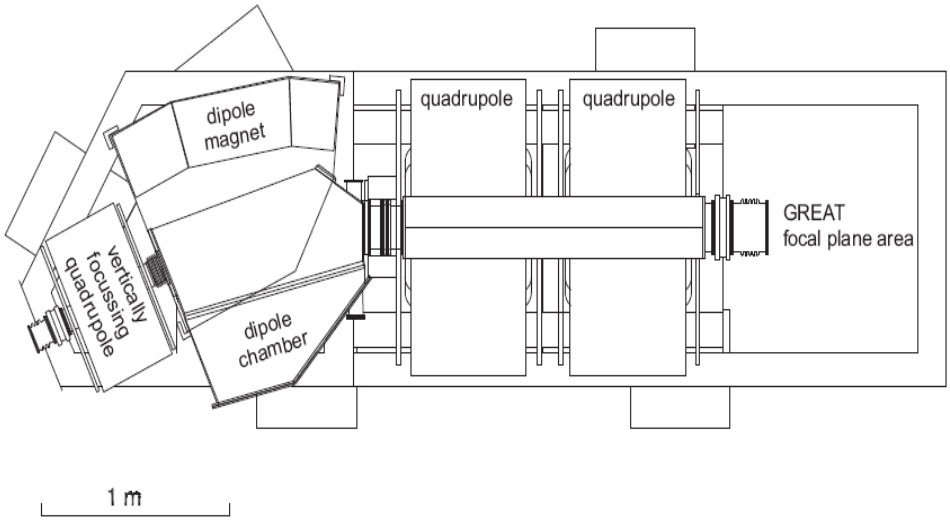

Figure 2.5: A schematic of the RITU separator.

2.3 The Recoil Ion Transport Unit (RITU)

A recoil separator is a powerful tool in studying the heavy-ion-induced fusion evaporation products. The Recoil Ion Transport Unit (RITU) [Lein95], shown in figure 2.5, is a gas-filled recoil separator used to separate, in-flight, the evaporation residues produced with low yields from the beam and other reaction products using magnetic fields. The separation and focusing of the ions is performed by the QDQQ magnetic configuration of RITU, which is located downstream from the target and is coupled to the JUROGAM array. The initial quadrupole magnet matches the recoil cone to the acceptance of the dipole magnet. The dipole magnet separates the beam and fusion products according to their magnetic rigidity. The last two quadrupole magnets focus the recoils on the focal plane detectors. RITU is filled with Helium (He) gas at a pressure of 0.5-3.0 mbar. The helium surrounds the target acting as a coolant and flows continuously through the separator.

With RITU, charge exchange interactions between He gas and ions result in a narrow charge-state distribution. A gas-filled separator like RITU can have trans-

mission efficiencies in the range of 20-50 % compared to vacuum-mode separators such as the Fragment Mass Analyser (FMA), which typically has <10 % transmission efficiency. The increased transmission is essential in fusion evaporation reactions that produce residues with cross sections of the order of nanobarns. The consequence of only having a narrow (average) charge state distribution is that there is no mass selectivity. This is overcome with the use of selective tagging techniques where the characteristic radioactive decay properties of the recoils are used to identify different nuclear species.

2.4 The GREAT Focal Plane spectrometer

The Gamma Recoil Electron Alpha Tagging (GREAT) [Page03] spectrometer, shown in figure 2.6 was designed to measure the decay properties of fusion evaporation reaction products transported to the focal plane of RITU. GREAT comprises a system of silicon, germanium and MWPC detectors. It is designed to detect the implantation of the reaction product as well as spatially and temporally correlate the recoil with its subsequent radioactive decay involving the emission of α particles, β particles, protons, γ rays, X-rays and conversion electrons. Although, GREAT can be employed as a sensitive stand-alone device for decay measurements at the focal plane, it can also provide a selective tag for prompt γ rays measured with the JUROGAM array at the target position. The elements of GREAT used in this experiment are discussed below.

2.4.1 The Multiwire Proportional Counter (MWPC)

The Multiwire Proportional Counter (MWPC) is positioned at the entrance of GREAT. It has an aperture of 131 mm (horizontal) x 50 mm (vertical), with a central vertical 1 mm wide strut to support the thin (0.9 μm) mylar foil entrance and exit widows. The entrance window separates the isobutane gas of the MWPC from the low-pressure helium gas of RITU and the exit window separates the isobutane

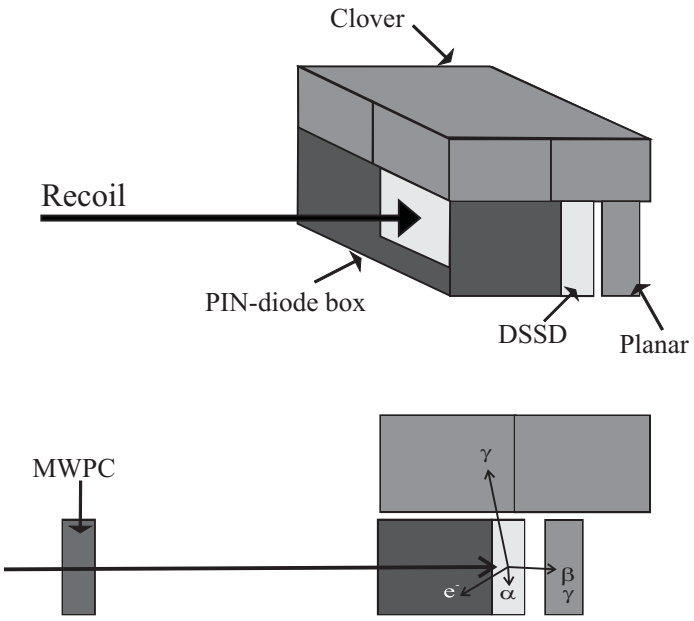

Figure 2.6: A schematic of the GREAT spectrometer.

from the vacuum in which the other GREAT detectors are operated. Ions travelling through the MWPC generate energy-loss, timing and position signals. In conjunction with the DSSDs, the MWPC is used to distinguish between recoiling reaction products passing through it from any subsequent radioactive decay.

2.4.2 The DSSD implantation detectors

After passing through the MWPC the recoils are implanted into a pair of Double-sided Silicon Strip Detectors (DSSDs). Each detector has an active area of 60 mm x 40 mm and a thickness of 300 μm. The DSSDs are divided into 60 vertical and 40 horizontal strips with a strip pitch of 1 mm in both directions giving a total of 4800 detector pixels. The high granularity allows higher implantation rates without compromising decay correlations in comparison to previous focal plane detectors. The two DSSDs are mounted side by side and are separated by a gap of 4 mm, giving an approximate recoil collection efficiency of 85%. A coolant is circulated to reduce their temperature to -20 °C. The DSSDs are used to measure the energies of the ions

that are implanted and of any protons, α particles or β particles they subsequently emit.

2.5 Data acquisition

The experimental setup in Jyväskylä utilises the Total Data Readout (TDR) data acquisition that, unlike conventional data acquisition systems, is triggerless [Laza01]. Conventional systems require a common master trigger from which signals from other detectors are time ordered and read out as part of the same event. This presents a problem of common dead time losses that enforces limitations on Recoil Decay Tagging (RDT) experiments. The TDR method allows the data from every detector to be read out independently as all the electronic channels operate individually in free running singles mode. The information is read out asynchronously by front-end electronics independently of a hardware trigger, overcoming this limitation and eliminating common dead time. As all detector channels are treated independently, data items from the target position and focal plane spectrometer can be collected simultaneously. The data items are associated with a timestamp generated from a global 100 MHz clock with 10 ns precision and the events can then be reconstructed, offline, using temporal and spatial associations within the event builder.

A schematic diagram of the TDR data acquisition system is presented in figure 2.7. In the TDR system, the energy and timing signals come from shaping amplifiers and constant fraction discriminators (CFDs). The analog-to-digital converter (ADC) cards read the data apply a timestamp. The metronome unit controls the clock distribution and maintains synchronisation of all the ADCs. The timestamped data is then time ordered and put into one time ordered stream by the collator and merger units and then sent to the event builder. The event builder unit will pre-filter the data according to any pre-set software trigger condition and reconstruct the events using spatial and temporal correlations.

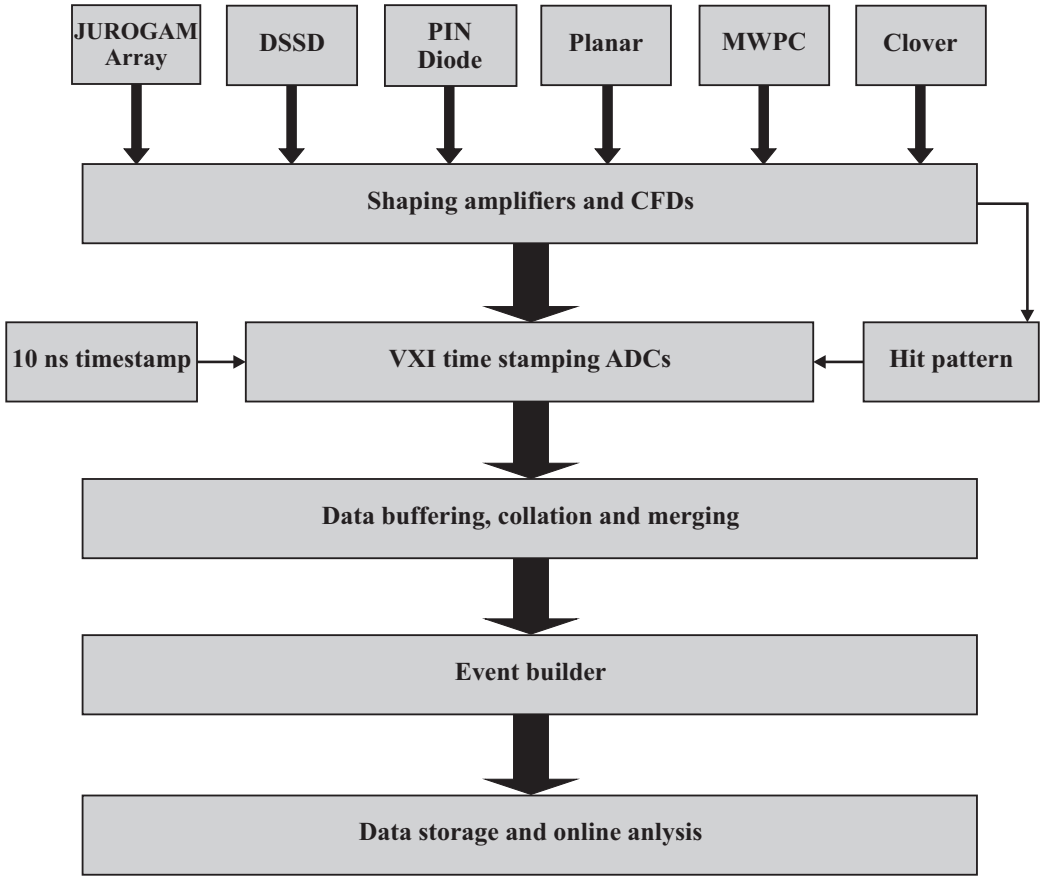

Figure 2.7: Schematic representation of the total data readout data acquisition system [Laza01].

2.5.1 Data Sorting

The data collected using the TDR acquisition system at JYFL is analysed online and offline using the software package GRAIN [Rahk08]. The GRAIN package has been implemented entirely in Java and is used to analyse the raw TDR data stream, sort time-stamped data and perform RDT analysis. Unlike the data emerging from a conventional data acquisition system, the data from the TDR collate and merge layer are not structured or filtered in any way, apart from the time ordering. Temporal and spatial correlations required to form events out of the raw data stream and filtering to remove unwanted or irrelevant data is done entirely in the GRAIN software. That is, channels originating from the same detector are selected from the data stream and temporal and spatially grouped together in a class, for example the DSSD implantation detector. The filter of pile-up events is also performed by GRAIN as well as the Compton suppression of the JUROGAM array. The GRAIN interface utilises the flexibility of the TDR acquisition system by generating a software trigger, thus the trigger conditions and the the trigger width can be varied from one sorting procedure to another using the same data set. In the present work, the software trigger demanded an event in the DSSD implantation detector.

2.6 Tagging techniques

The JUROGAM array located at the target position detects the γ rays emitted from all the reaction products that result from the bombardment of stationary target with a energetic beam of ions. Often only a small fraction of the detected γ rays are emitted by the nucleus of interest, with the rest coming from other fusion evaporation and fission exit channels. In order to associate the γ rays emitted from the nuclei of interest and to suppress the background of other events one has to utilise the techniques of recoil tagging and RDT [Paul95]. These techniques have proved extremely successful in studies of nuclei produced in experiments with low cross sections.

The fusion evaporation reaction products are separated from any fission products

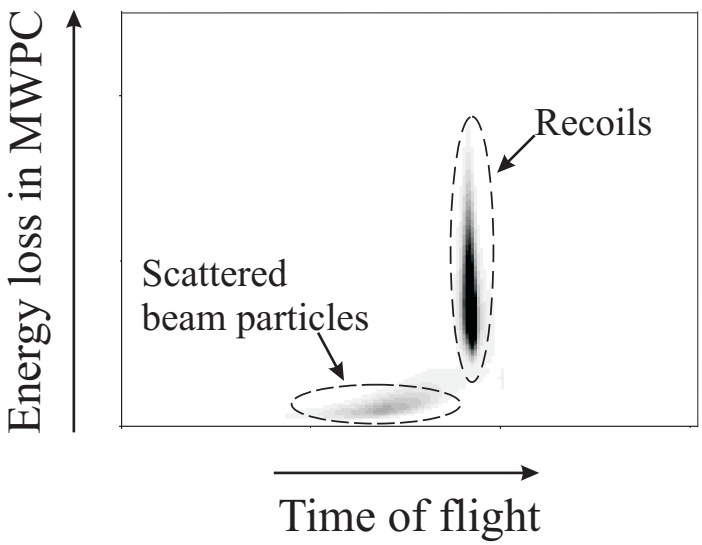

Figure 2.8: Two dimensional spectra showing the energy loss in the MWPC versus the ion time of flight. A two dimensional gate is used to select recoil implantations.

and scattered beam as they pass through RITU. The ions continue to pass through the MWPC and are implanted into the DSSD. The recoils can be separated from any remaining scattered beam by generating an energy loss versus time-of-flight two dimensional spectrum, where the time-of-flight is between the MWPC and DSSD. The two dimensional spectrum for this experiment is shown in figure 2.8. The recoiling fusion products are usually heavier (higher Z) and are transmitted at a lower velocity than the beam particles. Therefore the recoils experience a greater degree of stopping in the isobutane gas. The γ rays can be associated with fusion-evaporation products by setting a two dimensional gate on the identified recoils. This is known as recoil tagging. If the nucleus of interest is the dominant fusion-evaporation product, then recoil tagging can produce a sufficiently background suppressed γ-ray spectrum.

Once the recoil events have been established, the Recoil Decay Tagging (RDT) technique [Paul95] can be used to unambiguously identify the fusion-evaporation products through spatial and temporal correlations of the characteristic radiation decay and implanted recoils. The spatial correlation demands that the charged-particle decay occurs within the same pixel as the recoil while the temporal correlation de-

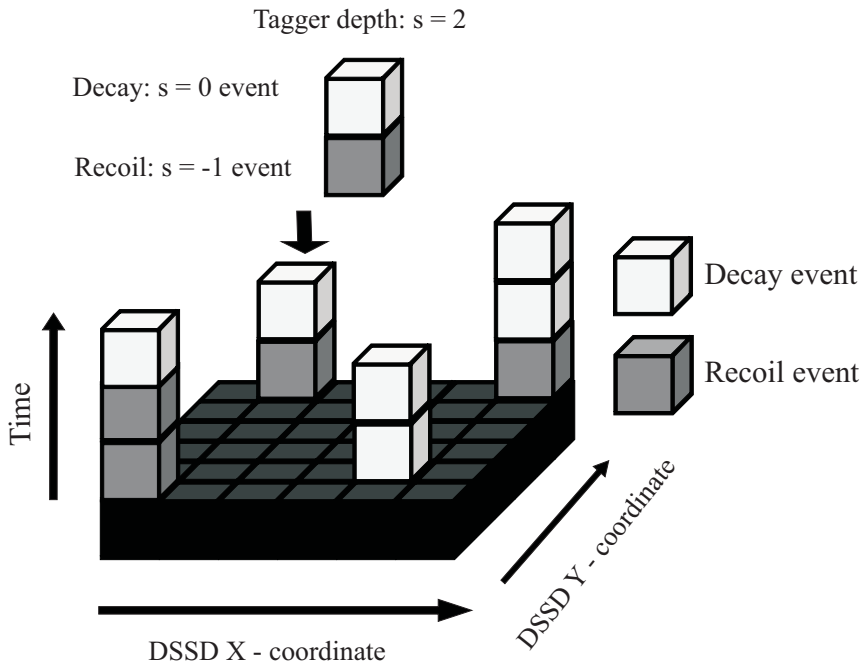

Figure 2.9: A schematic of the DSSD tagger.

mands that the decay occurs with $3 - 5$ half-lives of the implantation. A further energy condition, corresponding to the characteristic energy of the radiation, is then used to uniquely identify a specific nuclide. In this way, any subsequent, and indeed, preceding, radiation can be unambiguously associated with a particular nuclide.

While RDT is a powerful experimental technique, it does have its limitations. In order to be effective the half-life of the characteristic decay must be short in comparison to the time difference between the two consecutive implantations. In addition, the branching ratio of the radioactive decay should be sufficiently large to provide enough statistics in the decay peak to tag on. In the present work, the α decay of the nuclei of interest has been used for identification, however, the RDT method can also be employed for proton and β decaying nuclei as well as γ rays emitted from isomeric states using other detectors contained within the GREAT focal-plane detector.

The correlations made using the RDT technique are constructed in a software

array known as the tagger. A history of the events in each pixel of the DSSD is stored in the tagger. Correlation chains can then be constructed with events that pass the gating conditions discussed above. This method identifies the decay chain associated with a single recoil implant, as all the decay events in a sequence are associated with the recoil until another recoil implantation occurs in the same pixel. Figure 2.9 illustrates the construction of recoil decay events within the DSSD tagger. Figure 2.9 also illustrates a sequence of two recoils followed by a decay event. The first recoil would be ignored and it would be the second recoil associated with the decay event. This scenario could be a false correlation if the decay event is a decay of the first recoil implantation. This scenario can occur if the half-life of the decay is much longer than the rate of implantation.

2.7 The RDDS method

In the Recoil Distance Doppler-Shift (RDDS) method [Schw68], the mean lifetime τ of the nuclear state is related to the time needed by a recoiling nucleus with a velocity $\vec{v}$/c to travel a certain distance d. This method, implemented using the plunger device, is especially suited for fusion-evaporation reactions. An evaporation residue formed in a fusion-evaporation reaction recoils out of the target with a recoil velocity $\vec{v}$/c. In conventional RDDS technique, the evaporation residues are stopped in a stopper foil positioned at a distance $d = v$t directly in front of the target. The energy of a γ ray emitted before reaching the stopper foil is Doppler-shifted according to the equation

$$E = E_0 \left[1 + \frac{v}{c} \cos\theta\right] \tag{2.2}$$

where E_0 is the energy of the γ ray emitted at rest and θ is the angle at which the γ ray is detected relative to the beam direction. From equation 2.2 it can be seen that the relative Doppler-shift ΔE/E$_0$ is directly proportional to the recoil velocity $\vec{v}$ and so in the γ-ray spectrum the fully Doppler-shifted γ rays are separated from those

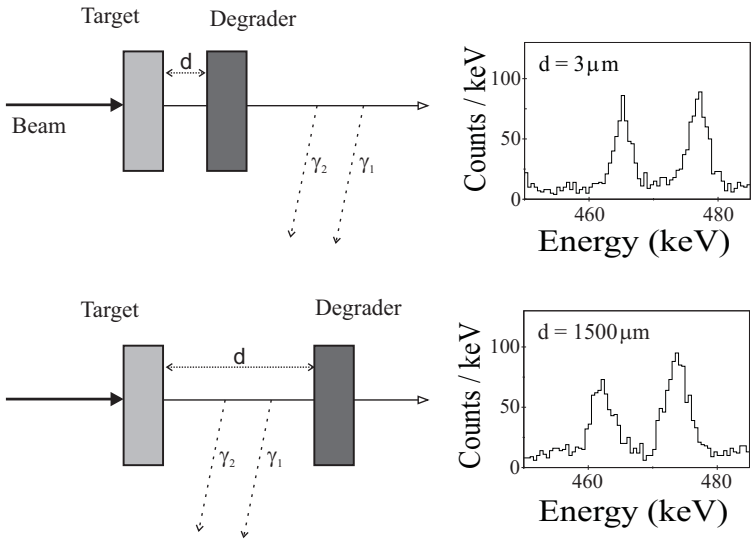

Figure 2.10: A schematic illustrating the principle of the RDDS method: γ rays emitted from a nucleus moving with an initial recoil velocity experience a different Doppler-shift and therefore are detected with a different energy than the γ rays emitted from a nucleus moving with a degraded velocity, having passed through the degrader foil.

emitted by nuclei stopped in the stopper foil, illustrated in figure 2.10. In the present work it was assumed that the direction of $\vec{v}$ was parallel to the beam (hereafter v).

The intensity of the Doppler-shifted component of the γ ray of interest is given by

$$I_s = I\left[1 - e^{\frac{-d}{v\tau}}\right] \tag{2.3}$$

where I is the total number of emitted γ rays of interest. The intensity of the corresponding unshifted γ rays is given by

$$I_u = Ie^{\frac{-d}{v\tau}}. \tag{2.4}$$

The mean lifetime τ can be extracted from a measurement of I_s and I_u, or the ratio $I_u/(I_s + I_u)$, as a function of the distance d if the recoil velocity v is known. The distance d can be varied by either moving the target or the stopper in the plunger device dedicated to the RDDS measurements. The recoil velocity v can be

determined directly by measuring the Doppler-shift as a function of detector angle using equation 2.2.

For the study of exotic nuclei such as ^{175}Au and ^{175,174}Pt via fusion evaporation reactions, the prompt γ-ray spectrum is dominated by huge background as described previously in sections 2.1 and 2.6, and conventional RDDS measurements are not feasible. Tagging techniques described in section 2.6 are required to select the γ rays originating from the nuclei of interest, requiring the nuclei to pass through a recoil separator and reach an implantation detector. This makes the use of a stopper foil as is used in the conventional plunger device impossible. In the present work the stopper foil is replaced by a degrader foil, which allows the recoiling nuclei to continue through to the recoil separator. As a result the stopped component of a γ-ray transition is replaced by a degraded component and the separation ΔE between that and the fully-shifted component is less pronounced than in the case with a stopper foil. The material of the degrader foil is chosen so that the energy loss of the recoiling nucleus is significant.

2.8 The Plunger device

The Köln plunger device was installed at the JUROGAM target position, where the target and degrader foil set-up was housed within a bespoke chamber. The target and degrader foils were glued to aluminium rings and then stretched on conical support frames. The stretching of the foils is required to allow the foils to remain parallel even at allow for distances of a few micrometres. The target was moved using a linear motor (inchworm), with the degrader foil position remaining fixed. For short distances d $\leq$ 200 μm, the target-to-degrader distance was measured by a magnetic transducer. For larger distances an optical system attached to the inchworm was used.

The plunger device was connected to the gate valve at the entrance of RITU replacing the standard JUROGAM target chamber. The target and degrader set-up

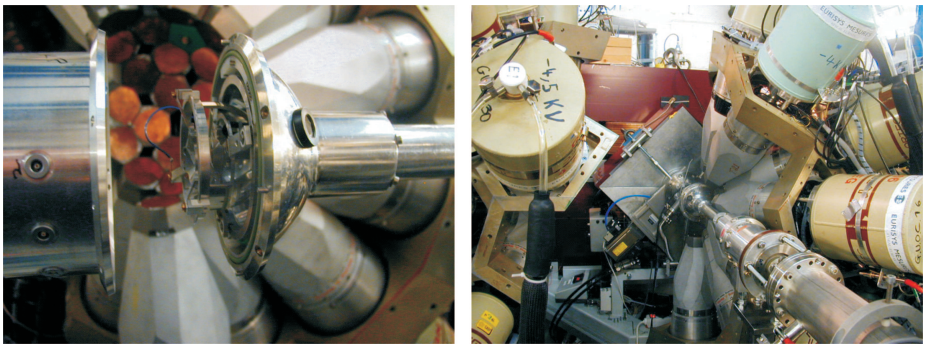

Figure 2.11: Photographs of the Köln plunger device installed into the JUROGAM target position.

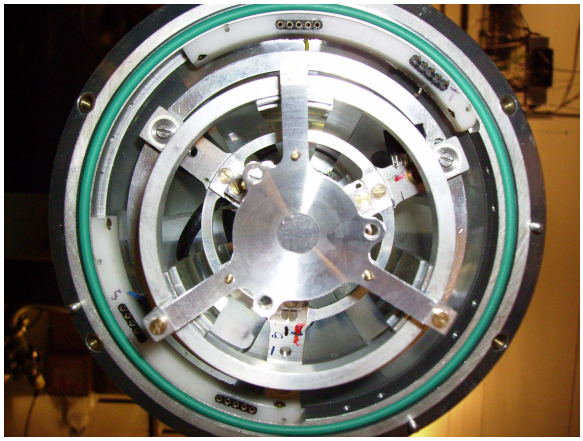

Figure 2.12: Photograph of the Mg degrader foil used in the experiment.

was positioned at the centre of the JUROGAM array. A separate control system for the plunger device recorded the distances of each experimental run. For the shorter distances an automatic regulation of the distance based on the measurement of the capacitance between the target and degrader foils was used. A piezo-crystal is connected to the target frame and the motor. A voltage is generated and applied to the piezo-electric crystal to counter any displacements that occur. This is required to compensate for the small variations in target-to-degrader foil distance that can occur due to the heating of the system by the beam.

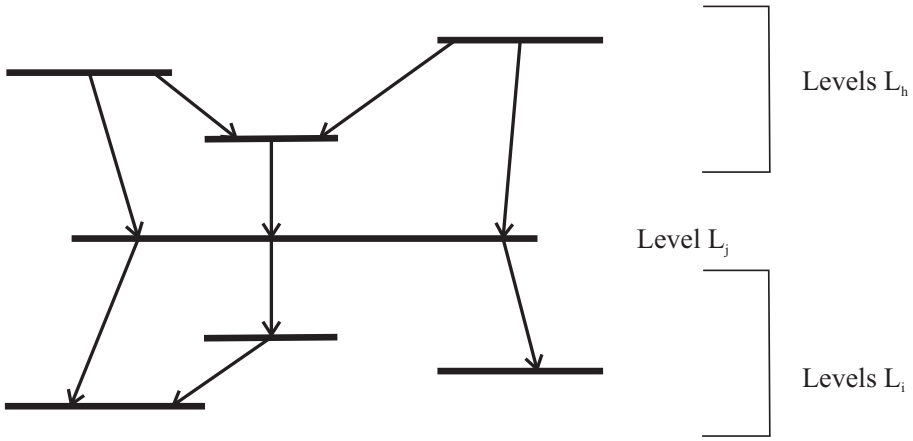

Figure 2.13: A schematic of a decay scheme illustrating the notation used to explain DDCM.

2.9 The differential decay curve method

In this work the lifetimes of the excited states of ^{174,175}Pt and ^{175}Au are derived using the Differential Decay Curve Method (DDCM) [Dewa89, Petk92]. In DDCM, the lifetime of a level can be obtained directly from the Doppler shift measurements. The schematic decay scheme shown in figure 2.13 illustrates the notation used to explain the DDCM.

In the DDCM, the mean lifetime is determined at each target-to-degrader distance d independently, using the equation

$$\tau_i(d) = -\frac{R_{ij}(d) - b_{ij}\sum_h R_{hi}(d)}{v\frac{dR_{ij}(d)}{dt}}, \tag{2.5}$$

where $R_{ij}(d)$ is the intensity of the degraded component of the γ-ray transition from a level i to a level j, $R_{hi}(d)$ is the same for the direct feeding transition from a level h to a level i and b_{ij} is the branching ratio of the transition $i \rightarrow j$. The quantities $R_{ij}(d)$ describe the mean time evolution of the number of nuclei in a certain nuclear level and are linked to the decay constants $\lambda_i = 1/\tau_i$ by the formula

$$R_{ij}(d) = b_{ij}\lambda_i \int_t^\infty n_i(t)dt, \tag{2.6}$$

where $n_i(t)$ is the number of nuclei at the given state i and $d = v$t. The derivative $dR_{ij}(d)/dt$ in the denominator of equation 2.5 must be determined from the measured decay curve by a fitting procedure that fits smoothly connected polynomials through the experimental points without any assumptions. In this way, a smooth differentiable function is created and the values for the derivatives can be obtained.

In the RDDS measurement, spectra are obtained at different target-to-degrader distances from which the areas of the Doppler shifted $\mathrm{I}_{ij}{}^{s}$(d) and degraded I_{ij}^{d}(d) components of the γ-ray peaks corresponding to the transitions $\mathrm{L}_i \rightarrow \mathrm{L}_j$ can directly be measured. In the analysis of the RDDS data it has become standard to introduce the relative quantity $Q_{ij}(d)$ which is proportional to $R_{ij}(d)$ and can be easily calculated from directly measurable quantities according to the relation

$$Q_{ij}(d) = \frac{R_{ij}(d)}{R_{ij}(0)} = \frac{I_{ij}^{d}(d)}{I_{ij}^{s}(d) + I_{ij}^{d}(d)}. \tag{2.7}$$

Equation 2.5 can then be written as

$$\tau_i(d) = -\frac{Q_{ij}(d) - b_{ij} \sum_h \left[J_{hi}/J_{ih}\right] Q_{hi}(d)}{v \frac{dQ_{ij}(d)}{dt}}, \tag{2.8}$$

where J_{hi} and J_{ij} are the relative intensities of the γ-ray transitions $\mathrm{L}_h \rightarrow \mathrm{L}_i$ and $\mathrm{L}_i \rightarrow \mathrm{L}_j$, respectively.

According to equation 2.5, the mean lifetime of a level L_i can be calculated from the ratio of the quantities dR_{ij}(d)/dt and R_{ij}(d)-$b_{ij} \sum_i R_{hi}$(d). These two quantities reach a maximum at a certain distance and so one can introduce the concept of a region of sensitivity, i.e. the region where the mean lifetime can be determined with small errors. The region of sensitivity is illustrated in figure 2.14 and the principle of lifetime determination according to the DDCM is shown in figure 2.15. The main advantage of the DDCM is that the resulting τ(d) values should lie on a horizontal line since the lifetime is constant. Any deviation from the straight line indicates the presence of systematic errors i.e. the overestimation or non-consideration of feeders. A detailed presentation of DDCM can be found in Reference [Dewa89].

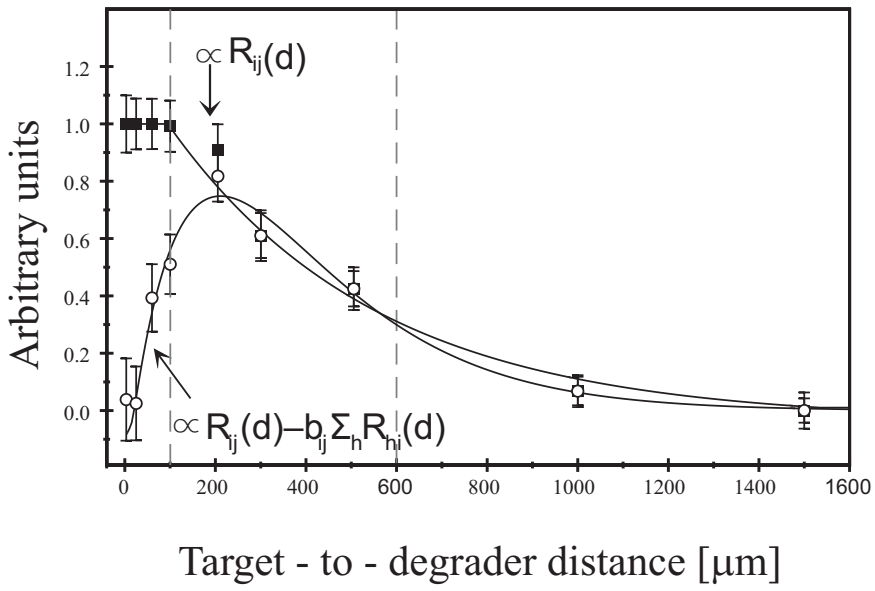

Figure 2.14: A graph of the intensity of the depopulating transition and the intensity difference between the feeding and depopulating transitions. The measured quantities are proportional to the quantities in equation 2.5. The region between the dashed lines indicates the region of sensitivity.

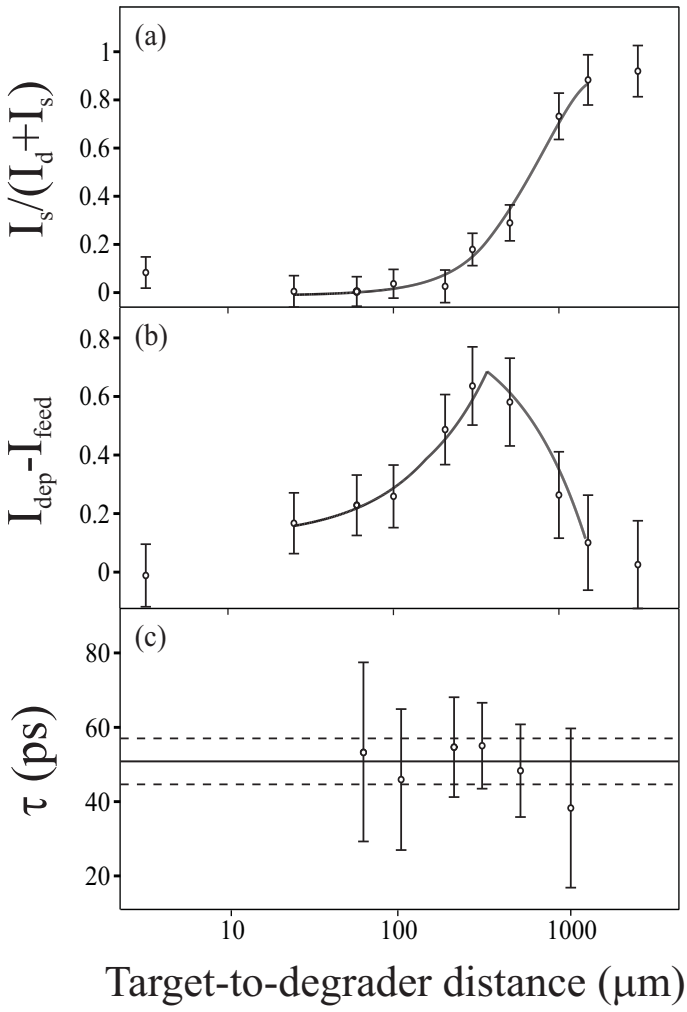

Figure 2.15: A graph illustrating the principles of the DDCM. Panel (a) shows the decay curve $I^d_{ij}(d)/[I^s_{ij}(d)+I^d_{ij}(d)]$ of the $17/2^+$ state in ^{175}Au. Panel (b) shows the intensity difference of the direct feeding and depopulating transition and the solid line is the derivative of the decay curve shown in the upper panel, these quantities are the numerator and denominator given in equation 2.8. Panel (c) shows the lifetime τ as a weighted mean of values $\tau(d)$.

2.9.1 Unobserved side feeding

In a RDDS measurement the time behaviour of the depopulating γ-ray transition is represented by the decreasing intensity of the degraded component with increasing target-to-degrader distance. In considering only the depopulating transition from a level, the determined lifetime is only an effective lifetime of the level. That is, the result not only includes the lifetime of the level but also the complete time behaviour of the feeding transitions. If the feeding history consists of a complex feeding pattern the number of free parameters becomes large and therefore limits the reliability of the fit. For singles RDDS data, in the DDCM only the direct feeding γ-ray transition to a level has to be taken into account, as it is impossible to detect all possible feeding transitions to the level, such as feeding from unobserved discrete levels, which are too weak to detect. Therefore assumptions concerning unobserved feeding have to be made.

The intensities of the unobserved feeding J_i^f can be obtained from the difference of the relative intensities $\sum_h \mathrm{J}_{hi}$ and $\sum_j \mathrm{J}_{ij}$ of the populating and depopulating γ-ray transition, respectively

$$J^f = \sum_j J_{ij}(1+\alpha_{ij}) - \sum_h J_{hi}(1+\alpha_{hi}) = J_{depop} - J_{feed}, \tag{2.9}$$

where α_{ij} is the internal conversion coefficient of the transition $\mathrm{L}_i \rightarrow \mathrm{L}_j$. If the lifetimes of the unobserved feeding transitions are not short compared to the lifetime τ_i and the intensity J^f is not small compared to the intensity J_{depop} considerations of these factors have to be made in the DDCM analysis and equation 2.9 has to be modified. A common hypothesis is that the time dependence of the unobserved feeding is equal to the average lifetime of the direct observed feeders populating the level of interest [Hari87]. This assumption can be introduced in the equations 2.5 and 2.9 by multiplying the contribution of the feeders in the numerator by the quantity $\mathrm{J}_{depop}/\mathrm{J}_{feed}$. This method has been found to be realistic [Petk92] when there are no special structural effects dominating the feeding pattern of the level of interest. The validity of such an assumption can be checked by inspecting the graph τ(d).

Deviations from the horizontal line will indicate the presence of components with different lifetimes. In this way, DDCM will provide more confidence concerning the assumptions made on the unobserved feeding even in extreme cases where only one feeder is known or the feeding lifetime is particularly long. The detailed discussion about the problem of unobserved feeding can be found in references [Dewa89, Petk92, Hari87]. The problems arising due to the unknown lifetime of the unobserved feeding can be solved by a coincidence plunger measurement by gating above the level of interest.

2.10 Summary of experimental details

The experiments discussed in this thesis were performed at the Accelerator Laboratory of the University of Jyväskylä employing the RDT method in the RDDS lifetime measurements of ^{174}Pt and ^{175}Au and the recoil gating technique for the RDDS measurement of ^{175}Pt. Excited states of ^{174,175}Pt and ^{175}Au were populated via the fusion-evaporation reactions using the ^{86}Sr beam delivered by the JYFL K130 cyclotron at an energy of $E_{Beam} = 401$ MeV and a 1 mgcm^{-2} thick ^{92}Mo target, resulting in an initial recoil velocity of $v/c = 4.4$ %. For the degrader foil, 1 mgcm^{-2} thick ^{nat}Mg was used. Prompt γ rays were detected using the JUROGAM Ge-detector array. The beam intensity was limited to 2.5 pnA by the heating of the stretched foils. Due to their suitable angular position for RDDS measurements, only 15 JUROGAM Ge detectors could be used in this experiment; five at an angle of 157.6° and ten at an angle of 133.6° with respect to the beam direction. The standard JUROGAM target chamber was replaced by the Köln plunger device which housed the target and degrader set-up. The replacement of a standard stopper foil of the plunger device by a degrader foil allowed fusion-evaporation residues to recoil into RITU.

On production, the recoils pass through the degrader foil to RITU, which separates the recoils from the un-reacted beam. The recoils are transported to the GREAT focal plane spectrometer where they are detected. At the entrance of GREAT, the MWPC

records the energy loss and timing signals generated by the recoils in flight. Following the MWPC the recoils are implanted into the DSSDs which record the position of the recoiling nucleus and its subsequent decay properties. Signals from all detectors were collected and time stamped independently with 10 ns accuracy by employing the TDR data acquisition system. Analysis of the data was performed using the GRAIN software package. The RDT method described in section 2.6 is implemented to construct singles RDT γ-ray spectra.

The RDT singles and recoil-gated γ-ray spectra from the two JUROGAM Ge-detector rings were analysed separately. For each target-to-degrader distance normalisation was obtained by normalising the intensities of the fully shifted (or degraded) components of the γ-ray transition under investigation to the sum of the areas of the two components. These quantities (the functions $Q_{ij}(d)$) are representative of the time behaviour of the corresponding transition as indicated in equation 2.7.

The fitting of the γ-ray peaks was performed by fixing the centroids and widths of both the degraded and fully-shifted components. These two parameters were obtained using the γ-ray spectra of the experimental runs with the shortest (degraded component) and longest (full-shifted component) target-to-degrader distances. At the extreme distances primarily only one of the components is observed. Once the two parameters of both components of the γ-ray transition of interest are fixed, the peak areas for the two components can be measured for each target-to-degrader distance.

Decay curves of quantities $Q_{ij}(d)$ were constructed and analysed by means of DDCM. The resulting lifetime of each level is an average of the lifetimes extracted from the decay curves measured with JUROGAM Ge-detectors at 157.6° and 133.6°.

Chapter 3

Deformation and collectivity of the coexisting shapes in ^{174}Pt and ^{175}Pt

The lifetimes of the excited states in the neutron-deficient nuclei ^{174}Pt and ^{175}Pt have been studied using the recoil distance Doppler-shift method and utilising tagging techniques in an experiment performed at the Accelerator Laboratory of the University of Jyväskylä. In measuring the lifetime of the excited states, the absolute transition probabilities can be determined and provide a direct measure of the quadrupole collectivity. In this chapter the results of the experimentally determined lifetimes of the excited states in ^{174}Pt and ^{175}Pt are discussed and compared to lifetime measurements of other neutron-deficient even-mass Pt nuclei.

3.1 Shape coexistence in ^{174,175}Pt

The nuclear phenomenon of shape coexistence occurs when nuclear configurations based on different deformations lie at similar excitation energies. This phenomenon occurs in nuclei near closed shells and has been interpreted in terms of intruder configurations based on particle-hole excitations producing deformed configurations [Wood92, Heyd83]. In the case of neutron-deficient Pb nuclei ($Z = 82$) and nuclei below the $Z = 82$ closed shell, such as Tl-Hg-Au-Pt [Lane94, Juli01, Kond01,

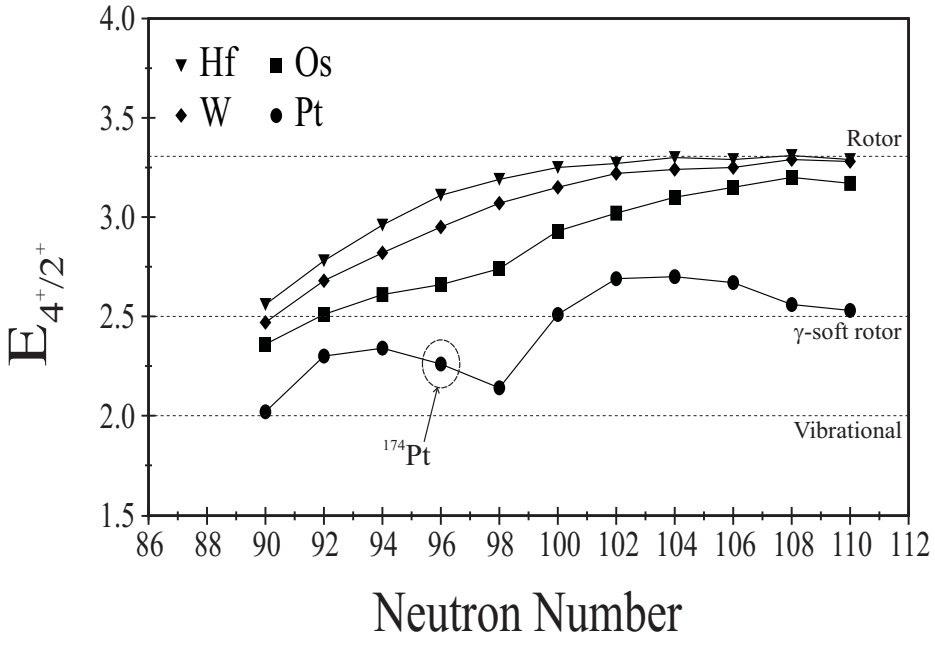

Figure 3.1: Yrast $E_{4^+/2^+}$ ratio in the even-Z $_{72}$Hf, $_{74}$W, $_{76}$Os and $_{78}$Pt.

Drac86] shape coexistence occurs when proton pairs are excited into the $h_{9/2}$, $f_{7/2}$ and $i_{13/2}$ intruder orbitals [Wood92, Heyd83, Naza93].

For the Pt isotopes at $N \simeq 96$ the nuclei may already be well deformed in the ground state resulting in a decrease in the difference in deformation between the competing minima and the height of the potential barrier between them. Theoretical calculations of the shape coexistence observed in even-even $^{174-180}$Pt suggest that the prolate minimum is due to the excitation of two (or more) protons across the $Z = 82$ gap into deformation driving orbitals [Drac91].

Figure 3.1 shows the systematic trend of the $E_{4^+/2^+}$ ratio for the $_{72}$Hf to $_{78}$Pt nuclei as a function of neutron number. The plot shows the gradual decrease of $E_{4^+/2^+}$ from the rotational limit as the $N = 82$ shell closure is approached. The Os ($Z = 76$) and Pt ($Z = 78$) nuclei show a deviation from this smooth behaviour at $N \simeq 98$. This is the result of the coexistence of different shaped minima at low spin. In the light Pt nuclei, unlike the behaviour observed in Pb and Hg where the different shapes are observed in distinct band structures, the phenomena of shape coexistence

manifests itself as a mixed band observed as a deviation from the regular I(I+1) rotational structure at low spin. The irregular level spacing observed at low spin in the yrast band of ^{176}Pt was interpreted [Cede90] in terms of competition between triaxial and prolate shapes relating to the occupation of different proton orbitals in the ground state band. This behaviour was found to be more pronounced in ^{174}Pt. This irregular behaviour at low spin was also observed in the assigned $\nu i_{13/2}$ signature partner bands of ^{175}Pt [Cede90]. It was also noted that the $N = 98$ gap stays almost constant when the ^{175}Pt nucleus undergoes the predicted shape changes, implying the neutron configuration is not affected by the deformation changes. Therefore the low spin irregularity observed in ^{175}Pt was explained to be analogous to the crossing of different proton structures as discussed for the even-A Pt nuclei [Cede90].

Experimentally, the degree of collectivity of low-lying excited states in nuclei can be determined by measuring the lifetime of the level. In doing so the absolute transition probabilities can be determined and provide a direct measure of the collectivity. In the present study, Recoil Distance Doppler Shift (RDDS) [Schw68] lifetime measurements have been carried out for the first time in ^{174}Pt and an odd-A Pt nucleus ^{175}Pt. The lifetimes of the low-lying yrast states in ^{175}Pt and the 6^+ state in ^{174}Pt have been measured. For ^{175}Pt the measured $|Q_t|$ values are in agreement with the interpretation of a transition from a collective, possible triaxial structure to a collective, prolate deformed band. The 6^+ state in ^{174}Pt is also a member of the collective, prolate band.

3.2 Results - the nucleus ^{174}Pt

3.2.1 Experimental details

The α-decay properties of ^{174}Pt were measured using the DSSD of the GREAT spectrometer and are presented in figure 3.2. The measurements are in agreement with the error weighted averages determined from published results: $E_\alpha = 6039(3)$ keV and $t_{1/2} = 889(8)$ ms [Della81, Enge82, Page96].

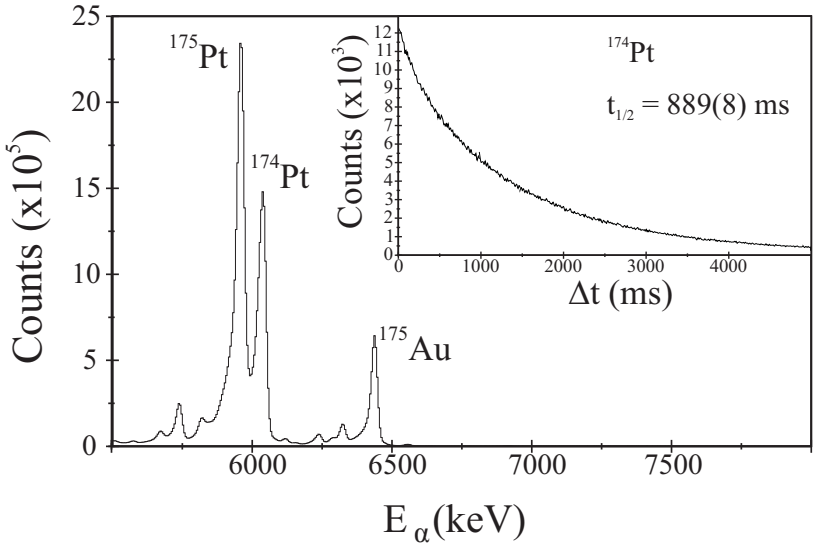

Figure 3.2: Energy spectrum of all the α decays occurring within 2.7 s of a recoil implantation into the same DSSD pixel. The α decay peak of ^{174}Pt is shown. The decay curve is shown in the inset.

E_γ [keV]	J_γ	ΔE at 158° [keV]	ΔE at 134°	I_i^π	J_{feed}/J_{depop}
474	68(4)	3.5	4.8	6^+	0.73(7)

Table 3.1: Energy separation ΔE of the fully Doppler-shifted and degraded components of the depopulating γ-ray transition of the 6^+ state in ^{174}Pt as well as the relative intensity J_γ and intensity balance J_{feed}/J_{depop}. The intensities are relative to the 394 keV $2^+ \rightarrow 0^+$ transition.

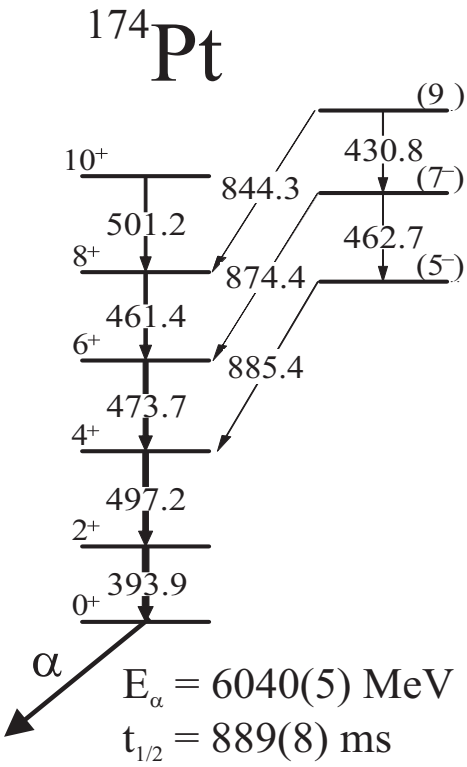

Figure 3.3: Partial level scheme of ^{174}Pt showing the yrast band as well as the side-band and feeding transitions according to Ref. [Goon04].

The yrast states of ^{174}Pt were populated using the ^{92}Mo(^{86}Sr,2p2n)^{174}Pt* fusion evaporation reaction with a beam energy of 401 MeV. A 1 mg/cm^2 Mg degrader foil was used in the plunger device, obtaining a velocity difference of $\Delta v/c = 1.1$ %; $v/c = 4.4$ % before and 3.3 % after the degrader foil. Singles RDT γ-ray spectra were constructed for ten target-to-degrader distances ranging from 3 μm to 3000 μm, details of which are presented in table 3.2. As described in section 2.10 it is imperative the stretched target and degrader foils are not heated to the point that the distance between them deviates as this introduces systematic errors in the distance measurement. For this reason, and also the counting rate limit of the signal processing electronics of the Ge detectors, the beam current was limited to an average of 2 pnA. Details of the energy differences of the fully Doppler-shifted and degraded components of the γ-ray transitions measured are given in table 3.1.

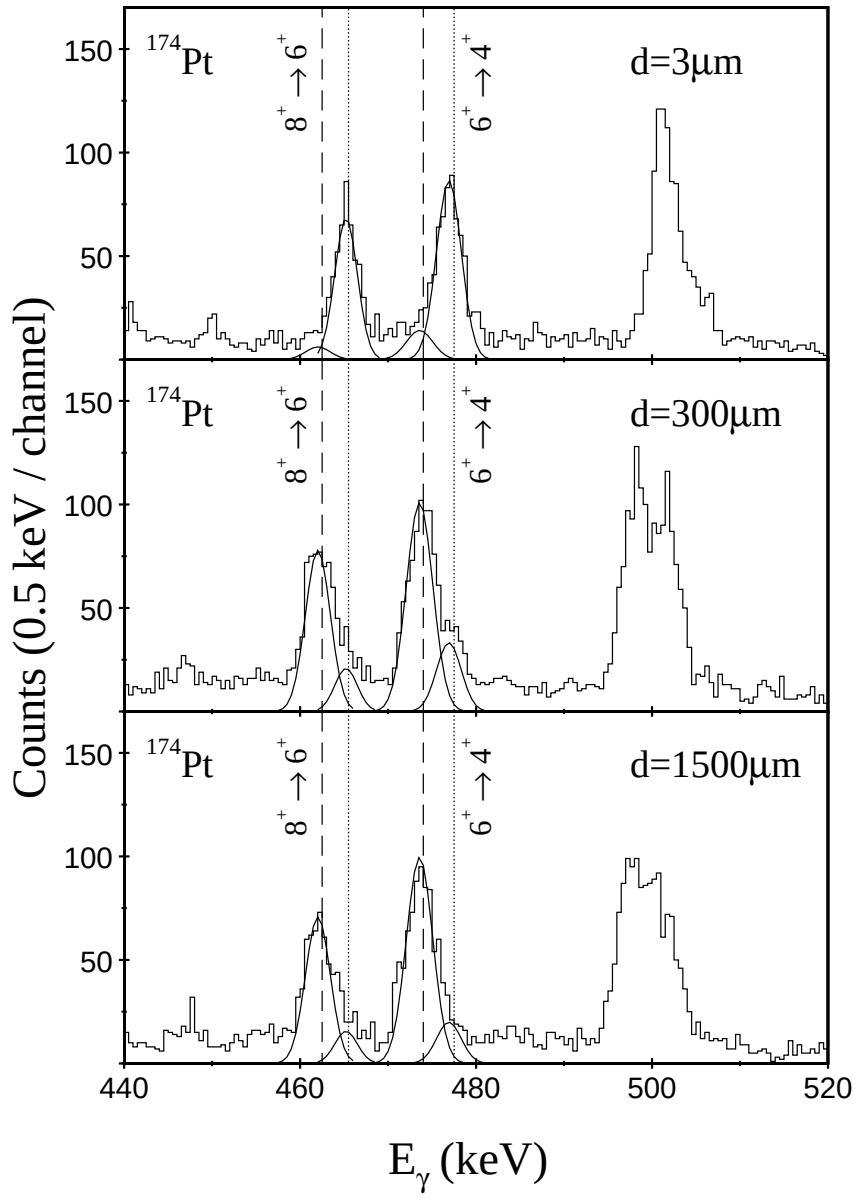

Figure 3.4: Spectra showing γ rays correlated with the recoils implanted in the focal plane DSSDs and followed by a distinct ^{174}Pt α decay with the same pixel. The correlation time was limited to 2.7 s. The spectra are measured at three target-to-degrader distances: (a) 3 μm, (b) 100 μm and (c) 1000 μm, with ten JUROGAM detectors at 134°. The dashed (dotted) lines indicate the positions of the fully Doppler-shifted (degraded) components of the transitions under study. The highest energy, unresolved peak is a combination of the fully Doppler-shifted and degraded components of the 497 keV and 501 keV γ-rays.

Distance d (μm)	Counts I_s + I_d
3.2(17)	1044
25.0(1)	1039
60.0(5)	1131
100.1(5)	1092
205.3(24)	1014
300.4(20)	1370
505.4(88)	1001
1000(20)	1336
1500(30)	1136
3000(60)	1245

Table 3.2: Summary of the peak areas measured for the $2^+ \rightarrow 0^+$ transition with 10 JUROGAM detectors at 134° at the 10 different target-to-degrader foil distances used.

The α decays of ^{174}Pt were correlated with the recoils to construct the singles RDT γ-ray spectra. A partial level scheme of ^{174}Pt is presented in figure 3.3, which shows the yrast band, the side band and the feeding transitions [Goon04]. Examples of the singles γ-ray spectra are shown in figure 3.4.

3.2.2 Lifetime measurements of the 6^+ state

For the lifetime measurement of ^{174}Pt only 5 detectors (at an angle of 158° with respect to the beam direction) and 10 detectors (134°) of the JUROGAM Ge detectors were used. The fitted peaks were normalised to the summed intensities of the degraded (I_d) and fully shifted (I_s) components (see equation 2.7). The quantity $Q_{ij}(d) = I^d_{ij}(d)/[I^s_{ij}(d)+I^d_{ij}(d)]$ for the 6^+ state is shown in figure 3.5. In the analysis of singles RDDS data the effect of unobserved feeding transitions must be taken into account. The relative intensities of the feeding and depopulating transitions J_{feed}/J_{depop} were measured from the experimental run with the highest statistics (300 μm run). The

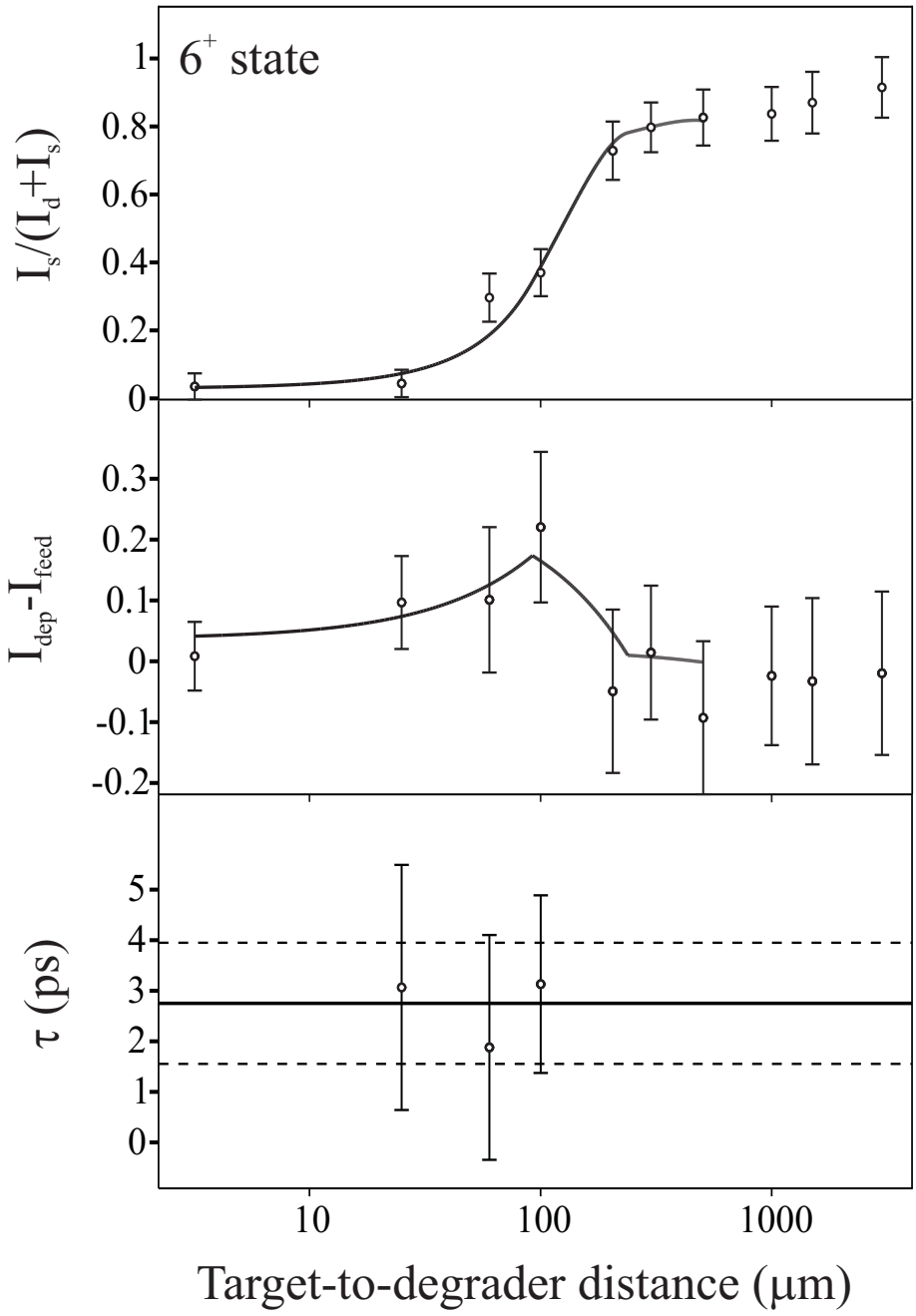

Figure 3.5: Decay curve of the 6^+ state of ^{174}Pt measured with ten JUROGAM detectors at 134°. The upper panel shows the decay curve $I^d_{ij}(d)/[I^s_{ij}(d)+I^d_{ij}(d)]$ of the 6^+ state in ^{174}Pt. The middle panel shows the intensity difference of the direct feeding and depopulating transition and the solid line is the derivative of the decay curve shown in the upper panel, these quantities are the numerator and denominator given in equation 2.8. The lower panel shows the lifetime τ as a weighted mean of values $\tau(d)$.

E_γ	I_i^π	τ	B(E2)	B(E2)	$\lvert Q_t \rvert$	$\lvert \beta_2 \rvert$
		ps	e^2b^2	W.u.	eb	
474	6^+	3(1)	1.11(20)	190(30)	5.9(5)	0.22(2)

Table 3.3: Electromagnetic properties of the low lying yrast states in ^{174}Pt extracted from the lifetime measurement.

result of this calculation for the 6^+ state is given in table 3.1. For the 6^+ it is reasonable to assume the time behaviour of the unobserved feeding to be similar to that for the observed direct feeder as discussed in section 2.9.

The mean lifetime τ value of the 6^+ state is a weighted average of the two values extracted independently from the data recorded with the detectors at 134° and 158°. The lifetime of the 6^+ state is presented in table 3.3 along with the absolute values of the transition quadrupole moment $|Q_t|$ (equation 1.29) and deformation parameter β_2 (equation 1.32), extracted from the experimental reduced transition probability B(E2) (equation 1.28). For ^{174}Pt the 497 keV and 501 keV γ rays ($4^+ \rightarrow 2^+$ and $8^+ \rightarrow 6^+$ respectively) could not be resolved (see figure 3.3 and 3.4) as a result the lifetime of the 2^+ and 4^+ states could not be extracted.

3.3 Results - The nucleus ^{175}Pt

3.3.1 Experimental details

The lifetimes of two low-lying yrast states in ^{175}Pt were measured in a recoil-gated $\gamma\gamma$-coincidence analysis implementing the RDDS method. A partial level scheme of ^{175}Pt is presented in figure 3.6 which shows the assigned $\nu i_{13/2}$ signature partners of the experimentally observed bands [Cede90]. Singles RDT γ-ray spectra were not be used for two reasons, the half-life is long for RDT and the γ-rays in the other band of ^{175}Pt are of similar energies to those observed in the $\nu i_{13/2}$ band therefore coincidence analysis is required to separate the two bands. The yrast states of ^{174}Pt

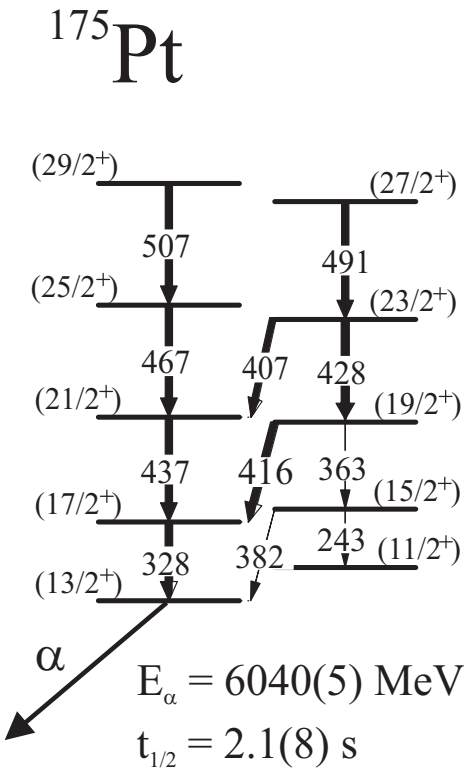

Figure 3.6: Partial level scheme of ^{175}Pt showing the $\nu i_{13/2}$ signature partner bands according to Ref. [Cede90].

were populated using the ^{92}Mo(^{86}Sr,2pn)^{175}Pt* fusion evaporation reaction with the experimental details as those described above. Details of the energy differences of the fully Doppler-shifted and degraded components of the γ-ray transitions measured are given in table 3.4.

3.3.2 Lifetime measurements of the $21/2^+$ and $17/2^+$ states

To exclude the uncertainties originating from the time behaviour of unobserved feeding, the projected spectra are gated with transitions directly feeding levels of interest and projected onto the axes recorded with the JUROGAM detectors at either 134° or 158°. In standard DDCM analysis gates are usually set on the fully Doppler-shifted component of the feeding transition. However, in the present investigation it

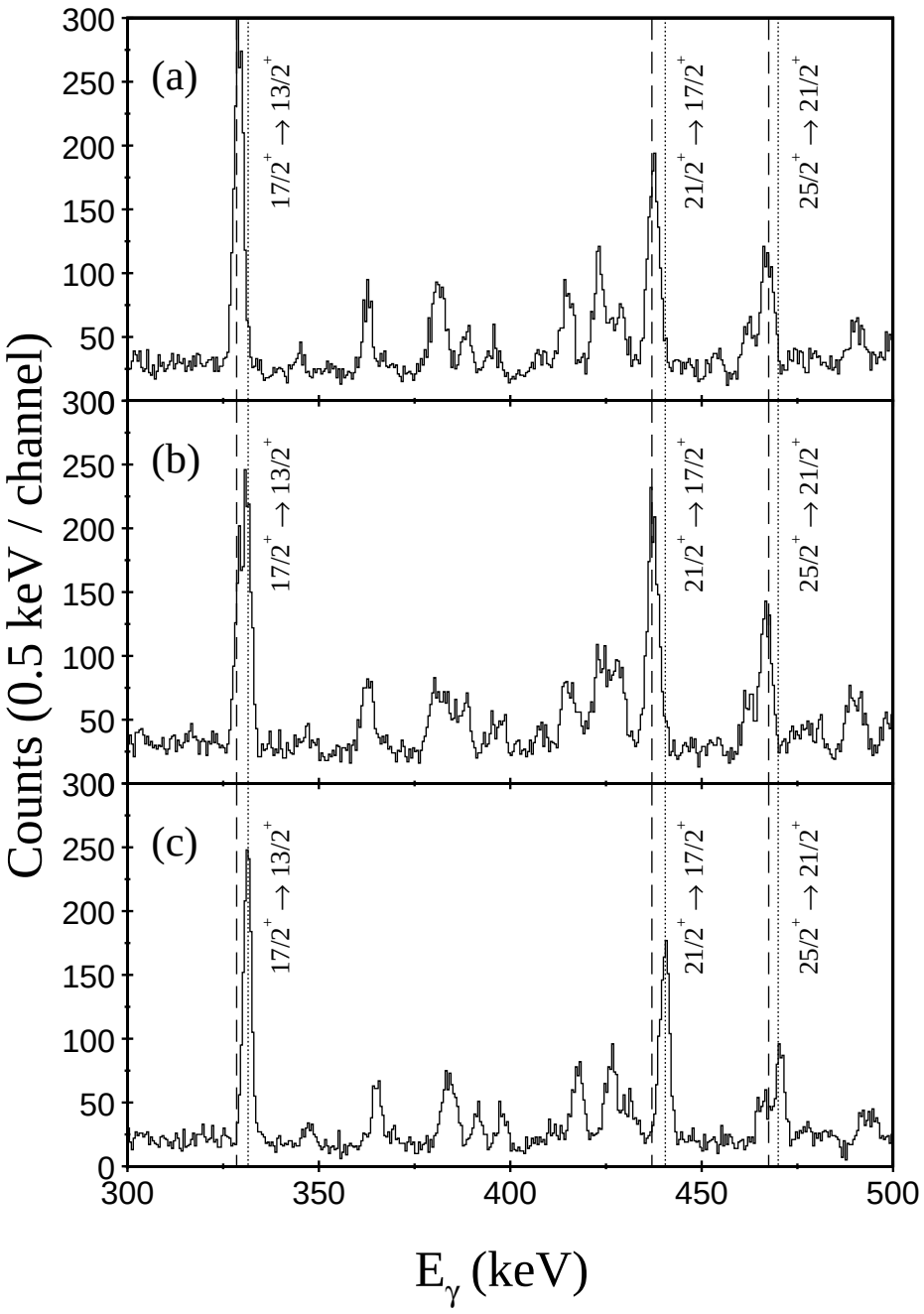

Figure 3.7: Spectra showing γ rays correlated with the recoils implanted in the focal plane DSSDs. The $\gamma\gamma$ coincidence spectra of ^{175}Pt are measured at three target-to-degrader distances: (a) 3000 μm, (b) 300 μm and (c) 3 μm, with ten JUROGAM detectors at 134°. The dashed (dotted) lines indicate the positions of the fully Doppler-shifted (degraded) components of the transitions under study.

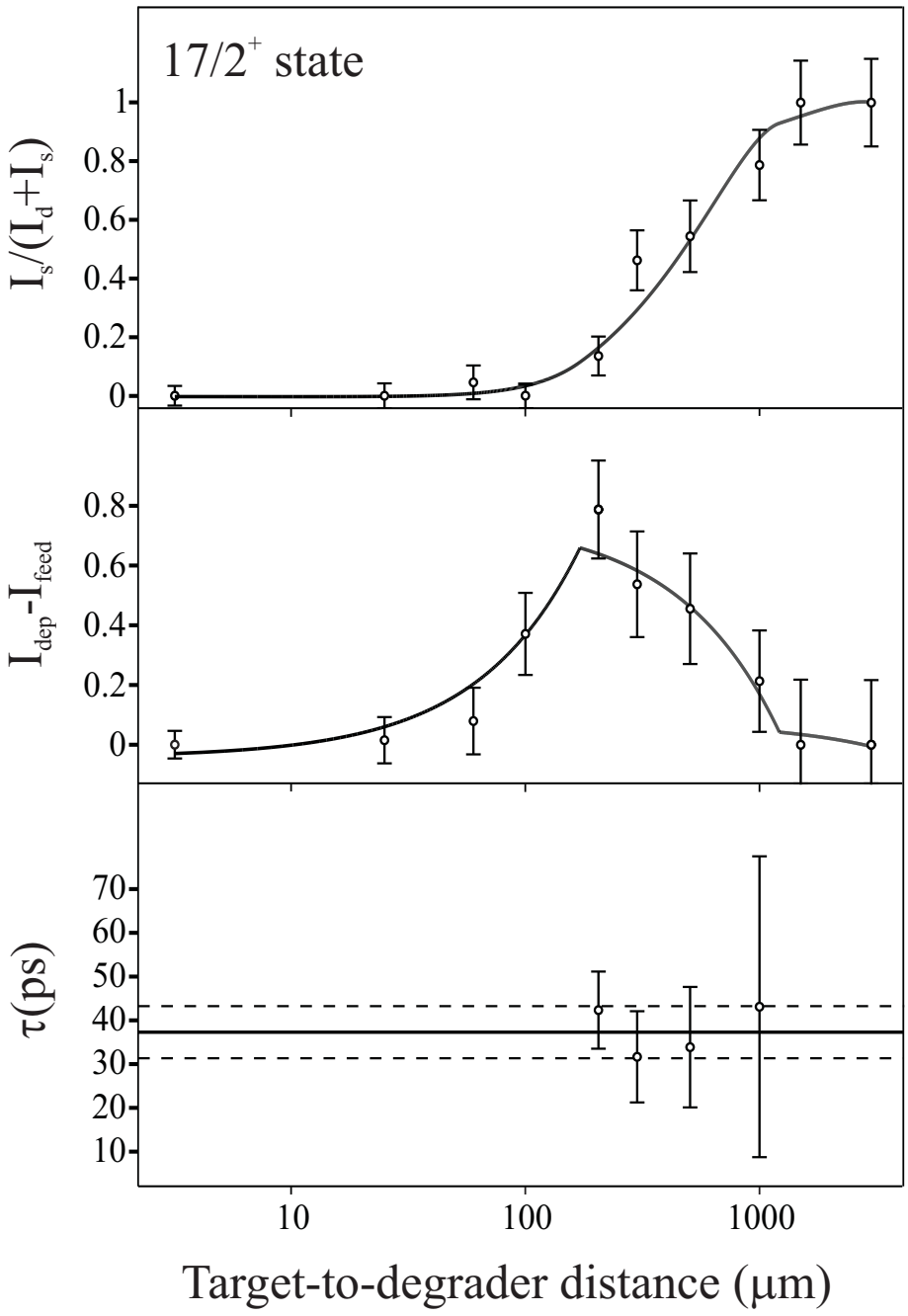

Figure 3.8: Decay curve of the $17/2^+$ state in ^{175}Pt measured with ten JUROGAM detectors at 134°.

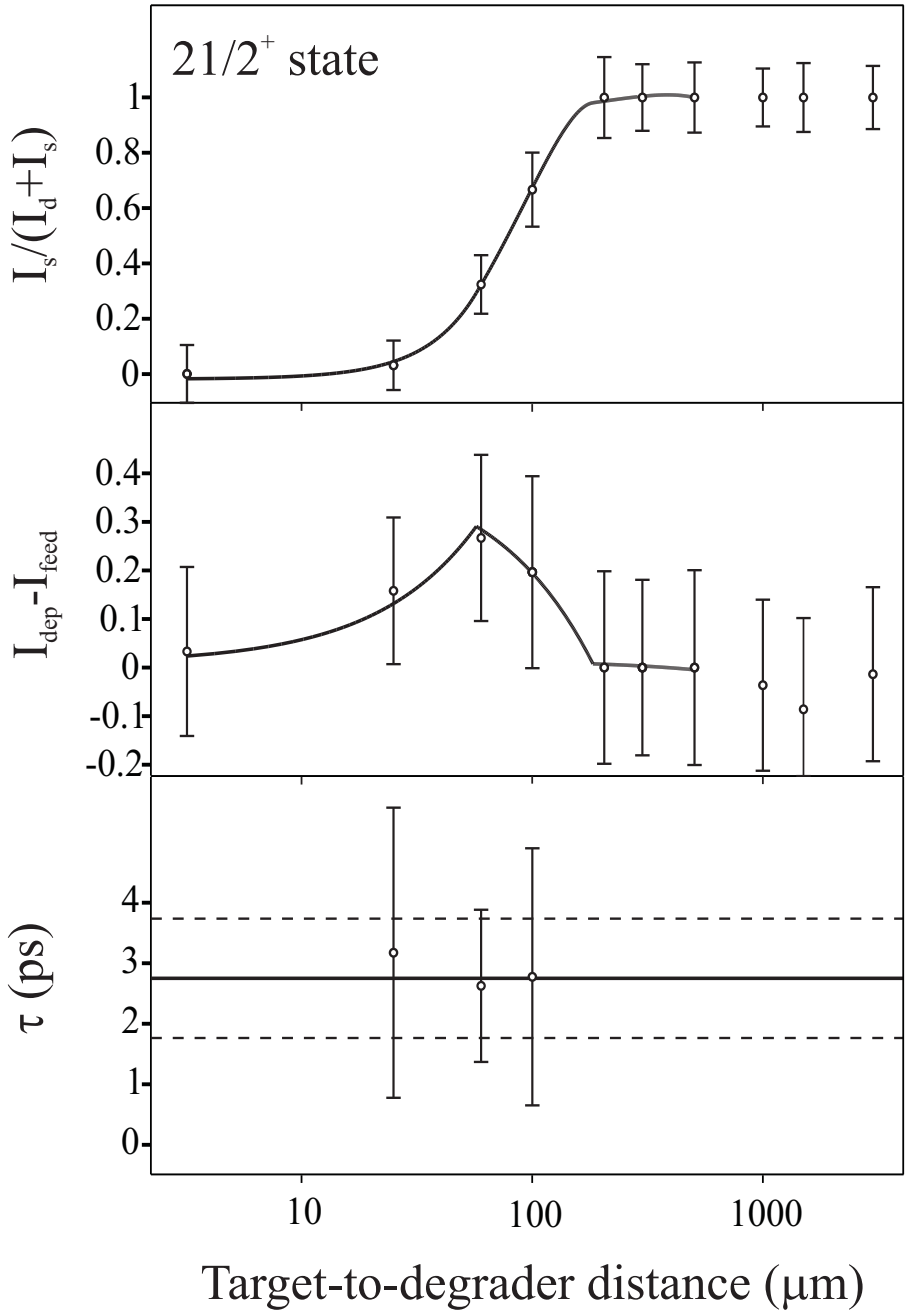

Figure 3.9: Decay curve of the $21/2^+$ state in ^{175}Pt measured with ten JUROGAM detectors at 134°.

E_γ [keV]	I_i^π	ΔE at 158° [keV]	ΔE at 134°
328	$17/2^+$	2.4	3.3
437	$21/2^+$	2.9	4.3

Table 3.4: Energy separation ΔE of the fully Doppler-shifted and degraded components for each level of interest in ^{175}Pt.

E_γ	I_i^π	τ	B(E2)	B(E2)	$\lvert Q_t \rvert$	$\lvert \beta_2 \rvert$
		ps	e^2b^2	W.u.	eb	
328	$17/2^+$	39(2)	0.52(3)	88(5)	4.0(1)	0.15(1)
437	$21/2^+$	3(1)	1.68(28)	290(50)	7.0(6)	0.25(2)

Table 3.5: Electromagnetic properties of the low lying yrast states in ^{175}Pt extracted from the lifetime measurement.

is necessary to gate on the full line shape, corresponding to the degraded and fully shifted component of the detected γ-ray transition recorded with all the JUROGAM Ge detectors to increase statistics of the $\gamma\gamma$-coincidence spectra of ^{175}Pt. Examples of recoil gated $\gamma\gamma$ coincidence spectra are shown in figure 3.7. The normalised decay curves $I_s/(I_s+I_d)$ for depopulating transitions of the $17/2^+$ and $21/2^+$ states were constructed and are shown in figure 3.8 and 3.9. Validation of this method can be found in references [Grah09, Grah10].

The mean lifetime τ values were extracted independently from the data recorded with the detectors at 158° and those at 134° using the DDCM resulting in a lifetime that is a weighted average of these two values. The lifetimes of the $17/2^+$ and $21/2^+$ state are presented in table 3.5 in addition to the absolute values of the transition quadrupole moment $|Q_t|$ and deformation parameter β_2 extracted from the experimental reduced transition probability B(E2).

3.4 Discussion

In this study the collectivity for the low-lying states in ^{174}Pt and ^{175}Pt have been experimentally measured and, in the context of coexisting shapes, interesting conclusions can be made. The large B(E2) reduced transition probability of the $21/2^+ \rightarrow 17/2^+$ transition in ^{175}Pt is indicative of high collectivity for the $21/2^+$ yrast state. The observed decrease in the transition probability of the $17/2^+ \rightarrow 13/2^+$ transition alludes to a shape change at low spin. The large $E2$ transition probability of the $6^+ \rightarrow 4^+$ transition in ^{174}Pt is evidence of the 6^+ state being a member of a collective prolate band.

3.4.1 Previous interpretation

Studies of the yrast bands in even-even Pt nuclei have revealed a variation in shape at low spin. This shape change is the result of two coexisting minima; one prolate and one triaxial, which have similar excitation energies. The prolate minimum is associated with proton excitations into low-Ω $h_{9/2}$ and $f_{7/2}$ intruder bands. The energy of these intruder states exhibits parabolic dependence on neutron number with a minimum near the neutron mid-shell ($N = 104$) becoming it is yrast for $^{178-182}$Pt [Kond00, DeVo90, Pope97]. Below the neutron mid-shell it is the triaxial minimum, which becomes dominant at low spin. This comes about as the number of valence neutron decreases and the prolate minimum begins to increase in energy resulting in the energy difference between the near spherical and prolate minima increasing. Figure 3.10 shows the Single-particle Woods-Saxon levels for protons and neutrons calculated for nuclei in the $A \approx 175$ region. For neutrons a gap is highlighted for $N = 98$ at positive deformation, occupation of the orbitals surrounding this gap stabilise the prolate shape of the nucleus. Decreasing the number of neutrons leads to a region with a number of competing, different deformation driving orbitals the result being triaxially deformed nuclei.

The kinematic moments of inertia of the even-even nuclei $^{172-178}$Pt and the odd-N

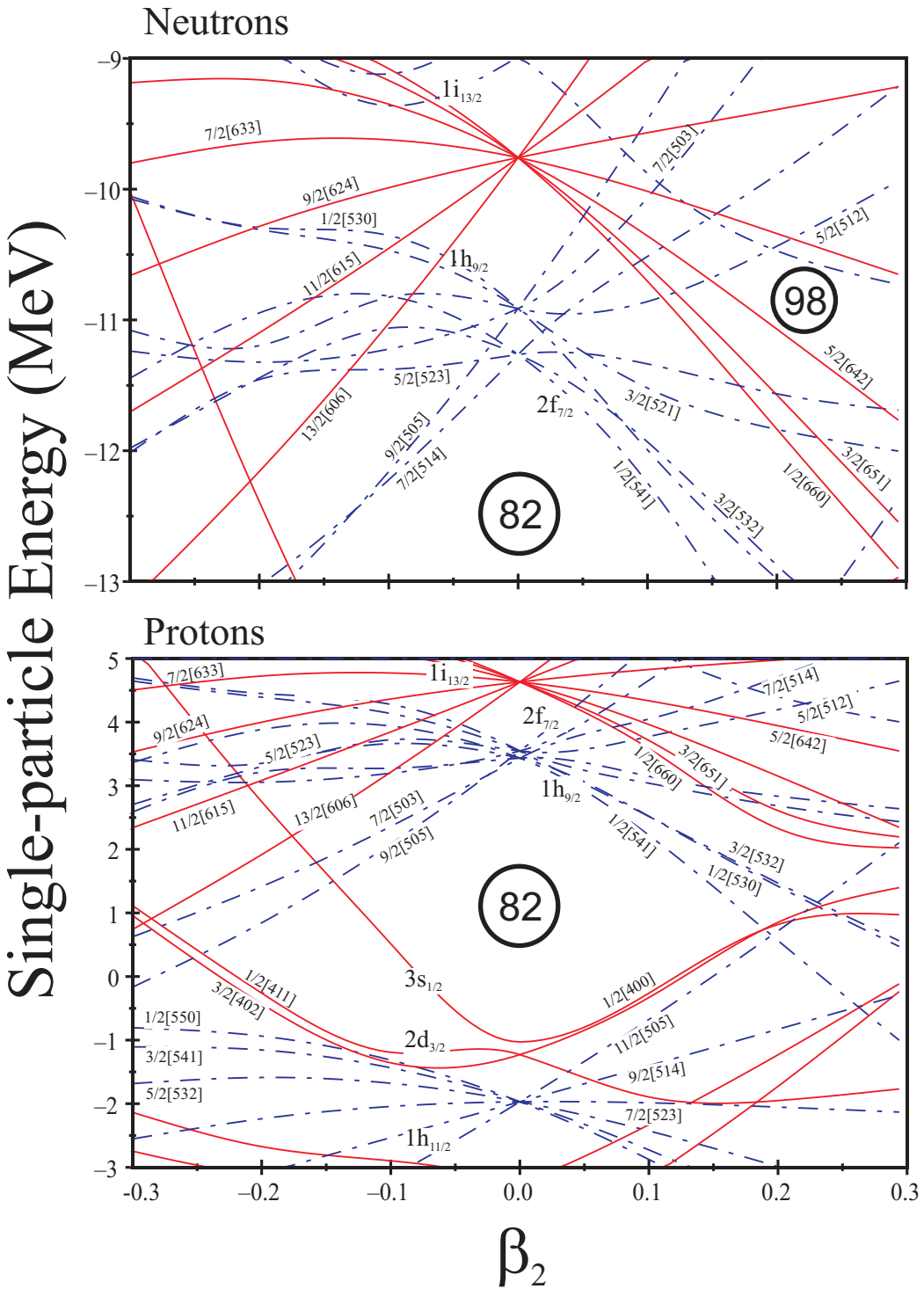

Figure 3.10: Single-particle Woods-Saxon levels for protons and neutrons calculated for nuclei in the $A \approx 175$ region. Dashed and solid lines represent negative and positive parity, respectively.

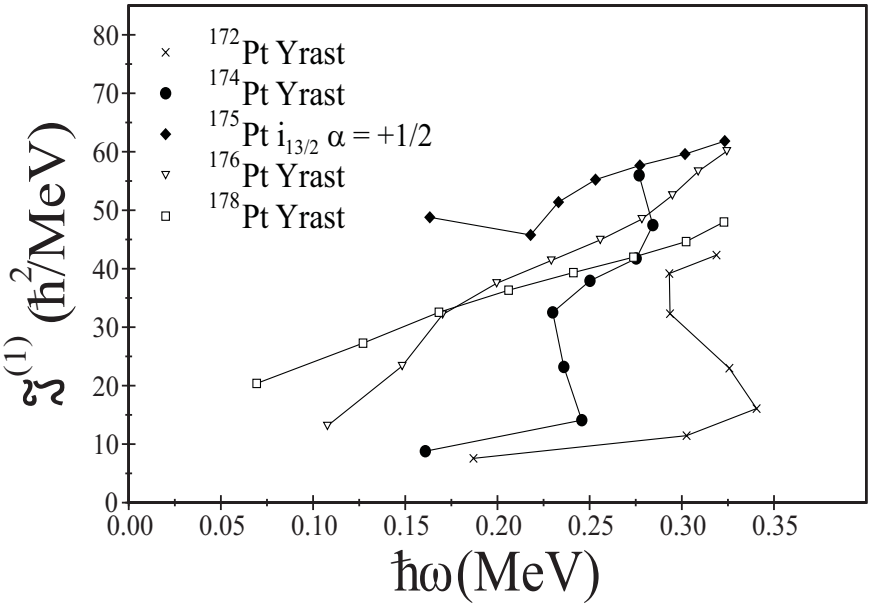

Figure 3.11: Kinematic moment of inertia $\Im^{(1)}$ vs rotational frequency $\hbar\omega$ for the yrast bands of the even nuclei ^{172,178}Pt and the favoured $i_{13/2}$ α=+1/2 signature band of the odd-A ^{175}Pt. The data for ^{172,176,178}Pt are taken from Refs. [Joss06, Cede90, Kond00].

nucleus ^{175}Pt are compared in figure 3.11. A close inspection of figure 3.11 reveals an irregularity in the low-spin yrast level structures of ^{174}Pt and ^{176}Pt. In the framework of a two band mixing model [Drac91] this irregularity has been interpreted as a crossing of a near-spherical ground state sequence by a more deformed configuration.

The two bands observed in the level scheme of ^{175}Pt have been assigned as the neutron $i_{13/2}$ signature partners [Cede90]. This assignment was based on the observation that in all the neighbouring $N = 97$ isotones, these bands are observed to be yrast at low excitation energy and the prediction that the neutron $i_{13/2}$ bands are most favoured due to the strong Coriolis coupling of the single $i_{13/2}$ neutron to the rotational motion [Kond02, Cede90, Bark90]. Cederwall *et al.* [Cede90] concluded that the yrast band in ^{174,176}Pt rapidly switches over from triaxial less beta deformed shape to the higher beta deformation. The deformed prolate shape is favoured relative to the triaxial shape by rotation because of the larger moment of inertia. It was also concluded that the irregularity in the kinematic moment of inertia for the favoured

band in ^{175}Pt is the same as the crossing of different proton structures as discussed for ^{174,176}Pt. It was also highlighted that the $N = 98$ sub-shell closure stays almost constant when the ^{175}Pt nucleus undergoes the predicted shape change, implying that the neutron configuration is not affected by the deformation changes [Cede90].

3.4.2 Total Routhian Surfaces

Total Routhian Surfaces (TRS) [Wyss88, NLD87, NWJ89] based on a Woods-Saxon potential and the Strutinsky shell correction formalism have been constructed for $^{174-176}$Pt and are shown in figure 3.12. The TRS represent the energy of a given configuration in the rotating system, as a function of the deformation parameters, β_2 and γ. For ^{176}Pt, at $\hbar\omega = 0$, a degree of β and γ softness is observed. In the case of ^{174}Pt, the γ-softness is more pronounced with a minimum observed at the deformation parameters $\beta_2 \approx 0.15$, $\gamma \approx$ -25°. Above the neutron crossing, the TRS calculations predict similar deformation parameters in ^{174}Pt as observed in ^{176}Pt. The TRS calculations show that ^{175}Pt exhibits a similar and intermediate behaviour to that observed in ^{174,176}Pt. As in ^{174,176}Pt the minima move towards a more deformed shape with increasing rotational frequency.

3.4.3 Staggering Parameter

Triaxial or γ-soft nuclear shapes can promote large signature splitting in deformation aligned orbitals at low frequencies. The signature splitting of the $i_{13/2}$ band in ^{175}Pt is compared to those in the heavier odd-N isotopes ^{177}Pt and ^{179}Pt in figure 3.13 in terms of the staggering parameter $S(I)$ defined as:

$$S(I) = E(I) - E(I-1) - 1/2[E(I+1) - E(I) + E(I-1) - E(I-2)]. \quad (3.1)$$

The large signature splitting can be interpreted as resulting from triaxial deformation as prolate deformation would result in a small staggering parameter. A shape transition from γ-soft to axially symmetric prolate deformation would bring about a

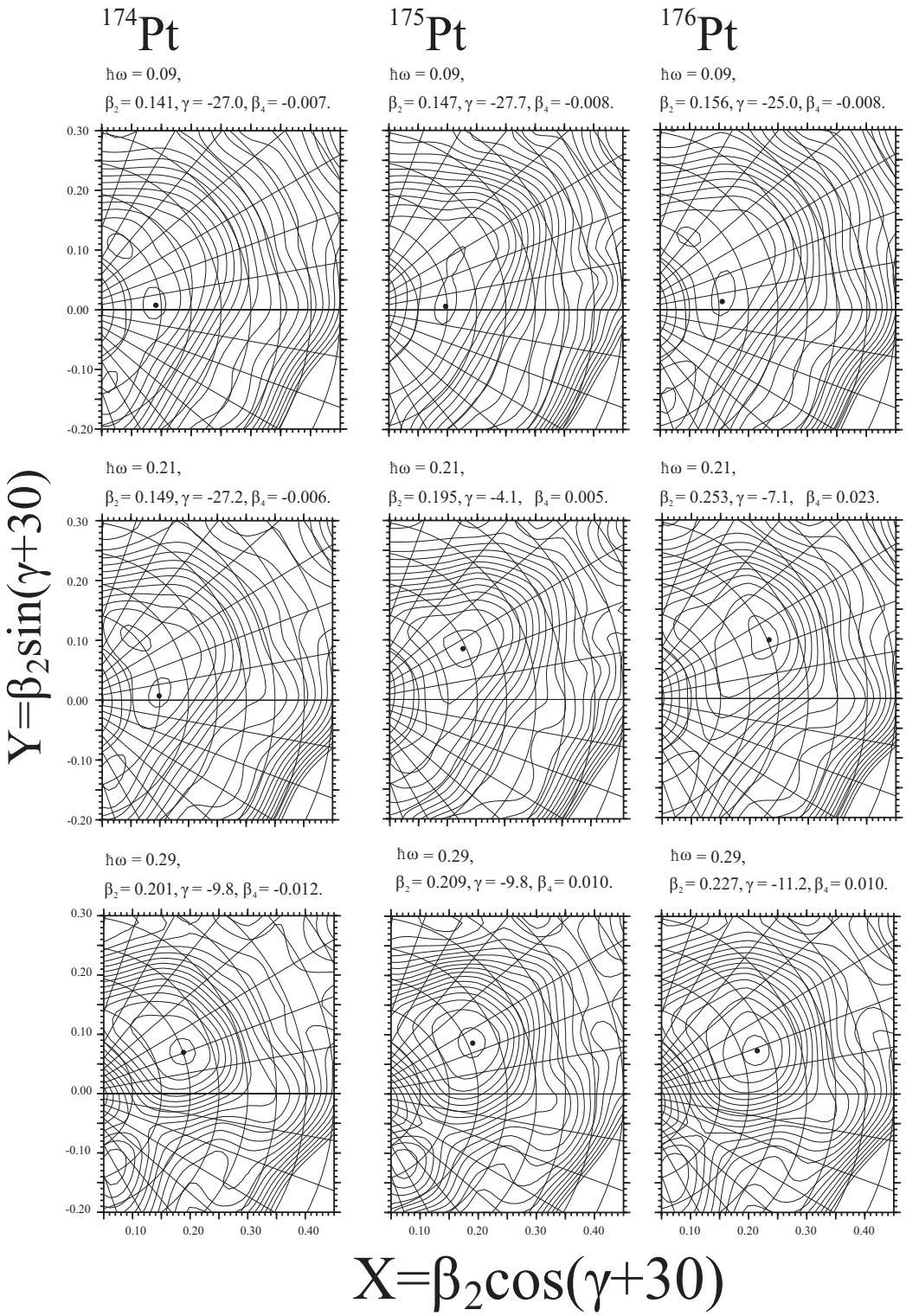

Figure 3.12: Total Routhian Surfaces for ^{174}Pt, ^{175}Pt and ^{176}Pt calculated at $\hbar\omega \sim 0$, $\hbar\omega \sim 0.2$ MeV and $\hbar\omega \sim 0.3$ MeV.

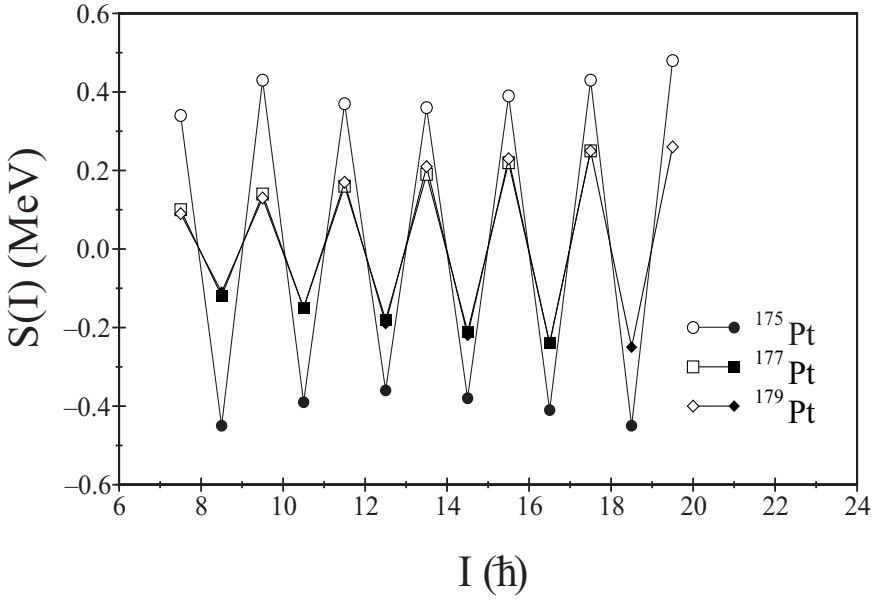

Figure 3.13: Staggering parameter S(I) as a function of spin I for the $i_{13/2}$ bands in the neutron-deficient odd-A Pt isotopes ^{175}Pt, ^{177}Pt and ^{179}Pt. The solid (open) symbols represent the $\alpha = +1/2(-1/2)$ signatures. The data for ^{175,177,179}Pt are taken from Refs. [Cede90, Drac90, Meis93].

reduction in the signature splitting with increasing spin, as is observed in the neutron-deficient odd-Z nuclide ^{163}Ta [Sand09]. This transition is not observed in these Pt nuclei and the signature splitting increases as the $N = 82$ shell-closure is approached. This observation can be interpreted as triaxial deformation becoming dominant as the number of neutrons decreases below the mid-shell. This a consequence of the underlying nuclear structure discussed above.

3.4.4 Collectivity of the 6^+ state in ^{174}Pt

The short lifetime measured for the 6^+ state corresponds to a high quadrupole moment indicating a collective structure. Figure 3.14 compares the transitional quadrupole moments (extracted from RDDS lifetime measurements) as a function of neutron number for excited states in several neutron-deficient Pt nuclei. The $|Q_t|$

values and their corresponding reduced transition probabilities, B(E2), indicate that the 6^+ state in ^{174}Pt is similar to collective prolate structures observed in nearby nuclei [Kond00]. This is consistent with the interpretation of a prolate band based on the scattering of a proton pair across the $Z = 82$ shell gap into the $(h_{9/2}/f_{7/2})$ orbitals [Drac91]. Unfortunately the lifetimes of the corresponding 2^+ and 4^+ states in ^{174}Pt could not be measured to show the shape change occurring due to band crossing of different proton structures. This is due to the 497/501 keV doublet in the yrast structure.

3.4.5 Shape coexistence in ^{175}Pt

The short lifetime measured for the $21/2^+$ state corresponds to a high quadrupole moment indicating a collective structure. The quadrupole moment extracted is comparable to the corresponding value for the 4^+ state in the even ^{176,178}Pt. Level energy systematics of the odd and even mass Pt nuclei show a strong coupling of the odd mass isotopes in relation to their even mass neighbours: the level energies are almost degenerate below $N = 98$ reflecting the decoupling of the odd neutron from the weakly decoupled core as suggested by Cederwall et al. [Cede90]. The TRS calculations predict the $17/2^+$ state in ^{175}Pt to be part of the γ-soft structure of the yrast band. The longer lifetime measured for the $17/2^+$ state in ^{175}Pt results in a lower $|Q_t|$ value relative to the higher spin prolate states. Though the reduction in $|Q_t|$ does suggest a change in shape of the nucleus at low spin the extracted $|Q_t|$ value assumes an axially symmetric deformed rotating nucleus. The degree of γ-softness cannot be accounted for in the calculations and so a conclusion on the degree of triaxiality of this nucleus at low spin cannot be made on the experimental lifetime analysis alone. Cederwall *et al.* also measured a decrease in lifetime with increasing spin in ^{176}Pt which was interpreted as the result of a shape change [Cede90].

The β_2 extracted from our experimentally determined lifetime measurements are compared in figure 3.15 with the β_2 deformation parameters extracted from the TRS calculations. The results from our experiment are consistent with the TRS extracted

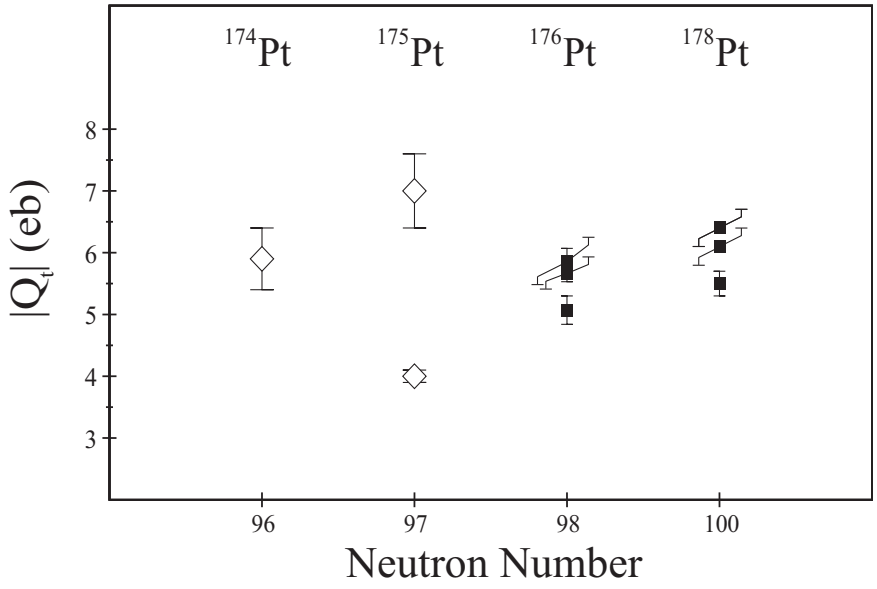

Figure 3.14: Experimental $|Q_t|$ values for the even-A $^{174-178}$Pt and the odd-A ^{175}Pt nuclei. The data for ^{176,178}Pt are taken from Refs. [Cede90, Kond00].

values and reinforce the conclusion of the crossing between a γ-soft structure and a deformed prolate structure for the yrast bands of ^{174,175}Pt at low spin. Though for the 6^+ state in ^{174}Pt and the $21/2^+$ in ^{175}Pt the extracted deformation parameter is greater than that inferred from the TRS calculations.

3.4.6 Triaxiality

The TRS calculations clearly indicate a degree of triaxiality at low spin in ^{174,175}Pt. Although a decrease in the measured lifetime is observed with increasing spin for ^{175}Pt, indicating a shape change, the extraction of the quadrupole moment $|Q_t|$ and deformation parameter β_2 are model dependent and assume the nucleus is axially symmetric. This assumption does not account for triaxility and may not be entirely in this instance. Using the deformation parameters β and γ extracted from the TRS calculations a quadrupole moment can be deduced using the following relation [Virt95]:

$$Q_t = \frac{6ZeA^{2/3}}{(15\pi)^{1/2}} r_0^2 \beta_2 \left(1 + \frac{2}{7}\left(\frac{5}{\pi}\right)^{1/2} \beta_2\right) cos\,(30^\circ + \gamma) \tag{3.2}$$

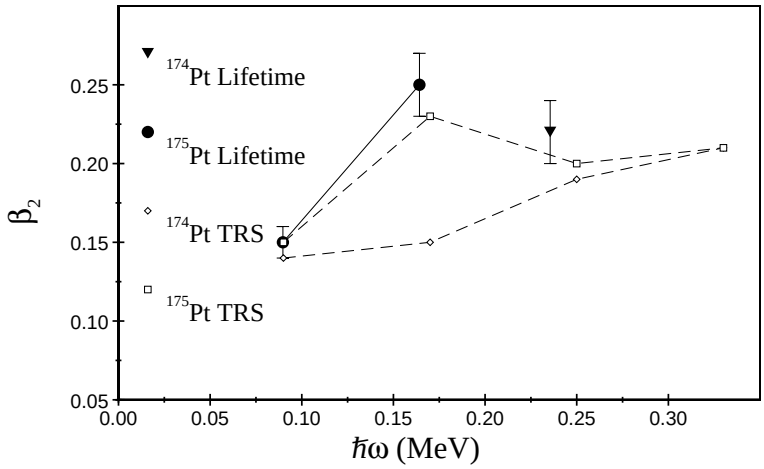

Figure 3.15: The extracted β_2 from our lifetime measurements are compared with those extracted from TRS calculations.

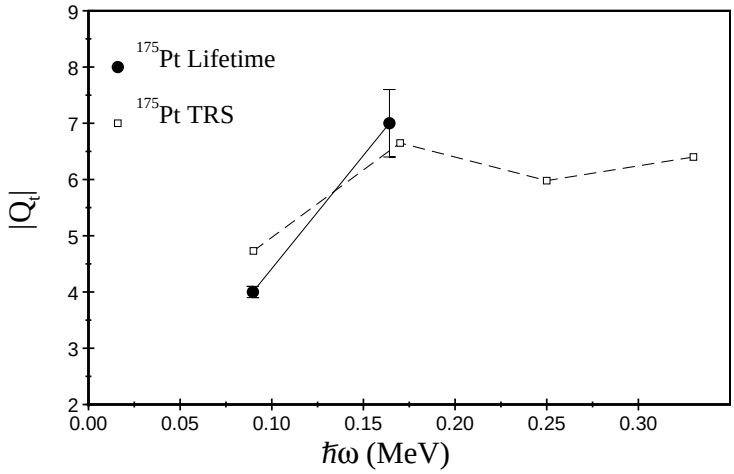

Figure 3.16: The extracted $|Q_t|$ values extracted from our lifetime measurements are compared with those incorporating γ extracted from TRS calculations.

where a value of 1.20 fm is used for the radius parameter r_0 and has to be converted into barns to give the units eb for the quadrupole moment. This can be compared to the experimental results in figure 3.16.

The extracted $|Q_t|$ value using the TRS calculated deformation parameters suggests the $17/2^+$ state has a greater collectivity, than implied by the $|Q_t|$ value extracted using the lifetime measurements, assuming an axially symmetric nucleus. This is to be expected as a triaxially deformed nucleus still exhibits collective behaviour. This cannot be accounted for when the $|Q_t|$ value is extracted from the lifetime measurement. However the increase in the lifetime measured with decreasing spin does indicate a shape change, as predicted.

Chapter 4

Deformation and collectivity of the coexisting shape triplet in ^{175}Au

The lifetimes of the low-lying excited states in the neutron-deficient nucleus ^{175}Au have been extracted from recoil-decay tagged γ-ray spectra using the recoil distance Doppler-shift method. Excited states were populated using the ^{92}Mo(^{86}Sr,p2n)^{175}Au* fusion evaporation reaction in an experiment performed at the University of Jyväskylä Accelerator Laboratory. By measuring the lifetime of the excited states, the absolute transition probabilities have been determined and provide a direct measure of the quadrupole collectivity. In considering the transition quadrupole moment extracted from the lifetime measurements it has been possible to investigate the competition of coexisting spherical, weakly deformed oblate and prolate deformed nuclear shapes occurring at low spin. In this chapter the results of experimentally determined lifetimes of excited states in ^{175}Au are discussed.

4.1 Triple shape coexistence in ^{175}Au

Shape coexistence is the phenomenon where different nuclear shapes based on distinct orbital configurations lie at similar excitation energies. This phenomenon can be explained in terms on multiple particle-hole (p-h) type excitations from orbitals

below a given shell gap to intruder states above it [Wood92, Heyd83]. The size of the shell gaps are strongly correlated with the arrangement of nucleons within specific orbitals close to the nuclear surface, which can polarize the nuclear core to adopt different deformations.

Neutron-deficient Pb nuclei ($Z = 82$) [Drac04] and those below the $Z = 82$ proton shell closure, such as Tl, Hg, Au and Pt nuclei [Lane94, Juli01, Kond01, Drac86] have exhibited many examples of the coexistence of different shapes when protons are scattered into deformation driving intruder orbitals above the shell gap. For example, the even-even Hg isotopes have oblate ground states that coexist with prolate shapes based on 4p-6h proton excitations [Naza93, Juli01]. The shape observed at low spin in these nuclei is correlated with the number of neutrons which results in the intruder states exhibiting a parabolic energy trend with a minimum about the neutron mid-shell ($N = 104$). For nuclei with a few neutrons above $N = 104$ nuclei, the low energy level structure is observed to be near spherical or oblate in shape. Approaching the $N = 104$ mid-shell the prolate minimum decreases in energy and dominates the low-energy structure. This occurs as the number of valence neutrons increases providing the maximum interactions to scatter the protons into the intruding orbitals. Below $N = 98$ the prolate minimum increases relative to the oblate ground state.

The coexistence of three shapes is comparatively rare with most of the cases being observed in even-Z nuclei [Andr00, Jenk02]. The sparseness of such cases is due to the lack of configurations available at low energy to stabilise three shapes. The phenomenon has been observed ^{186}Pb ($N = 104$), where a triplet of 0^+ states was interpreted in terms of coexisting spherical (0p-0h), oblate (2p-2h) and prolate (4p-4h) shapes [Andr00]. Also, odd-A nuclei [Jenk02], including the proton-unbound nucleus ^{175}Au [Kond01], exhibit structures that have been interpreted as a triplet of shapes.

The study of the Au nuclei ($Z = 79$) has provided invaluable information on shape coexistence and shape transition along the yrast line. For odd-A Au nuclei, above the $N = 104$ mid-shell, with $A < 187$, the low energy level structure is dominated by

oblate shapes [Rupn98]. For the lighter isotopes (around the $N = 104$) prolate shapes are preferred at lower energies. The stability of this prolate minimum is dependent on the proton single-particle states of the highest angular momentum, i.e. $\pi i_{13/2}$ and $\pi h_{9/2}$. The level structures in ^{181,183,185,187}Au consist mainly of prolate rotational bands and the intruder 1/2[541] $\pi(h_{9/2})$ and 1/2[660] $\pi(i_{13/2})$bands are most strongly populated [Muel99, Lara86, Joha89]. The $h_{9/2}$ rotational band lies lowest in energy for odd-A Au nuclei, but the prolate driving intruder orbital 1/2[660] $\pi(i_{13/2})$ comes lower in energy for the lighter Au nuclei [Muel99].

In ^{175}Au, different structures may be stabilised by the core polarising properties of the unpaired proton occupying the $h_{11/2}$ states below the shell gap or the $i_{13/2}$ intruder orbitals above the $Z = 82$ shell closure. The low-spin excited states for ^{175}Au established by Kondev *et al.*, were interpreted in terms of a spherical α-decaying $11/2^-$ isomer, an oblate $13/2^+$ state and a positive-parity sequence assigned as a collective prolate band [Kond01]. Figure 4.1 illustrates the available shape driving orbitals that the proton may occupy. The decreasing size of the shell gap towards prolate and oblate deformation is also highlighted.

Empirical values of deformation in the light Au nuclei have been inferred indirectly by estimating quadrupole moments from VMI fits to the $i_{13/2}$ bands and compared to predictions given by Total Routhian surface (TRS) calculations [Kond01]. However, obtaining direct experimental information on the collectivity and deformation of ^{175}Au is challenging from an experimental viewpoint. At present no quantitative information has been obtained on the shapes using techniques such as Coulomb excitation measurements due to exceedingly low yields of radioactive ion beams for this nucleus. However, it is possible to measure the lifetimes of weakly populated states using reactions of stable nuclei and measuring the Doppler shifts of γ-ray transitions selected by the recoil-decay tagging (RDT) technique [Paul95].

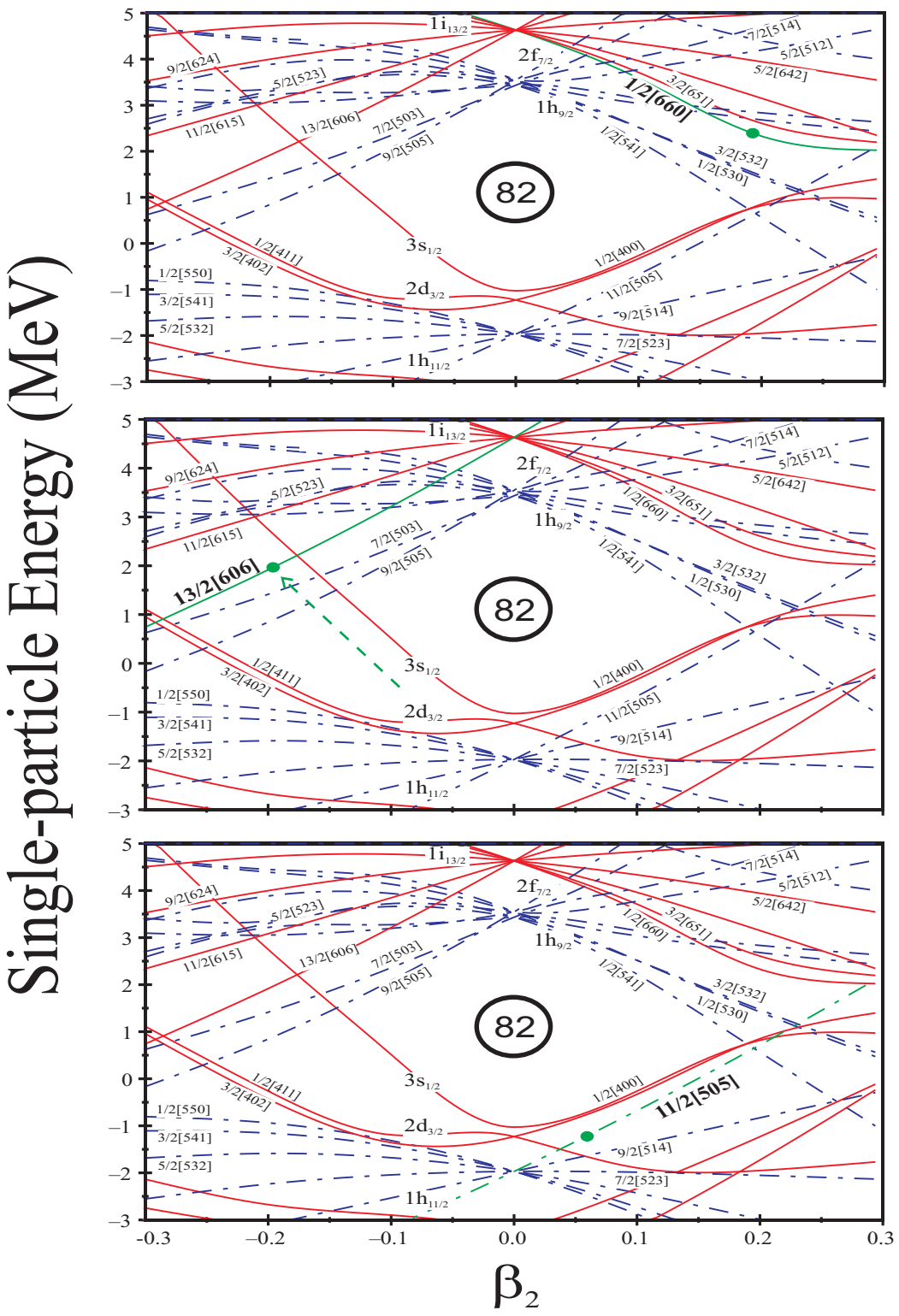

Figure 4.1: Schematic of the different shape driving proton orbitals surrounding the $Z = 82$ shell gap.

4.2 Results

4.2.1 Alpha decay properties of ^{175}Au

The α decay properties of ^{175}Au were measured using the DSSD of the GREAT spectrometer and are presented in figure 4.2. An improved measurement of $t_{1/2}$ = 138(2) ms for the half-life of the α-decay was obtained and is in agreement with the error weighted averages determined from published results: E_α = 6436(6) keV and $t_{1/2}$ = 156(5) ms [Rowe02, Kond01, Page96, Schn83, Andr10]. The half-life is measured by demanding a correlation of a 6.4 MeV α decay occurring within the same pixel of the DSSD, as the implanted recoil. In addition, correlations with the 294 keV γ-ray peak were used to suppress the background from random correlations [Bian08]. Correlations with the daughter α decay of ^{171}Ir cannot be used as it results in a shorter half-life than expected as the long half-life of ^{171}Ir of 1.40 s [Page96] biases the measurement. This is the result of an incorrect correlation with the next recoil implanting in the DSSD before the ^{171}Ir α decay. Figure 4.2 shows the decay curve of the measured half-life of ^{175}Au resulting from the additional 294 keV γ-ray correlation and the incorrect decay curve resulting from the additional ^{171}Ir daughter correlations.

4.2.2 Experimental details

The lifetimes of the low-lying excited states in ^{175}Au were measured using singles RDT γ-ray spectra obtained using the RDDS method. The yrast states of ^{175}Au were populated using the ^{92}Mo(^{86}Sr,p2n)^{175}Au* fusion evaporation reaction with a beam energy of 401 MeV. A Mg degrader foil of thickness 1 mg/cm^2 was used in the plunger device, providing a velocity difference of $\Delta v/c = 1.1$ %; $v/c = 4.4$ % before and 3.3 % after the degrader foil. Details of the energy differences of the fully Doppler-shifted and degraded components of the γ-ray transitions measured are listed in table 4.1.

The α decays of ^{175}Au were correlated with the recoils to construct the singles RDT γ-ray spectra. A partial level scheme of ^{175}Au is presented in figure 4.3 which shows the yrast band, the side band and the feeding transitions [Kond01]. Singles

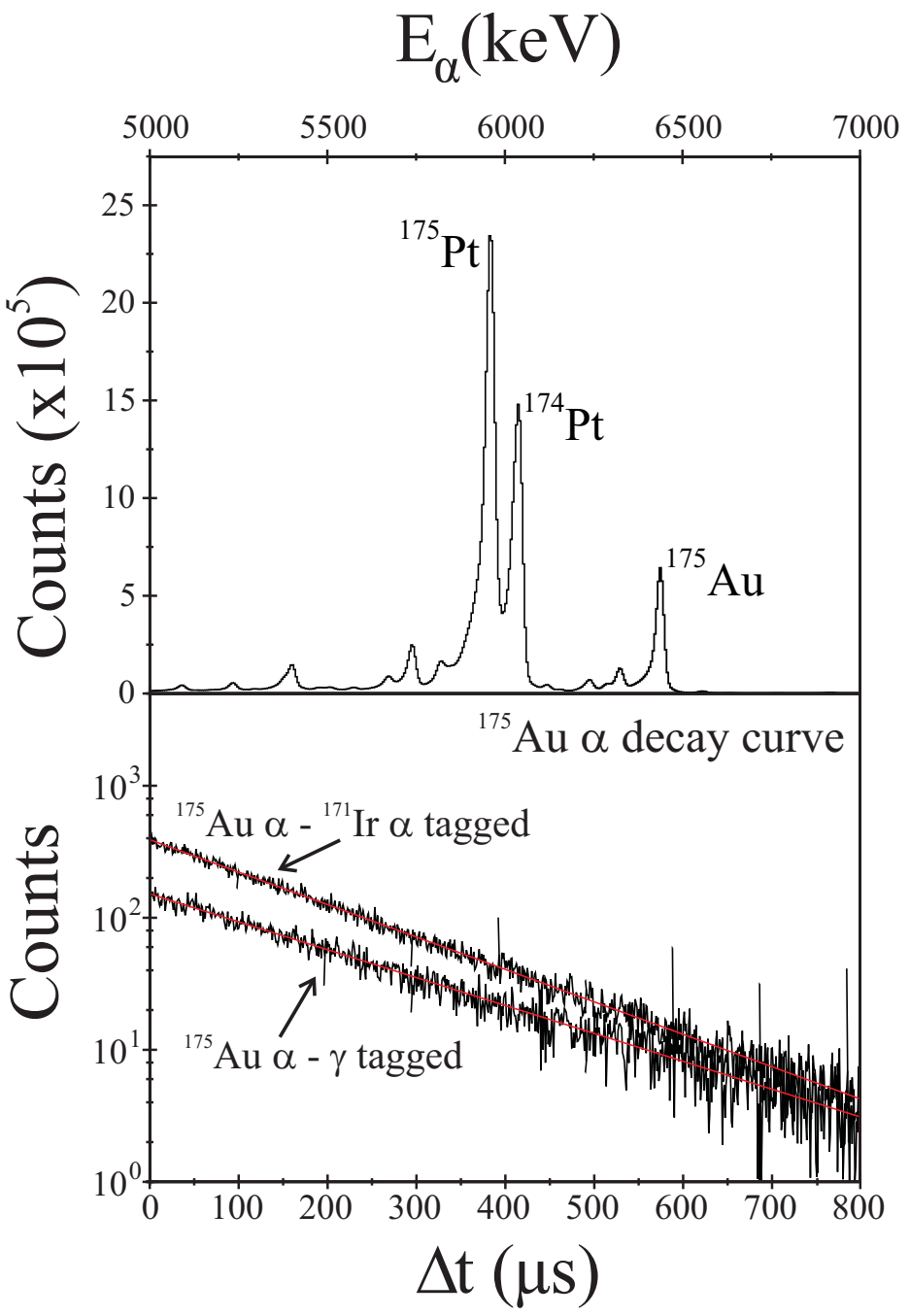

Figure 4.2: Alpha decay spectrum obtained from the DSSD of GREAT. The decay curve of the measured half-life obtained using the ^{175}Au alpha energy 294 keV γray correlation and is shown in the lower panel as well as the biased decay curve resulting from ^{175}Au and ^{171}Ir alpha energy correlations.

E_γ (keV)	J_γ	ΔE at 158° (keV)	ΔE at 134°	I_i^π	J_{feed}/J_{depop}
294	100	2.2	2.6	$17/2^+$	0.75(9)
323	75(9)	2.3	3.2	$21/2^+$	0.88(16)
380	66(9)	2.5	4.8	$25/2^+$	0.74(17)

Table 4.1: Energy separation ΔE of the fully Doppler-shifted and degraded components of the depopulating γ-ray transition of the states under investigation in ^{175}Au as well as the relative intensity J_γ and intensity balance J_{feed}/J_{depop}. The intensities are relative to the 294 keV $17/2^+ \rightarrow 13/2^+$ transition.

RDT γ-ray spectra were obtained for ten target-to-degrader distances ranging from 3 μm to 3000 μm, see table 4.2. Examples of the singles γ-ray spectra are shown in figure 4.4.

4.2.3 Lifetime measurements of the $25/2^+$ - $17/2^+$ states

For these lifetime measurements only Ring 1 (5 detectors at an angle of 158° with respect to the beam direction) and Ring 2 (10 detectors at an angle of 134°) of the JUROGAM Ge detectors were used. The fitted peaks were normalised to the summed intensities of the degraded (I_d) and fully shifted (I_s) components (see section 2.7). The quantity $Q_{ij}(d) = I^d_{ij}(d)/[I^s_{ij}(d)+I^d_{ij}(d)]$ for the states under investigation are shown in figures 4.5, 4.6 and 4.7. In the analysis of singles RDDS data the effect of the unobserved feeding transitions must be taken into account. The relative intensities of the feeding and depopulating transitions were measured from the experimental run with the highest statistics to calculate the intensity balance J_{feed}/J_{depop} of the level of interest. The result of this calculation for the states of interest is given in table 4.1. For the states for which the lifetimes have been measured in ^{175}Au it is reasonable to assume the time behaviour of the unobserved feeding to be similar to that for the observed direct feeder as discussed in section 2.9.

The mean lifetime τ value is a weighted average of the two values measured inde-

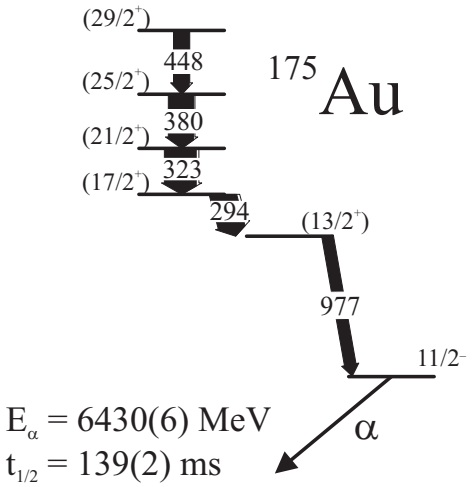

Figure 4.3: Partial level scheme of ^{175}Au showing the yrast band as well as the side band and feeding transitions according to Ref. [Kond01].

Distance d (μm)	Counts I_s + I_d
3.2(17)	216
25.0(1)	199
60.0(5)	212
100.1(5)	218
205.3(24)	192
300.4(20)	268
505.4(88)	228
1000(20)	250
1500(30)	231
3000(60)	236

Table 4.2: Peak areas measured for the $17/2^+ \rightarrow 13/2^+$ transition with 10 JUROGAM detectors at 134° at the 10 different target-to-degrader foil distances used.

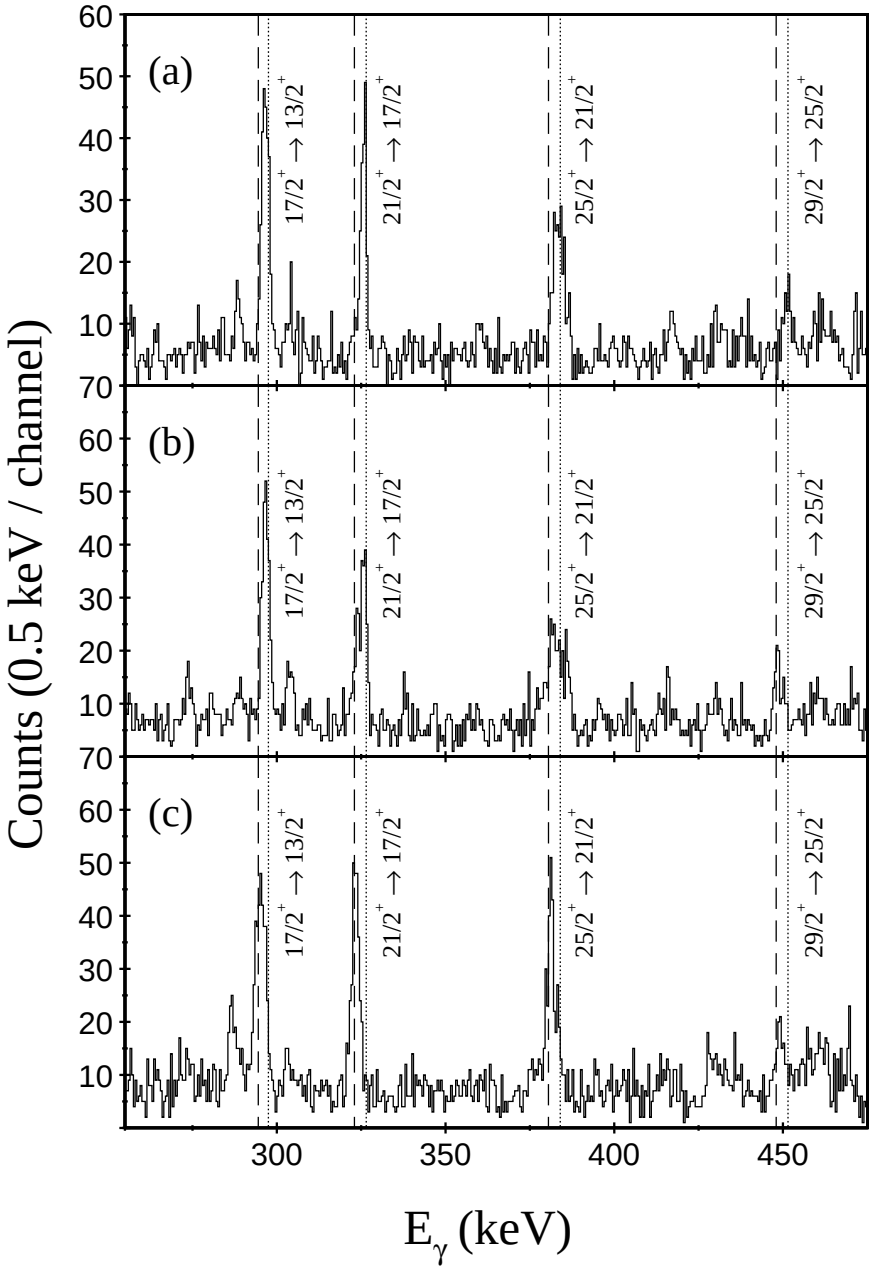

Figure 4.4: γ-ray spectra of ^{175}Au measured at three target-to-degrader distances: (a) 3 μm, (b) 100 μm and (c) 1000 μm with ten JUROGAM detectors at 134°. The dashed (dotted) lines indicate the positions of the fully Doppler-shifted (degraded) components of the transitions under study. The γ-rays were correlated with recoils implanted in the DSSD of the GREAT spectrometer that were followed by a distinct ^{175}Au α-decay within the same pixel. The recoil-α correlation time was limited to 470 ms.

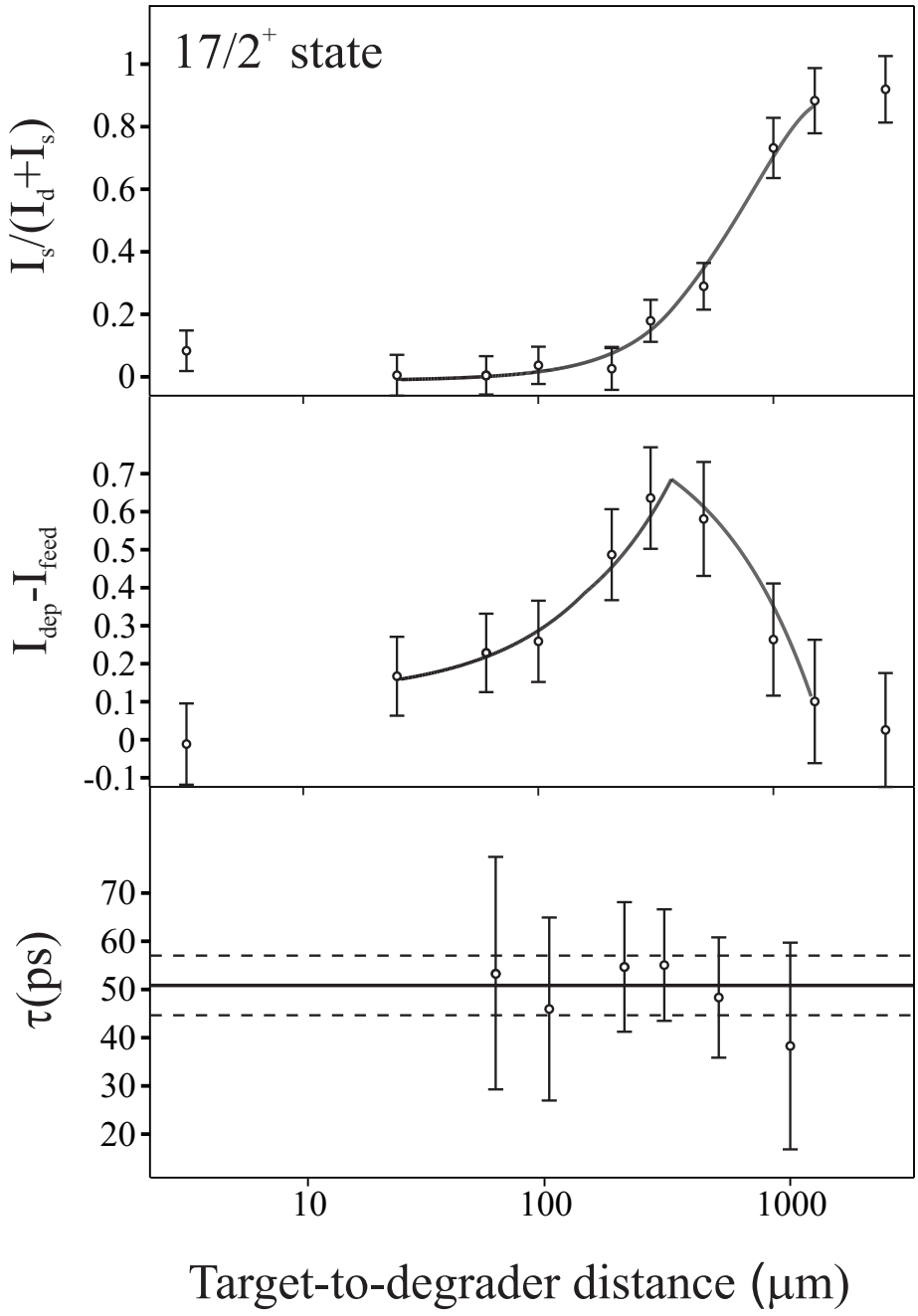

Figure 4.5: Decay curve of the $17/2^+$ state of ^{175}Au. The upper panel shows the decay curve $I^d_{ij}(d)/[I^s_{ij}(d)+I^d_{ij}(d)]$ of the $17/2^+$ state in ^{175}Au. The middle panel shows the intensity difference of the direct feeding and depopulating transition and the solid line is the derivative of the decay curve shown in the upper panel, these quantities are the numerator and denominator given in equation 2.8. The bottom panel shows the lifetime τ as a weighted mean of values $\tau(d)$

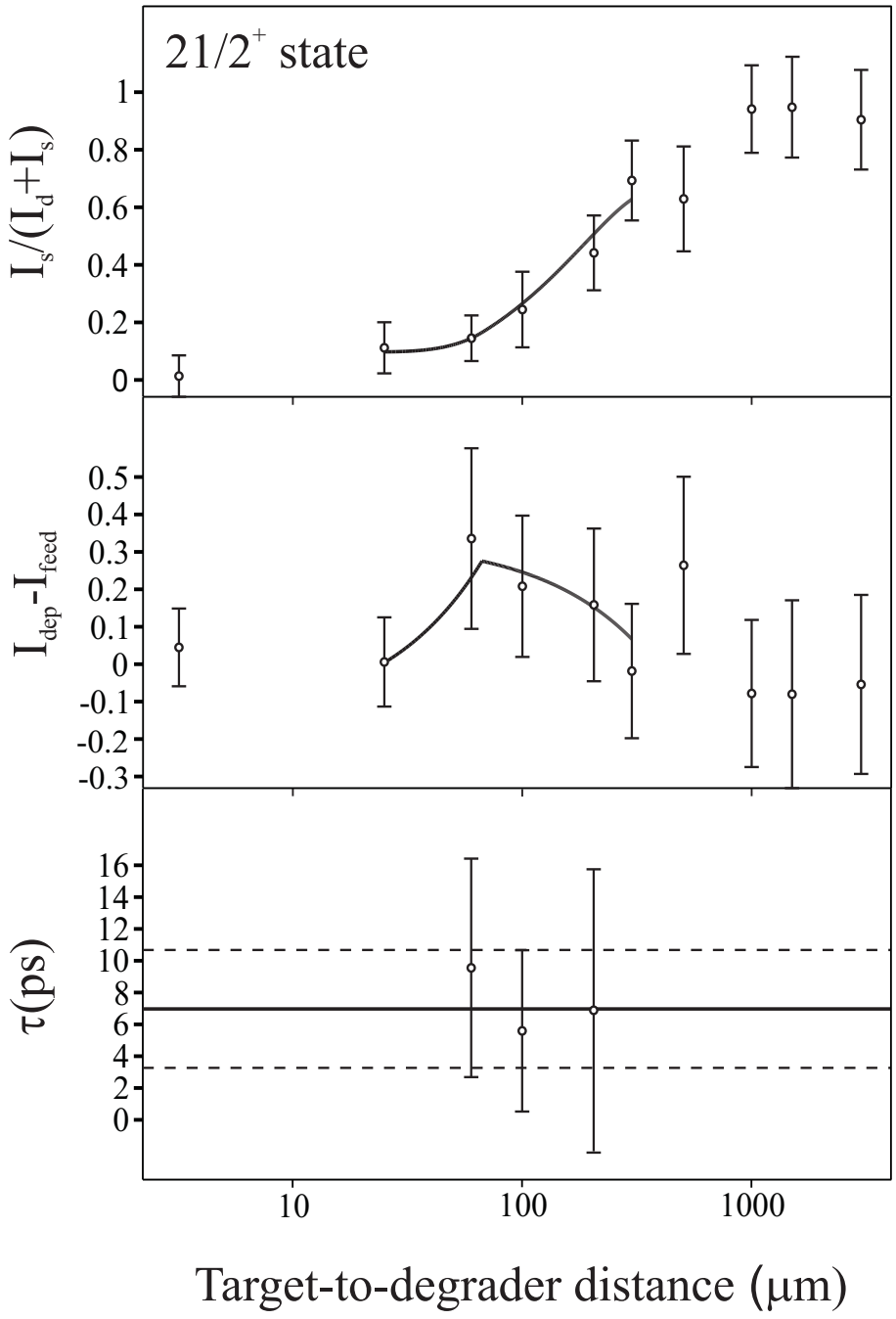

Figure 4.6: Decay curve of the $21/2^+$ state of ^{175}Au.

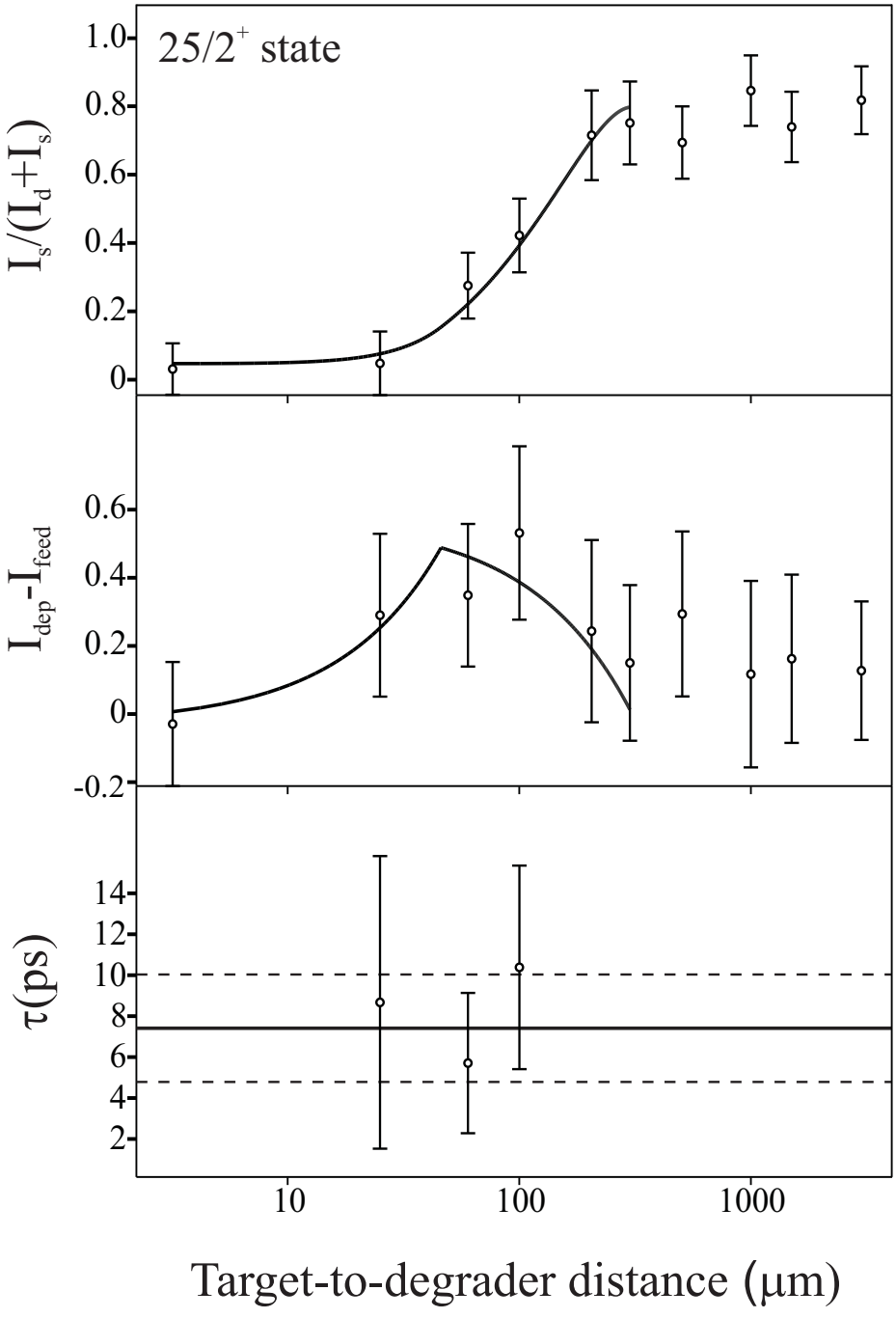

Figure 4.7: Decay curve of the $25/2^+$ state of ^{175}Au.

E_γ	I_i^π	τ	B(E2)	B(E2)	$\lvert Q_t \rvert$	$\lvert \beta_2 \rvert$
		ps	e^2b^2	W.u.	eb	
294	$17/2^+$	44(4)	0.76(7)	130(10)	4.8(2)	0.17(1)
323	$21/2^+$	11(2)	1.96(36)	340(60)	7.6(7)	0.27(2)
380	$25/2^+$	7(2)	1.40(40)	240(70)	6.4(9)	0.23(3)

Table 4.3: Electromagnetic properties of the low lying yrast states in ^{175}Au extracted from the lifetime measurement.

pendently from the data recorded with the detectors at 134° and 158°. The lifetimes of the $17/2^+$, $21/2^+$ and $25/2^+$ states are presented in table 4.3 along with the absolute values of the transition quadrupole moment $|Q_t|$ (equation 1.29) and deformation parameter β_2 (equation 1.32), extracted from the experimental reduced transition probability B(E2) (equation 1.28).

4.2.4 Lifetime measurement of the $13/2^+$ state

Only a limit for the lifetime of the $13/2^+$ state could be obtained. The 977 keV γ ray is observed to be in prompt coincidence with the γ ray transitions between high-spin states suggesting that the $13/2^+$ state de-excites within the focus of the JUROGAM spectrometer. However, no fully-shifted component was observed for the 977 keV depopulating transition at the maximum target-degrader distance (3000μm) used in the experiment. This implies a lifetime in the range of 0.3 - 11 ns for the $13/2^+$ state. The $13/2^+$ state is predominantly depopulated by an E1 transition to the $11/2^-$ α-decaying state. From the measured lifetime an experimental B(E1) reduced transition probability of $< 1.14\times10^{-6}$ W.u. has been determined using the transition probability equation given in table 1.3.

4.3 Discussion

In this study a change in collectivity for the low-lying states in ^{175}Au has been experimentally measured and in the context of a coexisting shape triplet interesting conclusions can be drawn. The large B(E2) reduced transition probability of the $25/2^+ \rightarrow 21/2^+$ and $21/2^+ \rightarrow 17/2^+$ transitions are indicative of high quadrupole collectivity for the $25/2^+$ and $21/2^+$ excited states. The decrease in transition probability of the $17/2^+ \rightarrow 13/2^+$ transition suggests a mixing between the collective prolate structure at high spin and a less collective oblate structure. The $E1$ transition probability of the $13/2^+ \rightarrow 11/2^-$ transition is reflective of a non-collective single-proton transition for the mixed configuration of the $13/2^+$ state to the weakly-deformed / near-spherical $11/2^-$ state.

4.3.1 Previous interpretation

Figure 4.3 shows the low-spin excited states for ^{175}Au established by Kondev *et al.* [Kond01]. The α-decaying isomeric state in ^{175}Au is based on the spherical $\pi h_{11/2}$ configuration coupled to the underlying Pt core. The main positive parity yrast sequence is a collective band based upon the prolate $\pi i_{13/2}$ configuration which feeds an oblate $\pi i_{13/2}$ state at 977 keV [Kond01]. The 294 keV transition feeding the oblate $\pi i_{13/2}$ does not follow the regular collective pattern established in the higher-spin states, indicating shape mixing.

The isotopic chain of odd-A Au nuclei has been studied to investigate the various shapes that occur as a function of neutron number. One particular point of interest is the properties of structures associated with proton excitations into low-Ω $i_{13/2}$, $h_{9/2}$ and $f_{7/2}$ intruder bands [Wood92, Muel04, Kond01]. For Au nuclei these intruder states exhibit a parabolic energy trend with a minimum below the neutron mid-shell ($N = 104$) [Muel04]. This trend has an impact on the dominant shape observed at low spin. Above the mid-shell, slightly oblate structures dominate at low spin [Heyd83]. Prolate structures dominate at low spin as the prolate deformed well

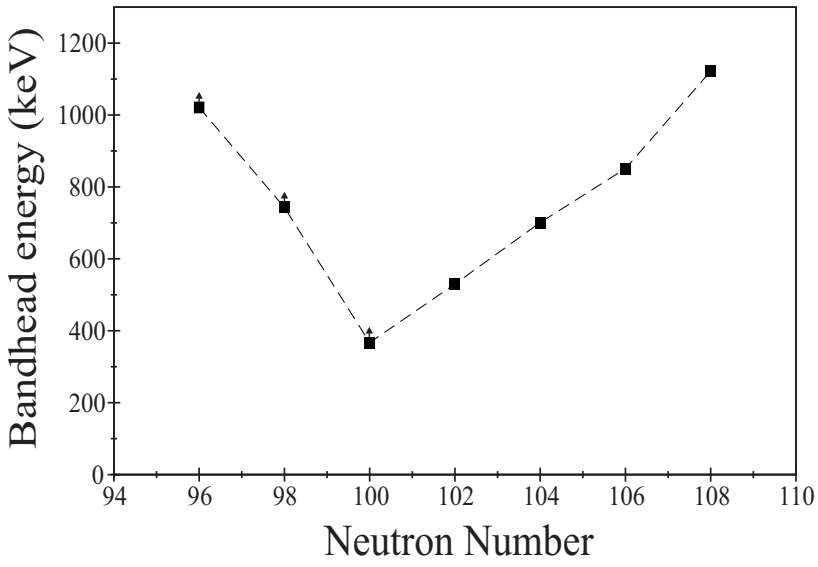

Figure 4.8: Experimental bandhead energies for the $\pi i_{13/2}$ bands in odd-A $^{175-187}$Au nuclei. Data for the heavier Au nuclei are taken from Refs. [Kond01, Muel04, Muel99, Lara86, Rupn98].

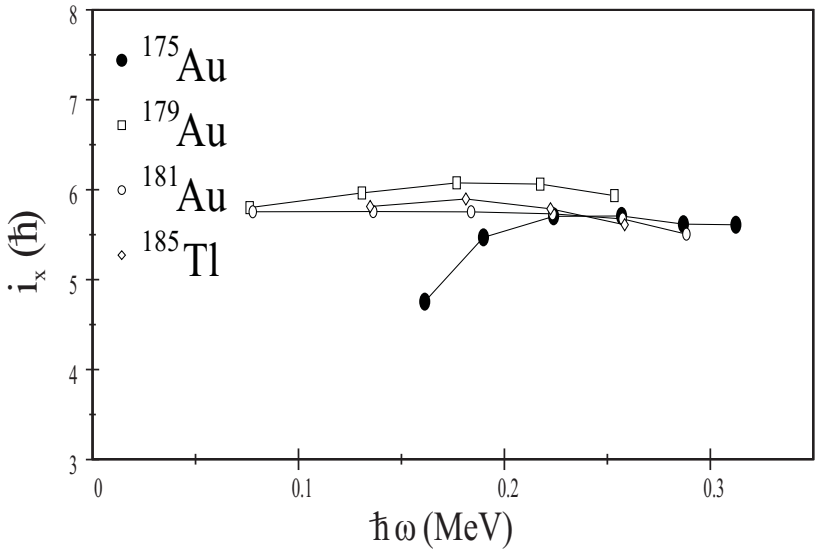

Figure 4.9: Aligned angular momentum for the $\pi i_{13/2}$ yrast bands in Au and Tl, extracted using the reference parameters, $\Im_0 = 27.5$ MeV$^{-1}\hbar^2$ and $\Im_1 = 190.0$ MeV$^{-3}\hbar^4$ for all nuclei. Data for the heavier Au nuclei and ^{185}Tl are taken from Refs. [Muel04, Muel99, Lane94].

drops in excitation energy near the proton mid-shell ($N = 104$) [Muel99]. Below the mid-shell, the minimum increases with decreasing neutron number to the extent that prolate states are observed but the oblate / near spherical states dominate at low excitation energy [Muel04, Kond01]. In these light Au nuclei the yrast prolate shape is assigned to the intruder $1/2^+[660](i_{13/2})$ proton configuration. Figure 4.8 illustrates this parabolic trend for the bandhead energies of the $\pi i_{13/2}$ rotational bands in odd-A Au nuclei. In the plot, the experimental bandhead energies in $^{175-179}$Au are the lower limits.

The experimental alignments for the $1/2^+[660](i_{13/2})$ yrast bands in the odd-A Au and Tl isotopes have been compared in figure 4.9. The observed values of $i \approx 6\hbar$ for these bands is consistent with expectations for a rotationally-aligned $i_{13/2}$ proton, supporting the $1/2^+[660]$ configuration assignment [Kond01].

4.3.2 Collectivity of the $25/2^+$ and $21/2^+$ states

The short lifetimes measured for the $25/2^+$ and $21/2^+$ states in ^{175}Au correspond to a high quadrupole moments indicating a collective structure. Figure 4.10 compares the transitional quadrupole moments (extracted from RDDS lifetime measurements) for excited states in several neutron-deficient nuclei near the neutron midshell. The $|Q_t|$ values and their corresponding reduced transition probabilities, B(E2), indicate that the high-spin states in ^{175}Au are similar to collective prolate structures observed in nearby nuclei. These data are consistent with the assignment of a prolate band based on an odd proton occupying a high-j $i_{13/2}$ intruder orbital proposed by Kondev *et al.* [Kond01].

Since the neutron-deficient nucleus ^{175}Au has an odd proton coupled to a ^{174}Pt core, insights into the particle-core coupling scenario may be inferred. The ^{174}Pt nucleus exhibits an yrast band, which deviates from the regular $I(I+1)$ rotational sequence due to the mixing of a weakly deformed ground state band and a deformed intruder band based on two-proton excitations across the $Z = 82$ shell gap [Drac91, Goon04]. These perturbations are clearly visible at low spin in plots of rotational

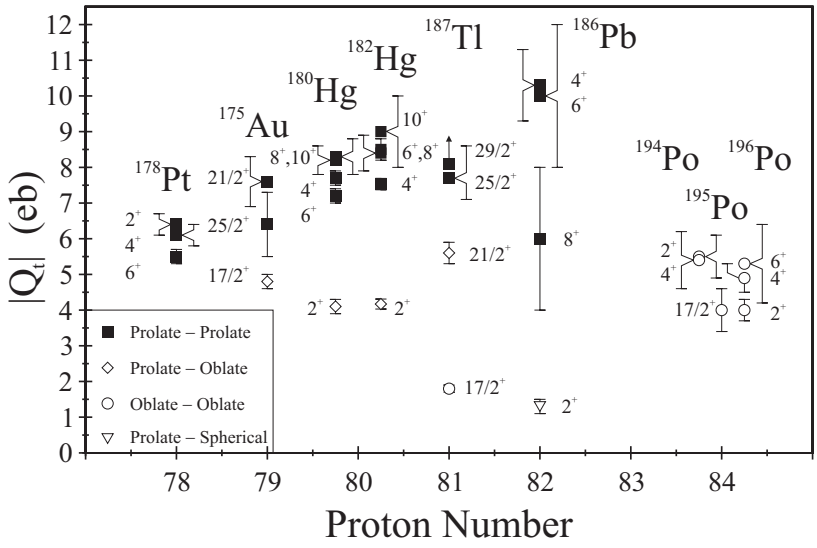

Figure 4.10: Experimental $|Q_t|$ values as a function of proton number for ^{175}Au and the known states in neutron deficient nuclei near the mid-shell. The spin values are those of the initial states. The data for the other nuclei are taken from Refs. [Drac86, Grah08, Sche10, Cham05, Grah06].

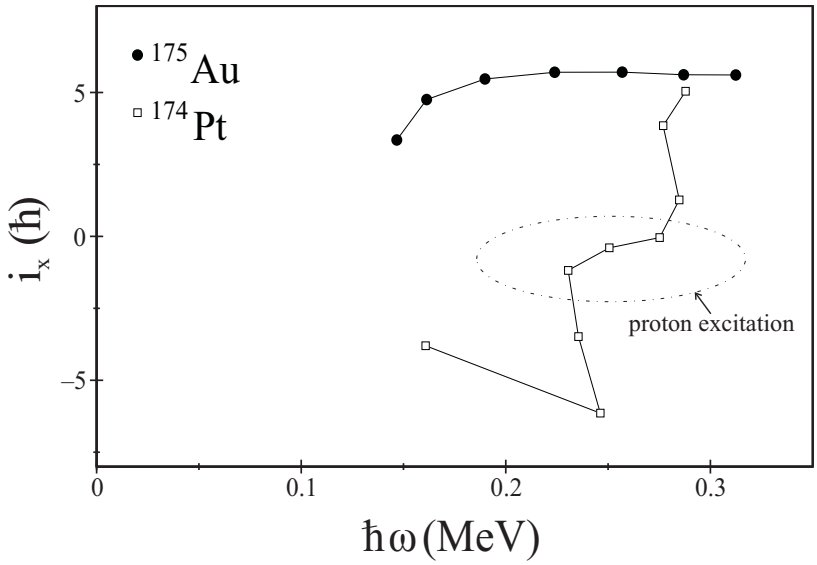

Figure 4.11: Aligned angular momentum i_x vs rotational frequency $\hbar\omega$ for the yrast bands of ^{175}Au and ^{174}Pt, extracted using the reference parameters, $\Im_0 = 27.5$ MeV$^{-1}\hbar^2$ and $\Im_1 = 190.0$ MeV$^{-3}\hbar^4$ for all nuclei. The data for ^{174}Pt is taken from [Drac91].

quantities such as aligned angular momentum and kinematic moments of inertia as a function of rotational frequency. A comparison of these rotational quantities can be seen in figure 4.11 in which the aligned angular momentum i_x of the ^{175}Au and ^{174}Pt yrast bands as a function of rotational frequency are plotted.

For ^{174}Pt the alignment plot is flat at the point at which the prolate deformation dominates. This flat alignment is also observed for the yrast band in ^{175}Au and may suggest that the prolate yrast band is the result of the odd-proton in the $i_{13/2}$ orbital coupled to the prolate deformed core of ^{174}Pt. The shape coexistence observed in ^{185,187}Tl was interpreted as the result of the odd-proton in the $i_{13/2}$ orbital coupled to the prolate deformed Hg core [Lane94].

4.3.3 Shape mixing at the $17/2^+$ state

The $17/2^+ \rightarrow 13/2^+$ 294 keV γ-ray transition does not follow the regular collective structure established for the prolate band. It has therefore been interpreted [Kond01] as not being a member of the rotational band but a transition out of the band to another structure. Kondev *et al.* applied a variable moment of inertia (VMI) fit to the levels between the $49/2^+$ and $17/2^+$ states. Extrapolating this fit to the $13/2^+$ state an energy of 199 keV for the $17/2^+ \rightarrow 13/2^+$ was predicted for in-band transition [Kond01].

The longer lifetime measured for the $17/2^+$ state in ^{175}Au, measured from the Doppler-shifted $17/2^+ \rightarrow 13/2^+$ γ-ray transition, results in a lower $|Q_t|$ value relative to the higher-spin states. Similar features are observed for the 2^+ states in ^{180,182}Hg [Grah08, Sche10] and the $17/2^+$ state in ^{187}Tl [Cham05]. In these nuclei, the relatively low quadrupole moments are interpreted as arising from a change from prolate shapes stabilised at high spin to oblate ground or low-spin states. The $|Q_t|$ measurement for the $17/2^+$ state in ^{175}Au is consistent with a scenario where the unpaired proton de-excites a prolate configuration to occupy a state based on a high-Ω $i_{13/2}$ intruder orbital. It can be noted that the $|Q_t|$ value for the $17/2^+$ state in ^{175}Au is higher than the analogous state in ^{187}Tl. This could suggest that the $17/2^+$ state

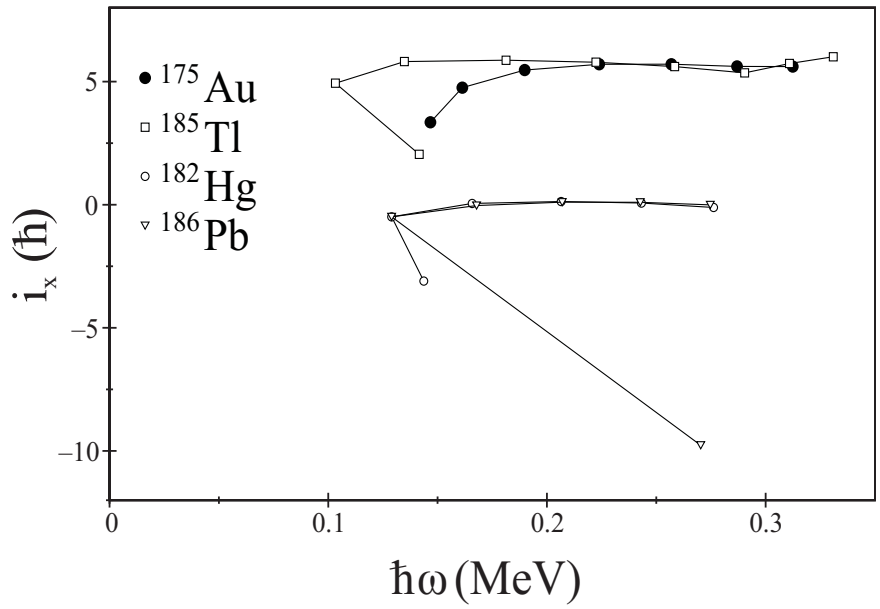

Figure 4.12: Aligned angular momentum I_x vs rotational frequency $\hbar\omega$ for the yrast bands of ^{175}Au, ^{185}Tl, ^{182}Hg and ^{186}Pb, extracted using the reference parameters, $\Im_0 = 27.5$ MeV$^{-1}\hbar^2$ and $\Im_1 = 190.0$ MeV$^{-3}\hbar^4$ for all nuclei. The data for the other nuclei are taken from Refs. [Lane94, Bind95, Paka05].

is a mixed configuration compared to the more purely oblate $17/2^+$ state in ^{187}Tl. Indeed, the lower γ-ray transition energy for the $17/2^+ \rightarrow 13/2^+$ transition should favour greater configuration mixing.

As discussed above the yrast band passes through a different structure at low spin and the $17/2^+ \rightarrow 13/2^+$ γ-ray transition is expected to link the prolate band to an oblate $13/2^+$ state. The $13/2^+$ state is assigned to the $13/2^+[606]$ intrinsic state which is associated with an oblate configuration. It can be seen in the Nilsson diagram, shown in figure 4.1, that the proton Fermi level for oblate shapes is near the high-Ω orbitals originating from the $h_{9/2}$ and $i_{13/2}$ shells intruding from above the $Z = 82$ shell gap. The alignment for the yrast band in ^{175}Au is plotted and compared to that of ^{185}Tl, ^{182}Hg and ^{186}Pb, see figure 4.12. The interpretation of the longer lifetime measured for the $17/2^+$ in ^{175}Au is supported by changes observed in this alignment plot. The flatness observed is indicative of the deformation of these nuclei

being comparable [Lane94]. This is supported by the measured $|Q_t|$ values shown in figure 4.10. The large gain in alignment at low frequency, observed in the Tl, Hg and Pb nuclei is due to the change of shape from oblate (Hg and Tl) or spherical (Pb) to a more deformed prolate shape. Though a change in alignment at low frequency is observed in ^{175}Au, the extent to which change occurs is not as prominent as the higher Z nuclei. This may suggest that the states in ^{175}Au are more mixed then they are in Hg, Tl and Pb nuclei and a shape change from a well deformed prolate shape towards a weakly-deformed oblate shape is occurring.

4.3.4 Single particle behaviour of the $13/2^+$ state

From the measured lifetime an experimental B(E1) reduced transition probability has been determined at the 10^{-5} W.u. level that is indicative of a non-collective single-proton transition from the $13/2^+$ state to the $11/2^-$ state. This result is comparable to the B(E1) reduced transition probabilities measured for the E1 transition from the $13/2^+$ oblate states in ^{185}Tl and ^{187}Tl of 6.2x10^{-6} W.u. and 7.7x10^{-6} W.u., respectively [Lane94]. The long lifetime for the $13/2^+ \rightarrow 11/2^-$ suggests a difference in the configurations of these two states which inhibits the transition. The $11/2^-$ state is assigned the $11/2^-$ $\pi[505]h_{11/2}$ configuration. The shape associated with this orbital changes gradually from triaxial at ^{185}Au [Lara86] to near-spherical at ^{173}Au [Kond01]. The change in shape is thought to be the result of a changing number of valence neutrons which are available to interact with protons and bring deformation-driving orbitals close to the proton Fermi surface. Away from the $N = 104$ mid-shell the number of valence neutrons decreases and the $h_{9/2}$ and $f_{7/2}$ bands observed in the heavier Au nuclei are no longer yrast resulting in states from the $s_{1/2}$, $d_{3/2}$ and $h_{11/2}$ orbitals to be observed at low spin. The Nilsson diagrams shown in figure 4.1 highlights that the $11/2^-[505]$ $\pi h_{11/2}$ orbital is near to a closed shell. This implies that at low spin the single proton $11/2^-$ state is likely to be weakly deformed or near-spherical in shape.

Chapter 5

Summary

The lifetimes of the low spin yrast states in ^{174,175}Pt and ^{175}Au have been measured using the RDDS method in a fusion evaporation reaction performed at the Accelerator Laboratory of the University of Jyväskylä. The Köln plunger device was installed at the target position of JUROGAM Ge detector array and coupled to the RITU gas-filled separator. The GREAT spectrometer at the focal plane of RITU was used to identify the recoiling nuclei with the application of the recoil decay tagging technique. The RDT technique provides background free γ-spectra allowing lifetime measurements using the RDDS technique to be extended to neutron-deficient nuclei with relatively low cross sections.

The lifetimes of the low lying yrast states in ^{175}Au have been measured providing quantitative information on the collectivity of the nucleus as it changes shape. By implementing the recoil decay tagging method background suppressed γ-ray spectra were produced enabling the RDDS technique to be employed to this highly neutron-deficient nuclei. The experimentally determined $|Q_t|$ values for the $21/2^+$ and $25/2^+$ states indicate a collective prolate structure, for the $17/2^+$ state the $|Q_t|$ value suggests a mixed configuration between the two prolate and oblate shapes as the unpaired proton de-excites from the collective prolate structure to the $13/2^+$ state. The experimental B(E1) reduced transition probability for the $13/2^+$ state indicates a non-collective single-particle transition as the unpaired proton de-excites to a weakly

deformed or near spherical shape. These measurements constitute the first measurements of a transition from collective prolate shape to a non-collective single particle state exhibiting triple shape coexistence in a heavy odd-proton nucleus stabilised by the excitation of an unpaired proton.

The lifetimes of the $17/2^+$ and $21/2^+$ in ^{175}Pt and the 6^+ state in ^{174}Pt have been measured by employing the RDDS technique and tagging methods, allowing the collectivity of the bands to be established. For ^{175}Pt the recoil tagged $\gamma\gamma$ method had to applied to resolve the issue of numerous doublets within the nucleus. The short lifetime measured for the 6^+ state in ^{174}Pt indicates a collective, prolate structure. This result is in agreement with the predicted frequency at which the shape change is predicted to occur according to TRS calculations. The extracted $|Q_t|$ value for the $21/2^+$ state is indicative of the state being part of the collective, prolate deformed band. The longer lifetime measured for the $17/2^+$ state in ^{175}Pt is in agreement with a predicted shape change from a prolate shape to a triaxial shape resulting from crossing of different proton structures.

Lifetime measurements using the RDDS method is the only feasible technique for such neutron-deficient nuclei as studied in this work. The technique provides invaluable information on the collectivity and deformation as the change in shape is directly measured experimentally. Though the degree of deformation can be ascertained, this technique cannot provide direct information on the type of deformation, that is whether the nucleus is prolate or oblate deformed. This may be determined from the sign of the quadrupole moment Q extracted from $B(E2)$ values measured via Coulomb excitation. For the exotic nuclei studied in this work the yields of radioactive beams required are not yet sufficient for these sufficient. However, the continuous development of radioactive beams means that future facilities will be able to provide the required beams to high enough yields to conduct such important experiments.

The microscopic origins of low-energy shape coexistence in these neutron-deficient nuclei can also be elucidated by studying excited states in odd-Z nuclei. The observation of intruder states in these nuclei allows for detailed information on the relative

positions of single-particle states to the Fermi surface to be extracted. Proton particles and proton holes couple to different cores, in Au the proton intruders couple to Pt cores and the proton holes couple to the Hg cores. The observation of structures based on hole excitations in Au nuclei provides a method of probing the even-even Hg core structure, which are known to exhibit the low-energy coexistence of 0^+ states. The $11/2^-$ states that lie at higher excitation energies are interpreted as predominantly $h_{11/2}$ holes coupled to $2p$-$4h$ deformed even-even Hg cores. Therefore, the corresponding $11/2^-$ states in odd-A Au isotopes are expected to have a predominantly $11/2^-[505]$ Nilsson structure. The experimental signature of such configurations is the presence of strongly coupled bands. As well as lifetime measurements using the recoil distance Doppler-shift method, excited states in ^{175}Au were also populated in fusion-evaporation reaction using a ^{92}Mo target and a 403 MeV $^{86}Sr^{16+}$ beam. This RDT experiment was carried out at the Accelerator laboratory of the University of Jyväskylä using the JUROGAM γ-ray spectrometer in conjunction with the RITU gas-filled separator and the GREAT spectrometer. Preliminary investigations into the expansion of the ^{175}Au energy level scheme has revealed a possible structure that could be the result of a proton hole couple to the ^{176}Hg core. Work is in progress to elucidate the structure of these observed excited states.

Bibliography

[Andr10] A.N. Andreyev *et al.*, J. Phys. G: Nucl. Part. Phys. **37** 035102 (2010).

[Andr00] A.N. Andreyev *et al.*, Nature **405** 430 (2000).

[Bark90] R.A. Bark, G.D. Dracoulis and A.E. Stuchbery, Nucl. Phys. A **514** 503 (1990).

[Bian08] L. Bianco *et al.*, Nucl. Inst. Meth. Phys. Res. A **597** 189 (2008).

[Bind95] K.S. Bindra *et al.*, Phys. Rev. C **51** 401 (1995).

[Beau92] C.W. Beausang *et al.*, Nucl. Inst. Meth. Phys. Res. A **313** 37 (1992).

[Beau96] C.W. Beausang and J. Simpson, J. Phys. G: Nucl. Part. Phys. **22** 527 (1996).

[Beng89] R. Bengtsson, J. Dudek, W. Nazarewicz and P. Olanders, Phys. Scr. **39** 196 (1989).

[Bohr40] N. Bohr., Phys Rev, **58** 654 (1940).

[Bohr75] A. Bohr and B.R. Mottelson, *Nuclear Structure Volume II: Nuclear Deformations*, W. A. Benjamin Inc., New York (1975).

[Cede90] B. Cederwall *et al.*, Z. Phys. A **337** 283 (1990).

[Cham05] S.K. Chamoli *et al.*, Phys. Rev. C **71** 054324 (2005).

[Darb06] I.G. Darby *Decay Spectroscopy of the Light Rhenium Isotopes*, PhD. thesis University of Liverpool (2006).

[Della81] S. Della Negra *et al.*, Z. Phys. A **300** 251 (1981).

[DeVo90] M.J.A De Voigt *et al.*, Nucl. Phys. A **507** 472 (1990).

[Dewa89] A. Dewald, S. Harissopulos and P. von Brentano., Z. Phys. A **334** 163 (1989).

[Dewa03] A. Dewald *et al.*, Phys. Rev. C **68** 034314 (2003).

[Drac86] G.D. Dracoulis *et al.*, J. Phys. G: Nucl. Phys **12** 97 (1986).

[Drac90] G.D. Dracoulis *et al.*, Nucl. Phys. A **510** 533 (1990).

[Drac91] G.D. Dracoulis *et al.*, Phys. Rev. C **44** R1246 (1991).

[Drac04] G.D. Dracoulis *et al.*, Phys. Rev. C **69** 054318 (2004).

[Duch99] G. Duchêne *et al.*, Nucl. Inst. Meth. Phys. Res. A **432** 90 (1999).

[Enge82] H.A. Enge *et al.*, Phys. Rev. C **25** 1830 (1982).

[Grah06] T. Grahn *et al.*, Phys. Rev. Lett **97** 062501 (2006).

[Grah08] T. Grahn *et al.*, Nucl. Phys. A **801** 83 (2008).

[Grah09] T. Grahn *et al.*, Phys. Rev. C **80** 14324 (2009).

[Grah10] T. Grahn *et al.*, Phys. Rev. C **81** 14310 (2010).

[Goon04] J.T.M. Goon *et al.*, Phys. Rev. C **70** 014309 (2004).

[Hari87] S. Harissopulos *et al.*, Nucl. Phys. A **467** 528 (1987).

[Harr65] S.M. Harris, Phys. Rev. **138** 509 (1965).

[Heyd83] K. Heyde, P. van Isacker, M. Waroquier, J.L. Wood and R.A. Meyer, Phys. Rep. **102** 293 (1983).

[Jenk02] D.G. Jenkins *et al.*, Phys. Rev. C **66** 011301R (2002).

[Joha89] J.K. Johansson *et al.*, Phys. Rev. C **40** 132 (1989).

[Joss06] D.T. Joss *et al.*, Phys. Rev. C **74** 014302 (2006).

[Juli01] R. Julin *et al.*, J. Phys. G: Nucl. Part. Phys. **27** R109 (2001).

[Kran88] K.S. Krane *Introductory Nuclear Physics*, John Wiley and Sons, New York (1988).

[Kond00] F.G. Kondev *et al.*, Phys. Rev. C **61** 044323 (2000).

[Kond01] F.G. Kondev *et al.*, Phys. Lett. B **512** 268 (2001).

[Kond02] F.G. Kondev *et al.*, Phys. Lett. B **528** 221 (2002).

[Lane94] G.J. Lane *et al.*, Phys. Lett. B **324** 14 (1994).

[Lara86] A.J. Larabee *et al.*, Phys. Lett. B **169** 21 (1986).

[Laza01] I.H. Lazarus *et al.*, IEEE Trans. Nucl. Sci. **48** 567 (2001).

[Lein95] M. Leino *et al.*, Nucl. Inst. Meth. Phys. Res. B, **99** 653 (1995).

[Lein97] M. Leino, Nucl. Inst. Meth. Phys. Res. B, **126** 320 (1997).

[Meis93] F. Meissner *et al.*, Phys. Rev. C **48** 2089 (1993).

[Muel04] W.F. Mueller *et al.*, Phys. Rev. C **69** 064315 (2004).

[Muel99] W.F. Mueller *et al.*, Phys. Rev. C **59** 2009 (1999).

[Naza93] W. Nazarewicz, Phys. Lett. B **305** 195 (1993).

[Nils69] S.G. Nilsson, Nucl Phys A, **130** 241 (1969).

[NLD87] W. Nazarewicz, G.A. Leander and J. Dudek, Nucl. Phys. A **467** 437 (1987).

[Nola94] P.J. Nolan, F.A. Beck and D.B. Fossan, Annu. Rev. Nucl. Part. Sci. **45** 561 (1994).

[NWJ89] W. Nazarewicz, R. Wyss and A. Johnson, Nucl. Phys. A **503** 285 (1988).

[Page96] R.D. Page *et al.*, Phys. Rev. C, **53** 660 (1996).

[Page03] R.D. Page *et al.*, Nucl. Inst. Meth. Phys. Res. B, **204** 634 (2003).

[Paka05] J. Pakarinen *et al.*, Phys. Rev. C **72** 011304R (2005).

[Paul95] E.S. Paul *et al.*, Phys. Rev. C **51** 78 (1995).

[Petk92] P. Petkov *et al.*, Nucl. Phys. A **543** 589 (1992).

[Pope97] D.G. Popescu *et al.*, Phys. Rev. C **55** 1175 (1997).

[Rahk08] P. Rahkila., Nucl. Inst. Meth. A, **595** 637 (2008).

[Rowe02] M.W. Rowe *et al.*, Phys. Rev. C, **65** 054310 (2002).

[Rupn98] D. Rupnik *et al.*, Phys. Rev. C **58** 771 (1998).

[Sand09] M. Sandzelius *et al.*, Phys. Rev. C **80** 054316 (2009).

[Sche10] M. Scheck *et al.*, Phys. Rev. C **81** 014310 (2010).

[Schn83] J.R.H. Schneider *et al.*, Z. Phys. A, **312** 21 (1983).

[Schw68] A.Z. Schwarzschild and E.K. Warburton., Annu. Rev. Nucl. Sci **18** 265 (1968).

[Venh10] M. Venhart *et al.*, Phys. Lett. B **695** 82 (2010).

[Virt95] A. Virtanen *et al.*, Nucl. Phys. A **591** 145 (1995).

[Wood92] J.L. Wood, K. Heyde, W. Nazarewicz, M. Huyse, and P. van Duppen, Phys. Rep. **215** 101 (1992).

[Wyss88] R. Wyss *et al.*, Phys. Lett. B **215** 211 (1988).